A Multi-Technique Comparative Evaluation of Ag Dispersion on Polycrystalline TiO_2

by

Zenda Deena Ann Davis

A thesis submitted to the Graduate Faculty of
Auburn University
in partial fulfillment of the
requirements for the Degree of
Master of Science

Auburn, Alabama
December 8, 2012

Keywords: silver, titanium oxide, desulfurization, x-ray photoelectron spectroscopy, adsorbents, crystallite size, dispersion

Approved by

Bruce J. Tatarchuk, Chair, Professor of Chemical Engineering
W. Robert Ashurst, Associate Professor of Chemical Engineering
Minseo Park, Associate Professor of Physics
Christopher B. Roberts, Professor of Chemical Engineering

Abstract

Energy independence, coupled with the increasing demands on energy supply, and rising environmental, health, and efficiency concerns have fueled the need for more appropriate refining processes in the petroleum industry. The North American pursuit of energy independence can be advanced through the refining of regionally available petroleum reserves – deposits of shale oil, tar sands, and bitumen. These unconventional deposits typically contain extra heavy oils that are extremely viscous and high in concentrations of sulfur. The processing of these sulfur rich feedstock presents many new challenges. One of these is the removal of heterocyclic sulfur compounds and their alkylated derivatives. Sulfur removal is necessary for the evolution of fuel cell technology and for cleaner fuel oil.

Catalytic and adsorption processes that target undesirable refractory sulfur compounds are being investigated for use in the desulfurization of hydrocarbon streams. A silver-titania adsorbent developed at Auburn University is one such compound that can be used in the desulfurization processes. The readily available raw materials, facile synthesis, and multi-cycle regenerability at ambient conditions make this adsorbent appealing. Ag/TiO_2 adsorbents are capable of removing various refractory species in the presence of 160 fold excess of competing aromatics in logistic fuels, such as JP5. Ag/TiO_2 adsorbents showed a consistent capacity of 8.5 mg S/g of competing aromatics for JP5 fuels ($\sim$1200 ppmw sulfur) for 10 cycles.

There is a continual effort to improve the sulfur sorption capacity of Ag/TiO_2 adsorbents. The first step in improving the quality of an adsorbent is to have a fundamental understanding of its properties. Literature has shown that there is a strong correlation between the efficacy of supported catalyst and particle dimension and dispersion. It is important to note that dispersion is important to gain the greatest access to the active atoms

of the adsorbent. Thus, the size of metal particles is crucial to the activity and selectivity of such systems. The purpose of this study was to perform fundamental studies to acquire a molecular level understanding of Ag/TiO_2 adsorbents used in the liquid phase desulfurization of logistics fuels. The ultimate goal of this study is the enhancement of performance capabilities and development of new sorbent materials.

In the literature, various techniques for the estimation of crystallite size are described. The intrinsic strengths and weaknesses of the four such techniques, Electron Microscopy (EM), X-ray Diffraction (XRD), Gaseous Chemisorption, and X-ray Photoelectron Spectroscopy (XPS) have been analyzed in their application to the Ag/TiO_2 adsorbent system. Oxygen chemisorption and XPS have proven to be useful in defining the catalytic system. Both techniques have demonstrated respective nanometer scale and sub-nanometer scale occurrence of Ag supported on titania. The results from these techniques complemented with information from Electron Paramagnetic Resonance (EPR) support the hypothesis that well dispersed silver oxide crystallite decorate defects on the titania support at low loading (<4 wt%). These crystallites are responsible for the preferential selectivity of Ag/TiO_2 for sulfur removal at low loadings.

The XPS particle size estimation was approximately a factor of approximately 5 less than the particle size found estimated by oxygen chemisorption for the same range. Particle size estimation using XRD was not achieved. Silver atoms are mono–dispersed between 0 – 4 wt % loading, after this loading there is a critical point beyond which particle growth occurs.

Acknowledgments

I would like to express my sincere gratitude to the many people who have supported me throughout this journey. My research adviser, Dr. Tatarchuk for his invaluable and enthusiastic, support and guidance. My family for their unconditional love and encouragement and my friends for keeping me grounded. I would also like to thank my colleagues – the past and present members of the Center for Microfibrous Materials Manufacturing (CM^3).

To everyone who has challenged, encouraged and empowered me. Thank you.

Table of Contents

List of Figures

List of Tables

List of Abbreviations

Acronyms

A_c	Cross-sectional Area
ADS	Adsorptive Desulfurization
A_m	Cross-sectional area of the active metal surface atom
ASA	Active Surface Area
BE	Binding Energy
BET	Brunaur-Emmett-Teller
CEN	European Standards Organization
EM	Electron Microscopy
EPA	Environmental Protection Agency
EPR	Electron Paramagnetic Resonance
ESCA	Electron Spectroscopy Chemical Analysis
FCC	face-centered cubic
FPM	First Principles Model
FTIR	Fourier Transform Infrared Spectroscopy
FWHM	Full Width Half Maximum
HDS	Hydrodesulfurization

HSA Hemispherical Analyzer

IMFP Inelastic Mean Free Path

IR Infrared Spectroscopy

KM Kerkhof-Moulijn

MM Molecular Weight

N_A Avogadro's number

N_m monolayer uptake

NN Nearest Neighbor

PEMFC Proton Exchange Membrane Fuel Cell or Polymer Electrolyte Membrane Fuel Cell

S/V Surface-to-Volume

S_A Surface Area

SF Sensitivity Factor

SMSI Strong Metal Support Interaction

SOFC Solid Oxide Fuel Cell

SPM Scanning Probe Microscope

TEM Transmission Electron Microscopy

TPD Temperature Programmed Desorption

TPRS Temperature Programmed Reaction Spectroscopy

UHV Ultra-High Vacuum

ULS Ultra Low Sulfur

XPS X-ray Photoelectron Spectroscopy

XRD X-ray Diffraction

X_i Mole fraction of i

English letter symbols

d particle dimension

f particle shape factor

I Intensity

L percentage metal loading

m metal

S adsorption stoichiometry

s support

Greek letter symbols

λ inelastic mean free path; wavelength

ϕ work function; angular frequency

ρ density

σ cross-section; specific surface area

Units

G Gauss

ppm parts per million

$ppmw$ parts per million weight

eV	electron volts eV

Definitions

Agglomeration:	The gathering of smaller crystallites into larger particles.
Experimental:	When used in tables mean experimental results.
Crystallite:	A small single crystal. Crystallites are constituents of particles.
Interatomic spacing:	The distance between the nuclei of atoms in a material
Mono-dispersed:	The distribution of a quantity for example, atoms in such a way that they are separated from each other i.e., not touching.
Monolayer:	A singly packed layer of atoms or crystallites.
Nucleate:	To aggregate as a result of the combination smaller crystallites into larger particles.
Particles:	A general term for small object of any size. Particles can be formed from one or more crystallites. In this work, particles correspond to the active phases rather than the support.
Sinter:	To form larger particles or masses by heating, by pressure or both.

Chapter 1

Introduction

Worldwide concerns about increasing anthropogenic air pollution have resulted in the establishment of stricter standards on transportation fuels. The aim of these standards is to reduce exhaust pollutants thus improving air quality and subsequently public health. Currently, there are no international standards mandating sulfur emission content. The European Union, the United States of America, Japan and China have been leading the world with the most severe environmental restrictions as pertaining to sulfur levels in fuels [2, 3]. The European Union, Japan, and China have forged ahead of the United States by restricting sulfur levels to 10 ppmw before or by 2008 [3]. While, in 2006, the United States limited ultra low sulfur diesel (ULSD) to 15 ppmw, a regulation established by the EPA under the Tier 2 Vehicle and Gasoline Sulfur Program Final Rule published in 2000 [4, 5]. Currently, there is no singular international body mandating strict worldwide sulfur emission conformity. The European Standards Organization (CEN) regulates Europe and the Environmental Protection Agency (EPA) regulates the United States. The environmental directives in other regions are regulated by local government and are driven by their economic needs. As a result, there is often little or no regulation in third world countries. Several protocols have been implemented to reduce sulfur emissions in a stage-wise process but none has had widespread global participation.

The emergence of fuel cells, which is a technology highly dependent on sulfur free fuels, has increased the need for ULS fuels. Fuel cells are desirable for several reasons: their ability to generate electric power directly from fuel, high efficiency, high energy, high power density, portability, simplicity, small size, silent operation, and extremely low emissions. Fuel cells require a high purity hydrogen input that is free of trace catalytic poisons. One

such identified poison is sulfur. Sulfur has deleterious effects on the performance of fuel cells and its removal is necessary for efficient fuel reforming. Polymer electrolyte membrane fuel cells (PEMFC) and solid oxide fuel cells (SOFC) require sulfur levels below 1 ppmw and 10 ppmw respectively for efficient operation [6–9]. Consequently, researchers need to develop more practical and efficient means to process ULS fuels to facilitate this technology and to meet rising environmental regulations. As a result, several processes are being investigated to achieve low sulfur standards; among them: bio-desulfurization, extractive desulfurization, oxidative desulfurization and the use of adsorbents.

Adsorptive desulfurization (ADS) is the most economical process currently available, with regards to industrial scale up and commercialization. The process of ADS relies on using a sorbent as a separation tool for the adsorption of sulfur compounds from refinery streams. In addition, the other alternative technologies have significant limitations in wide spread utilization. Bio-desulfurization has to overcome issues with catalysts inferior activity rates, thermal instability and slow reaction processes. Extractive desulfurization solvents extract large amounts of energy intensive hydrocarbons and typically cannot decrease refinery streams to ULS levels of 10 ppmw. Oxidative desulfurization is a comparably competitive process, but only after the chemical oxidation of the organic sulfur compounds, and it relies on ADS or extractive desulfurization to complete this process. Consequently, ADS has emerged a highly promising step in fuel refining [10, 11].

Future advancement in ADS technology requires the development of adsorbents with high sulfur capacity, high selectivity and multi-cycle regenerability. High sorption capacity (g of S per g of sorbent) is needed to remove as much sulfur as possible from a large volume of fuel in a single hydrocarbon stream pass. Selectivity is required to target specific compounds, particularly sulfur containing heterocyclic compounds such as thiophenes derivates and their alkylated derivatives that are difficult to chemically reform [12, 13]. It is also integral that the absorbents be able to resist chemical changes that causes deactivation and has multi-cycle retention properties to achieve competitive and economical sulfur removal. Ambient

temperature and pressure ADS of liquid fuels offers great advantages when compared to higher temperature and higher pressure HDS. The primary advantages being reduction in energy usage, capital and operating costs.

Many adsorbents have been studied for liquid phase desulfurization of logistic fuels in an effort to further develop effective adsorbents [6, 8–11, 14–19]. Adsorbents that strongly bind and isolate sulfur-containing compounds are needed to enable the transition into more environmentally benign sulfur products.

The novel Ag/Titania adsorbents developed at the Center for Microfibrous Materials Manufacturing (CM^3) at Auburn University has been found to be a more effective adsorbent for the liquid phase desulfurization of high sulfur logistic fuels [20]. Ag/TiO_2 adsorbents overcome two obstacles usually encountered in ADS namely, low capacity and selectivity. Ag/TiO_2 based adsorbents have been found to selectively remove sulfur containing aromatic compounds. The sulfur content in fuels such as JP5 and JP8 have been reduced to levels below 1 ppmw at ambient operating conditions.

A molecular level understanding of the surface chemical processes involved in the ADS process is needed to more fully explore the advantages. Information about the active sites, fundamental mechanisms, and chemical species at the adsorption interface is needed to truly understand the adsorbent system. Characterization of Ag/TiO_2 is a reverse problem formulation because the adsorbent was initially, found to possess desirable attributes instead of being tailored with the desirable attributes. Subsequently, investigations were carried out in a systematic manner to elucidate the surface chemistry interactions with the ultimate goal of improving performance and designing a superior adsorbent.

1.1 Objectives

The first step in improving the quality of an adsorbent is to have a fundamental appreciation of its properties. The characteristics of adsorbent are determined by the chemistry occurring at the topmost atomic layers. Fundamental studies were performed to extract

information at the surface interface. Research has shown that there is a strong correlation between the efficacy of supported adsorbent and crystallite dimension and dispersion. The purpose of this study was to acquire a molecular level understanding of Ag/TiO_2 adsorbents with the ultimate goal of improving performance capabilities and developing new sorbent materials. Thus, in an effort to achieve stepwise characterization of the adsorbents *a multi-technique comparative evaluation of Ag dispersion on polycrystalline TiO_2* was performed.

1.2 Overview

In this chapter, Chapter 1, the motivation of this work is presented along with objective and a brief outline of the subsequent chapters. Chapter 2 presents the literature review – an overview of the surface properties of the Ag/TiO_2 adsorbents previously determined is presented, four techniques of crystallite size determination are discussed along the fundamental physics and their sampling perspectives in their application the Ag/TiO_2 adsorbents system. Chapters 3, Experimental Methodology gives a brief overview of the techniques and the experimental conditions used. In Chapter 4, the experimental results are presented and discussed. Also, atheoretical method of crystallite size determination by XPS based on geometric probability developed by Kuipers et al. is applied.The final chapters, 5 and 6 detail the conclusions of this work and the potential for future work in clarifying outstanding issues and questions.

Chapter 2

Literature Review

The use of heterogeneous catalysts is widespread in the petroleum and chemical industries. Billions of dollars are spent each year on tons of heterogeneous catalysts. Thus, there is a continual effort to improve the quality of the catalysts for efficiency and economy. The first step in improving the quality of a catalyst is to have a fundamental understanding of its properties. In this chapter, the fundamental properties of the Ag was used along with simple theoretical concepts and experimental facts in the particle size and surface atom dispersion determination of Ag promoted on a TiO_2 support. Various methods can be used for the estimation of particle dimension and surface dispersion. Here, EM, XRD, gaseous chemisorption, and XPS have been explored; the fundamental physics along with their sampling perspective and biases were analyzed in the determination of Ag particles size in the Ag/TiO_2 adsorbents system.

2.1 Surface Chemistry of Silver-Titania Adsorbents

2.1.1 Adsorbent Preparation

Silver-titania adsorbents were made from 3.2 mm TiO_2 pellets [St. Gobain Norpro: Type ST61120]. The pellets were crushed, sieved and dried in a convection oven for at least 6 hours at 110 °C. Ag was dispersed on the support in the form of $AgNO_3$ solution [Alfa Aesar Co. 99.9 % purity] via incipient wetness impregnation to maintain 90 % of the pore volume of the TiO_2. The concentration of the $AgNO_3$ solution was varied according to the required load. The sample was subsequently dried at 110°C for 6 hours followed by calcination in air at 400°C for 2 hours.

Figure 2.1: 4 wt% Ag/TiO_2 adsorbent - 2.5× magnification

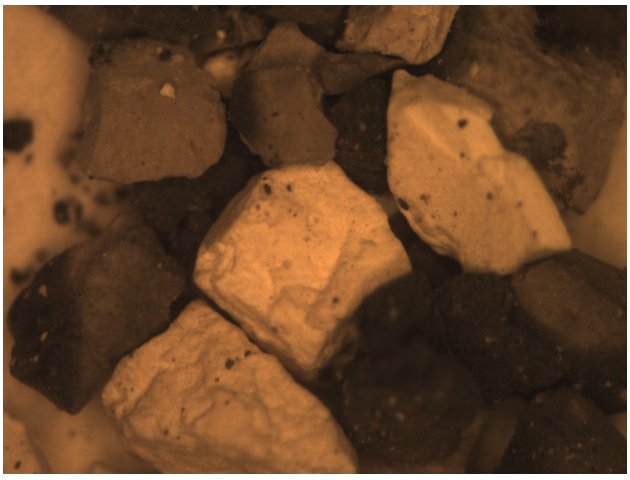

Figure 2.2: 4 wt% Ag/TiO_2 adsorbent - 15× magnification

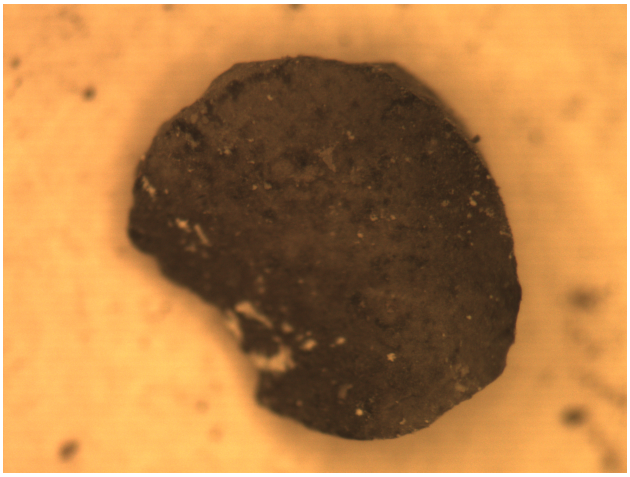

Figure 2.3: 4 wt% Ag/TiO_2 adsorbent - 25× magnification

2.1.2 Surface Properties

Table 2.1: Surface Properties of Ag/TiO_2 Sorbent.

Ag Loading (wt%)	BET surface area (m^2/g)	Pore Volume (ml/g)	Active Ag surface area (m^2/g)	Average crystal size (nm)	Dispersion (%)
0.00	153	0.46	–	–	–
4.00	114	0.27	6.7	3.4	34.4
8.00	89	0.23	10.7	4.1	28.7
12.00	79	0.21	12.1	5.3	22.4
20.00	58	0.13	14.3	6.9	17.0

Table 2.1 states the surface properties of Ag/TiO_2 sorbent used in this study. This data was previously published by Nair [1]. At 0 – 20 wt % loading Ag is present in the oxide phase. EPR and TPR analyses indicated that Ag is present in its oxide state as Ag^{1+} with minor concentrations present as Ag^{2+} [21]. TPR showed that the majority of Ag was present in the oxide phase at higher loading (greater than 4 wt%). Oxygen chemisorption was used to determine the average crystallite size of the silver particles on the surface.

2.2 Silver Crystal Structure

Ag has a face centered cubic (FCC) crystallographic structure with 4 atoms per unit cell – the Ag unit cell contributes 1/2 of an atom on each of its 6 faces to each unit, and 1/8 th of an atom at each of its 8 corners totaling 4 atoms. In the bulk, each atom has 12 nearest neighbors thus a coordination number of 12. The Ag (111) structure exposes a surface atomic arrangement of 3 fold symmetry which appears to be hexagonal. Fig 2.4 depicts the hexagonal packing of the surface atoms, which is the most efficient (closely packed) manner of atomic arrangement. The coordination number of the surface layer on the fcc (111) surface is 9; each atom has 6 nearest neighbors in the 1st layer and 3 in the layer below, totaling 9 atoms.

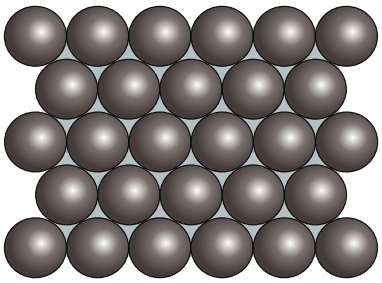

Figure 2.4: Birds eye view of an fcc structure of (111) plane

The density of atoms in Ag FCC (111) crystal plane is calculated from the lattice parameter, a. Since two corner atoms and and a central atom make up the length of the side diagonal of the FCC (see Figure 2.5), the lattice parameter is given by:

$$a^2 + a^2 = (4R)^2$$

$$a = \frac{4}{\sqrt{2}} = 2R\sqrt{2}$$

$$a = 4.08 \text{ Å}$$

The atomic density per cubic cm^3 of Ag(111) surface is:

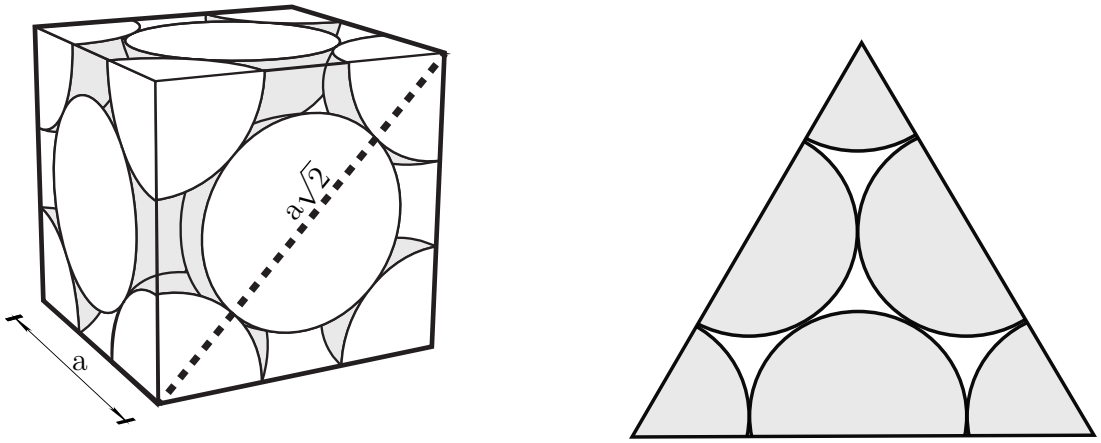

(a) 3d view of a unit cell **(b)** cross-sectional view

Figure 2.5: FCC structure of (111) plane

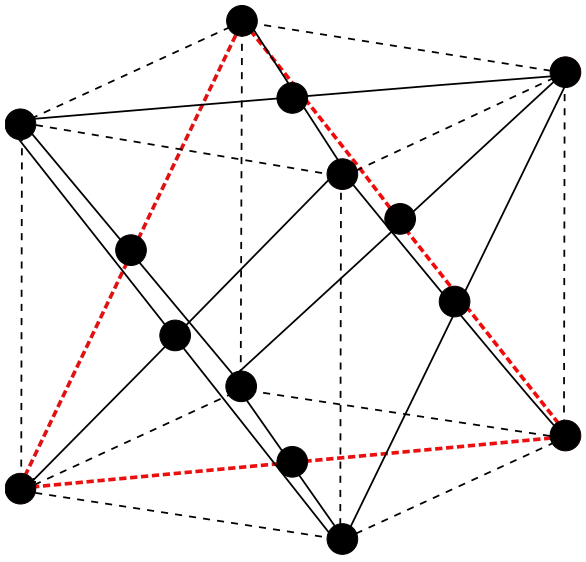

Figure 2.6: FCC (111) plane

$$\text{Ag atomic density} = \frac{\text{\# of atoms per unit cell}}{\text{Volume of unit cell}} = \frac{4}{a^3}$$
$$= \frac{4}{(4.08 \times 10^{-10}\ \text{m})^3}$$
$$= 5.88 \times 10^{28}\ \text{atoms/m}^3$$

The number of surface atoms is dependent on the surface structure. Considering the crystallographic surface heterogeneity of polycrystalline surfaces for dispersed metals, the usual approximation is to assume that such surfaces are formed from equal proportions of the main lox index planes [22]. Using this assumption, equal portions of the (100), (110) and (111) planes was used to estimate the polycrystalline planar concentration.

Density of atoms in Ag(111) crystal plane

$$\text{No. of atoms contained in Ag (111) plane} = \left(\frac{1}{6} \times 3\ \text{corners}\right) + \left(\frac{1}{2} \times 3\ \text{sides}\right)\ \text{atoms}$$
$$= 2\ \text{atoms}$$
$$\text{Area of Ag (111) plane} = \frac{a^2\sqrt{3}}{2}$$
$$\text{Surface density of atoms in Ag (111) crystal plane} = \frac{2}{\frac{a^2\sqrt{3}}{2}} = \frac{4}{a^2\sqrt{3}}$$
$$= \frac{4}{(4.08 \times 10^{-8})^2 \times \sqrt{3}}$$
$$= 1.38 \times 10^{19}\ \text{atoms/m}^2$$

Density of atoms in Ag(110) crystal plane

$$\text{No. of atoms contained in Ag (110) plane} = \left(\frac{1}{4} \times 4 \text{ corners}\right) + \left(\frac{1}{2} \times 2 \text{ diagonal center}\right) \text{atoms}$$

$$= 2 \text{ atoms}$$

$$\text{Area of Ag (110) plane} = a^2\sqrt{2}$$

$$\text{Surface density of atoms in Ag (110) crystal plane} = \frac{2}{a^2\sqrt{2}}$$

$$= \frac{2}{(4.08 \times 10^{-10})^2 \times \sqrt{2}}$$

$$= 0.85 \times 10^{19} \text{ atoms/m}^2$$

Density of atoms in Ag(100) crystal plane

$$\text{No. of atoms contained in Ag (100) plane} = \left(\frac{1}{4} \times 4 \text{ corners}\right) + (1 \text{ center}) \text{ atoms}$$

$$= 2 \text{ atoms}$$

$$\text{Area of Ag (100) plane} = a^2$$

$$\text{Surface density of atoms in Ag (100) crystal plane} = \frac{2}{a^2}$$

$$= \frac{2}{(4.08 \times 10^{-10})^2}$$

$$= 1.20 \times 10^{19} \text{ atoms/m}^2$$

Generally, in heterogeneous catalysis, only a monolayer (ML) of a chemisorbed species is adsorbed to the active sites. Assuming equal proportions of the Ag low index planes the number of Ag atoms in a ML is estimated to be 1.14×10^{15} atoms/cm^2.

2.3 Determination of Particle Size

2.3.1 Chemisorption

Gas phase chemisorption is the most extensively used technique for determining particle size and surface atom dispersion of supported metal catalysts in heterogeneous systems [24–33]. In this technique, a monolayer of chemisorbing atoms (surface atoms exposed) per number of total atoms is assumed to be directly proportional to the specific uptake. Oxygen has been shown to be the adsorbate that most accurately predicts the crystallite size dimensions of silver, the use of hydrogen and carbon dioxide as probe gases do not result in accurate determination of silver particle size [22, 26, 29]. The underlying theoretical assumptions of chemisorption are:

- Monolayer formation criteria - a monolayer is chemisorbed
- Stoichiometric ratio
- Adsorption selectivity
- Gas is adsorbed on the surface and not absorbed internally by the metal
- Unimodal particle size
- Crystallite formation
- Crystallite geometry
- Isolated atoms do not adsorb oxygen

Perspectives

Chemisorption is a simple, well-established surface weighted means of calculating the average particle diameter. Of all the techniques considered in this chapter, it is the most readily available techniques. Chemisorption is a surface area weighted average distribution

of the vital size. The accuracy of the techniques relies on background information, namely, the correct stoichiometric ratio, and the ability of a absorbate gas to selectively chemisorb on the active metal provided that there is constant gas uptake on the support when the metal is present or absent. For the Ag/TiO_2 adsorbent, there may be problems due to the variation in the stoichiometry ratio of Ag : O (the number of sites per chemisorbed oxygen atom) at the adsorption surface [29]. Although $Ag_{(S)} : O \simeq 1$ appears to be the best value as reported in the literature [28, 34, 35] other stiochiometries possibilities have been reported [28]. Differences in stoichiometries may be due to the hypothesis that the gas molecule to metal stoichiometry is dependent on metal particle size. Other discrepancies lie in the fact that the oxygen adlayer on silver has been reported to be complex [36, 37]. Complexities arise to carbonaceous contaminants which have an effect on the sorption behavior of oxygen due to possibility of subsurface oxidation of silver [28].

In chemisorption, there is size variation depending on the crystallite geometry assumed, for example, spherical and cubic geometries will produce slightly different average dimensions. See results in Table 4.6. Other problems that may arise include, multiple adsorption of oxygen molecule on metal surface atoms, internal absorption, incomplete adsorption of the oxygen molecules by the metal particles, and non-metallic silver particles. Of these problems, explanations for exaggerated crystallite size would be adsorption by titania support – subsurface adsorption and multiple adsorption of gas molecule on metal surface atoms – under estimation of the stoichiometric ratio [30]. Lower crystallite size would result from over estimation of the stoichiometric ratio and inability of absorbate gas to selectively chemisorb a monolayer.

2.3.2 X-ray Photoelectron Spectroscopy

XPS is based on the detection of photoelectrons from a sample irradiated by an X-ray source. The detected photoelectrons are recorded in a energy spectrum. This energy spectrum is analyzed to produce a wealth of chemical information about the sample under

investigation. XPS is sensitive for trace amounts of all elements with the exception of hydrogen. Quantitative information is received only from the top 10 nm of the surface thus, XPS is defined as a surface analysis technique. Like chemisorption, XPS is a well established as a technique for studying surface atom dispersion and particle size of metal on supported systems [38–47], however, in comparison it is less often used to acquired particle size dimension [48–53].

The basic assumptions underlying XPS are:

- The number of electrons recorded is proportional to the number of atoms in a given state
- Variation in the chemical environment does not appreciably affect the overall ejected photoelectrons
- Mono-dispersion of surface atoms

Perspectives

XPS is a non-destructive, surface analysis technique that gives a near- surface weighted measurement of the average particle dimension. Although there is general agreement that XPS offers a surface weighted characterization of particle dimension, Fung [49] postulated that XPS also adds a volume aspect such that it gives an account of the particle dimension based between the surface and volume average size. In XPS, the particle size is determined without extensive pretreatment with regards to other techniques. This is important as pretreatment may alter the state of the particle or crystallite in question.

XPS is broadly applicable – all elements can be observed in XPS with the exception of hydrogen. Also, unlike chemisorption, XPS is applicable to metal and metal oxides (reducible and irreducible phases). XPS offers good chemical resolution and depth resolution. The shortcomings of the past regarding poor spatial resolution and detection limit [54] have been improved upon in recent years [55–57].

2.3.3 X-ray Diffraction

X-ray diffraction XRD, is a non-destructive analytical technique which is used to derive information about the crystal structure, chemical composition, and physical properties of materials. In XRD, the scattered intensity of X-ray radiation is used to produce photon energy spectra as a function of the incident and scattered angle, polarization, and wavelength on a given sample. The spectra produced are characteristics of the composition of the sample. The scattered monochromatic X-rays are the result of constructive interference by the atoms in the crystal plane. Crystalline material produce diffraction maxima according to the Bragg equation:

$$n\lambda = 2dsin\theta \tag{2.1}$$

where n is an integer, λ is the wavelength of incident wave, d is the spacing between the planes in the atomic lattice, and θ is the angle between the incident ray and the scattering planes. The average crystallite size is determined by X-ray broadening [58, 59] by the Scherrer expression:

$$D = \frac{k\lambda}{\beta cos\theta} \tag{2.2}$$

where D is the mean diameter, β is the pure X-ray diffraction broadening and k is a constant ≈ 1. k and β are constants dependent on the crystallite shape.

Perspectives

XRD is a non-destructive, volume weighted means of determining crystallite size. The major weakness of this technique lies in the determination of small crystallites. If the irradiated volume is too small for a sharp diffraction maximum to build up, the resulting diffraction pattern is broadened [59]. From the literature, the lower detection limit is reported to be $\lesssim 5$ nm [27, 49, 61]. However, when a synchrotron radiation source is used, platinum particles as small as 1.5 nm have been estimated [62]. This is a result of a better signal to noise ratio produced using the high intensity radiation.

The agreement between X-ray line broadening (XRD) and gaseous chemisorption is good when particles are greater than > 50 Å and < 1000 Å [26] XRD did not provide conclusive measurements when applied in the crystallite size determination of Ag/TiO_2 adsorbents. The lack of signal suggested that the crystallite was below the detection limit of the XRD $\approx$ less than 5 nm. This is a result of X-ray broadening of the diffraction beam produced from very small crystals at angle close to the Bragg angle [59, 60]. Strong diffraction beam pattern form from bigger crystals than smaller crystal. Since, the instrumental peak width was much larger than the broadening due to crystallite size, the crystallite size could not be determined. A silver peak was detected at the 20 wt% loading however due to its small size and broad width a size dimension could not be reliably determined.

2.3.4 Electron Microscopy

Electron microscopy EM, is the near atomic scale microscopic examination of objects, through the use of highly energetic electrons (produced form a highly focused X-ray beam). EM can yield information on the topography, morphology, composition, and crystallography of a given sample. There are several forms of EM available. In this work, only transmission electron microscope (TEM) will be employed. In TEM, information is projected in two-dimensional image from the interaction of the electron beam with matter encountered. Detection is dependent on the existence of sufficient contrast between the particle and the support.

Perspectives

EM is a projected area, perimeter weighted average of size distribution. The main advantages of TEM are that it is a straightforward technique and the particles can be viewed from the images created. However, care must be taken during interpretation regarding the possible sources of contrast. Ideally, contrast should be as a result of the attenuation of electrons on the surface of the given sample but, there is also contrast due to diffraction

and interference which lead to misinterpretation [63, 64]. TEM is very prone to contrast issues. It is difficult to contrast supported catalyst material, thus it is not a good technique for particle size determination os supported catalysts. Other disadvantages are that it is destructive and difficult to prepare; extremely thin sections of specimens, typically about 100 nm are needed. Several samples must be examined with a large number of particles to produce a accurate quantitative representation of the sample.

The application of the TEM using the diffraction contrast method proved to be fruitless in the determination of particle size on the Ag/TiO_2. Information on particles size was not discernible from the bright and dark field images produced [65].

2.4 Comparison of the Various Methods of Particle Size Determination

Undoubtedly, the most valuable information is derived through a combination of several characterization techniques. However, when comparing techniques the underlying assumptions and perspectives must be considered when evaluating the information received. Since the information required is average particle size, the basis of the average weighting must be considered during analysis of the representation of particle size.

2.4.1 Impact of Sampling Perspective on Particle Size

Many techniques make an convenient assumption about the geometry of a particle when determining particle size. This is done to lessen the complexity, for example, an amorphous particle is described by many lengths (shortest and longest diameter and perimeter) in various different directions (x-axis, y-axis or a percentage of both). Taking all these length into consideration to determine the true particle size would be overly complex. Thus, using an assumption of a regular geometric shape will be valuable. This results in a trade off decreased complexity at the concession of a small reduction in accuracy, which research has shown has very little effect [66].

Each technique derives particle size based on a physical principle. A physical value such as, volume of a gas, scattered light and electron count is measured and used to determine average particle dimension. Each technique is based on a particular calculation namely, number, surface, and volume. For example, the XRD measures light scattered from various particles and averages the dimensions produced from the distribution of particles.

In a number distribution, each individual particle has equal weighting. In a volume distribution, weighting is placed on the number of particles of a particular volume. Likewise, in surface area distribution, weighting is placed on the number of particles that gives a particular surface area. In Figure 2.7, 42 particles of three different sizes are depicted. Figures 2.8, 2.9, and 2.10 shows the number, volume, and surface area distribution respectively. In Figure 2.8, each particle size accounts for one-third of the total. The 1 nm, 2 nm, and the

3 nm particles all carry equal weight because each group has a total of 14 particles. This makes it clear that size is not a determinant factor in number distribution. The same result is translated in a volume distribution in Figure 2.9 where the 1 nm, 2 nm, and the 3 nm particles account for 2.8 %, 22%, and 75% respectively of the total volume. Likewise, in figure 2.10, the surface area distribution the 1 nm, 2 nm, and the 3 nm particles account for approximately 8 %, 31%, and 61% respectively of the total surface area.

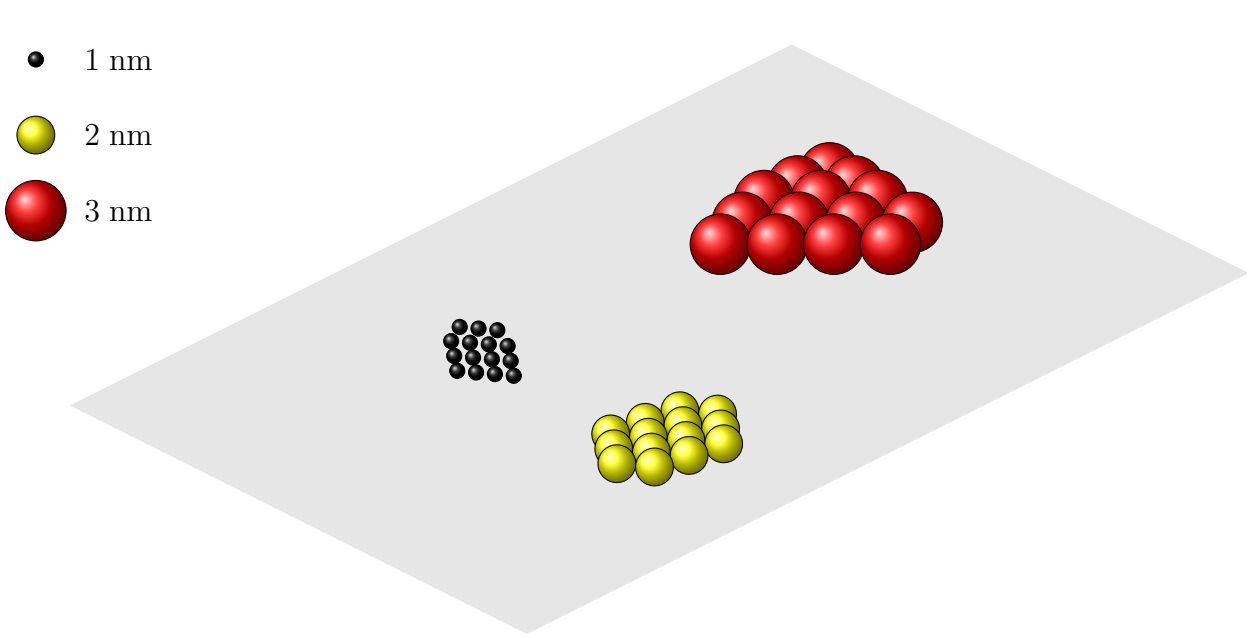

Figure 2.7: Diagram showing the perspective of number, volume, and surface weighted distributions

The number average diameter as determined by TEM is given by:

$$d_n = \frac{\Sigma n_i d_i}{\Sigma n_i}$$

where d is the diameter and, n the the particle number in increment i.

The surface average diameter d_s is determined by

$$d_s = \frac{\Sigma n_i d_i^3}{\Sigma n_i d_i^2}$$

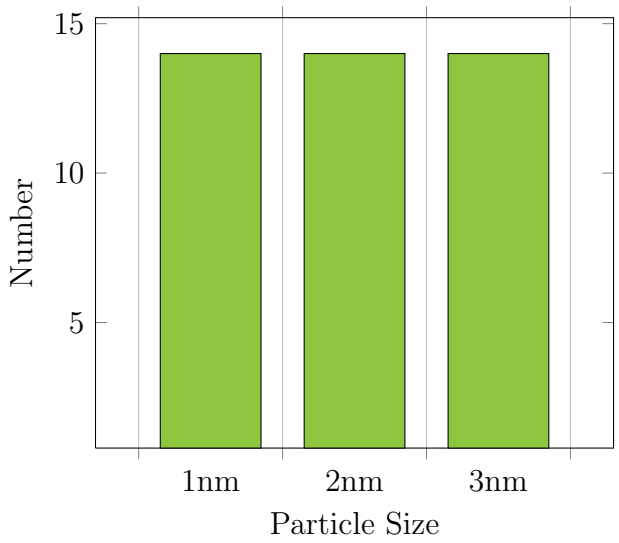

Figure 2.8: Bar chart showing number weighted sampling distribution perspective

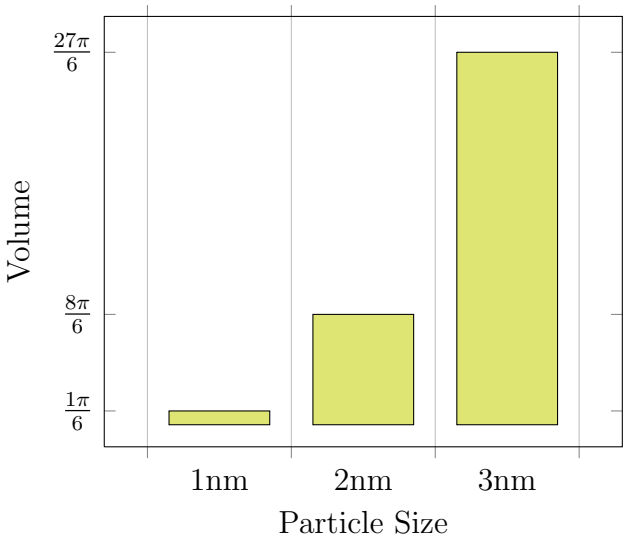

Figure 2.9: Bar chart showing volume weighted sampling distribution perspective

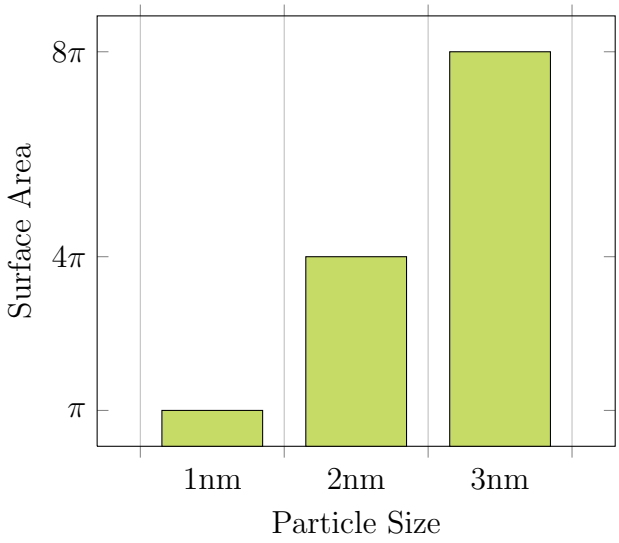

Figure 2.10: Bar chart showing surface area weighted sampling distribution perspective

the volume average diameter d_v is given by:

$$d_v = \frac{\Sigma n_i d_i^4}{\Sigma n_i d_i^3}$$

the volume area average diameter d_{VA}, as determined by chemisorption is given by:

$$d_{VA} = 6\frac{V_M}{SA_M}$$

where M indicates metal, V is the volume per metal atom, and SA is the surface area.

The four main techniques considered for average particle size determination are based on either a physical or a chemical principle. Electron microscopy and X-ray diffraction and based on direct observation, while X-ray photoelectron spectroscopy can be said to estimate mean particle size somewhat indirectly. Chemisorption is based on the chemical interaction of gas molecules with the particles on the surface.

Electron microscopy and X-ray diffraction are the most widespread technique for particle size determination. A simple search on Elsevier's ScienceDirect website for the technique and particle size (at the time of the preparation of this document) revealed 224,386 EM articles, 114, 725 XRD articles, 34,011 XPS articles, and 21,061 chemisorption articles.

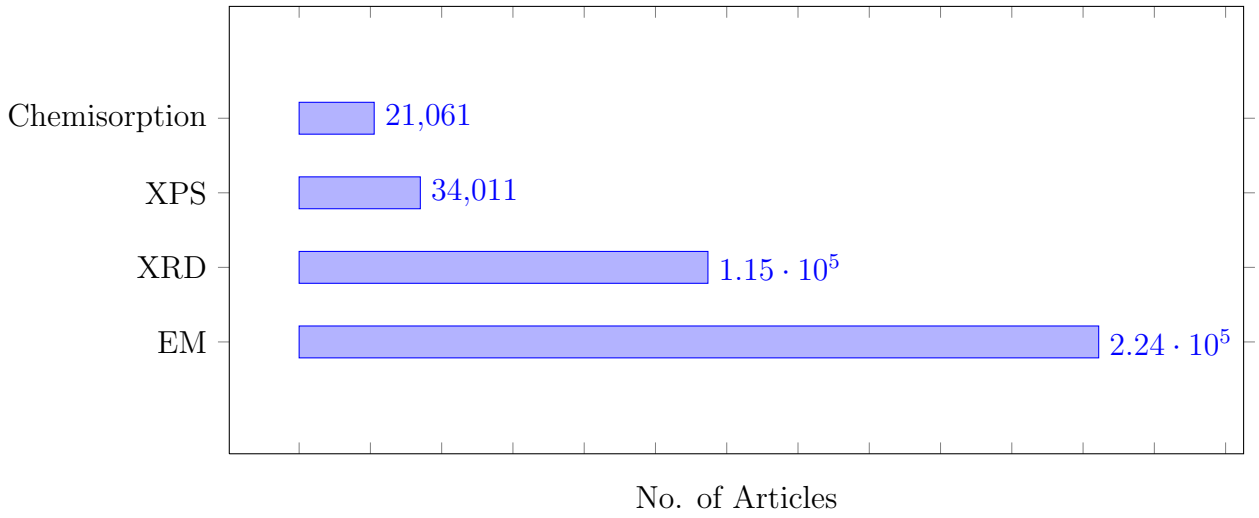

Figure 2.11: Frequency of the comparative techniques used for crystallite size determination as documented by ScienceDirect, June 2012

Comparison techniques that are in agreement with each other that give reproducible and reliable results are essential in particle size determination. Firstly, when selecting comparison techniques, it is important that the weighted mean measurement be understood. The notion of a weighted mean describes how each data point contributes equally to the final average. Table 2.2 lists the four techniques and their corresponding weight basis. The literature

has several accounts of particle size comparison using a combination of two or more of the techniques - XPS, XRD, EM, and/or chemisorption [27–29, 31, 34, 67–71].

Table 2.2: Characterization Techniques Discussed in this Work

Technique	In	Out	Average Weight	Information
Chemisorption	Gas	Gas	Surface	Surface Area, Dispersion, Particle Size
XPS	X-ray	Electron	Near-Surface	Composition, Dispersion, Oxidation State, Particle Size
XRD	X-ray	X-ray	Volume	Bulk Structure, Particle Size
TEM	Electron	Electron	Perimeter, Number	Particle Size, Structure

Seyedmonir et al [29] and Mustard & Bartholomew [27] used XRD, TEM, and chemisorption to characterize Ag/TiO_2 and supported nickel particles respectively. In determining particle size, Seyedmonir et al reported that there were no silver peaks distinguishable from XRD and that a very small number of crystals (range 3-10 nm) could be easily distinguishable from TEM micrographs. Thus, a possibility of error exists due to the small number, however, there was reasonable agreement between oxygen chemisorption and TEM data for particle size estimation. Mustard & Bartholomew reported that XRD was not accurate in the estimating particle size of supported nickel. TEM was accurate but tedious because samples are difficult to prepare and of the large number of particles that must be counted for accurate analysis. Chemisorption was also accurate and the most convenient. Chemisorption and TEM were found to be in very good and good agreement over a wide range of metal loading Ni/SiO_2 and 15 wt% Ni/Al_2O_3 respectively. There was poor agreement with Ni/TiO_2 suggesting that gaseous adsorption was suppressed. Strong metal support interactions (SMSI) have been reported to cause the causes suppression of thin electron transparent metal crystallite.

Several researchers [28, 34] have used chemisorption with XRD for crystallite size estimations. In comparing XRD and chemisorption, Strohmayer [28] reported poor quantitative

agreement between the two techniques for Ag/TiO_2 and Ag/α-Al_2O_3. The discrepancy was attributable to low sensitivity of the XRD and the possibilities of subsurface oxygen absorbed in the bulk of the Ag crystal during chemisorption. Scholten [34] did not report any aggrement between the two methods.

The influence of particle dimension and size distribution factors limits the accuracy to 30 % in XRD [22]. Very poor correlation between image analysis and laser diffraction exists. Generally, in the literature, XRD did not provide good agreement with the other techniques for particle size estimation [27–29, 31, 69, 71]. Chemisorption showed more aggrement with TEM [27, 29, 31, 71].

In Regalbuto et al.[31] an attempt was made to explain the discrepancy in chemisorption and XRD crystal size determination by XPS for $Pt/WO_3/SiO_2$ catalysts. This attempt was qualitative rather than quantitative in nature. Fung [49] recognized XPS as a desirable technique that can be used in the determination of the size of supported metal particles notably in the region in which XRD is generally insensitive, below 3-5 nm [22, 27, 49, 61, 72]. XPS sees only the outer surface area of a particle - the projected area as the outer surface atom contribute to the majority of the XPS signal. Using the intensity ratios eliminates most of the complexities of reproducing the exact geometry and morphology since these properties are not a determining characteristics of the intensity ratios. The degree of surface atom dispersion, percentage active particle loading, the projected surface area of the particle, and the specific surface area of the support affect the intensity ratios.

XPS is described as a surface weighted means of calculating the average crystallite diameter. Surface weighted is more meaningful with regards to surface analysis in contrast to number and volume weight [70]. Fung disputed the surface weighted claim by proposing that XPS give something between a surface and volume average size, since the surface atoms and atoms below the surface contribute significantly to the intensity of the XPS signal. This is a valid claim when atoms are smaller than 10 nm, as XPS sees the top 10 nm of the surface.

For a Ag particle in 20 wt% Ag/TiO_2, where d = 6.9 nm and λ_{Ag}=1.38 nm. The particle would be $^{6.9}/_{1.38}$ = 5 λ thick. Since in the most ideal case, XPS sees signal up to 5 λ in thickness, XPS would only see the surface atoms i.e., the photoelectron intensity count would arise only from one atomic layer. For smaller particles photoelectron intensity would arise form more than one layer.

Monolayer Perspective/Approach

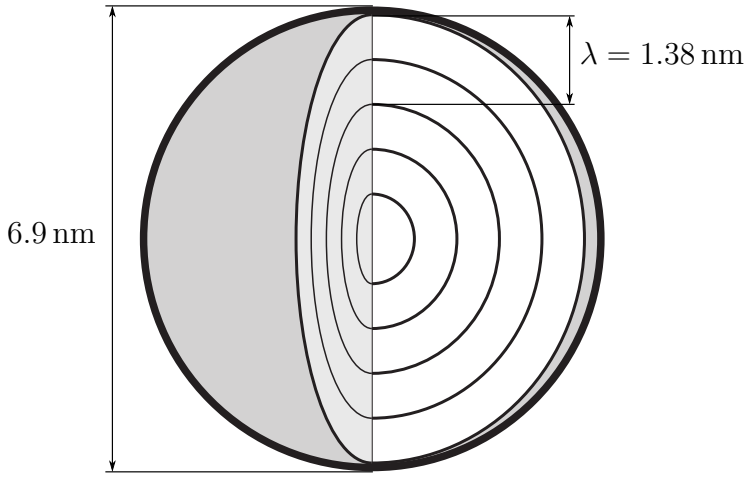

Figure 2.12: Layers of a representative silver particle

Chapter 3

Experimental Methodology

3.1 Introduction

Surface characterization is of crucial importance to the advancement of adsorbent technology. In this process, surface electrons are energized by an external source and are emitted for analysis. The emitted electrons arise from the top few atomic layers of the specimen and are a direct representation of the species at the interface. Information received from the surface species can elucidate properties such as: composition, size, dispersion, reactivity, selectivity, active site, etc.

The two main techniques utilized in this thesis are XPS and oxygen chemisorption. The following sections briefly describe the theory involved in the application of these two techniques.

3.2 X-ray Photoelectron Spectroscopy

X-ray photoelectron spectroscopy (XPS) is the most widely used surface sensitive characterization technique based on the photoelectric effect[38]. XPS give information about the chemical environment of a sample based on binding energy variation. When the surface of a sample is irradiated using an X-ray source, energy is transferred from the photons to the atoms on the surface of a sample. If the photon energy is enough to overcome the attractive forces binding the electron in its orbital, the electron will be emitted so that the atom can regain an energetically stable environment. The emitted electron, photoelectron, powered by the photon energy and kinetic energy are detected by an electron analyzer. Using the

principle of conservation of energy,

$$h_\nu = E_k + E_b + \phi \tag{3.1}$$

where h_ν is the energy of the photon, E_k is the kinetic energy, E_b is the binding energy and ϕ is the work function.

The intensity of the photoelectronic peak for a sample as described by Penn [73] is

$$I = I_0 n \sigma \lambda(\epsilon) D(\epsilon) \tag{3.2}$$

where I_0 is the X-ray flux, n is the density of atoms, σ is the photoelectron cross-section, $\lambda(\epsilon)$ is the mean free path of energy (ϵ), $D(\epsilon)$ the fraction of electrons detected by the analyzer. More complicated forms of this equation exist as described by Briggs and Seah [74] which include more instrumental and morphological parameters; however, this form of the equation has a $\pm$ 10 % uncertainty which is deemed acceptable given the degree of difficulty in acquiring all the different parameters. This form of the equation is referred to as the 'first principle model' (FPM).

The experimental intensity, I,which corresponds to the area under the graph of the XPS peak, is used to determine the atomic concentration, C_x , the of the element in the sample [75]:

$$A \propto C_x \sigma \lambda(\epsilon) D(\epsilon) \tag{3.3}$$

An empirical method using sensitivity factors can also be used to estimate C_x[76]:

$$C_x = \frac{\frac{I_x}{SF_x}}{\sum_i \frac{I_i}{SF_i}} \tag{3.4}$$

where SF_x is the atomic sensitivity factor for element x. The SF is directly proportional to the cross-section, the inelastic mean free path for the photoelectron core, level and several

parameters that are dependent on the experimental conditions. Thus, all instrumental factors are grouped into the SF, which is given by Wagner et al. [77]:

$$SF = \sigma \phi y A T \lambda \tag{3.5}$$

where σ is the photoelectric cross-section for a particular transition cm^2, ϕ is the angular frequency factor, y is efficiency of production, A is the sample illuminated area, T is the detector efficiency, and λ is the mean free path of photoelectrons. A list of sensitivity factors are reported in the literature for a large number of elements using the F 1s line [77].

This method is however prone to lower accuracy than XPS measurement intensity derived from FPM [78]. Wertheim [75] states that there is no possibility of defining universally accepted applicable sensitivity factors. This is because the area of the main line that depends on the fraction of events accompanied by the multi-electron process varies among atoms and materials. Also, several issues arise for the transferability of SF between instruments. In this study, the FPM was applied to determine the atomic concentration.

3.2.1 Experimental

The XPS system consists of non-monochromatic Leybold-Heraeus LHS-10 spectrometer with a dual anode Al/Mg X-ray source and hemispherical electron energy analyzer (HSA). XPS measurements were taken with an X-ray source typically requiring between 100 W and 350 W of power. The system typically yielded a 1.2 eV FWHM for the Au($4f_{7/2}$) photoelectron peak of a gold foil using a Mg Kα anode at a workable spectrometer pass energy and count rate. The measurement uncertainty was recorded as $\pm$ 0.2 eV. The samples were mounted on carbon, high-vacuum compatible, double-sided adhesive tape. Sorbent samples were introduced into the load lock and degassed to pressures of ca. 1 $\times 10^{-6}$ Torr. Subsequently, the samples were inserted into the main chamber where measurements were taken at a residual pressure of ca. 1 $\times 10^{-7}$ Torr. Al Kα (hν =1486.6 eV) or Mg Kα (hν

=1253.6 eV) x-ray source was used at spectrometer operating conditions of 10 mA and 50 eV. XPS data were fitted using the XPSPEAK41 program. Sample charging was compensated for by adjusting XPS settings to the C 1s peak at 284.6 eV. The samples were assessed to ensure that the shoulder was not the result of artifacts due to system contamination. Atomic ratios were derived using the analysis of the elemental peak areas and following well established methods for XPS data analysis [42, 46, 73–75, 77, 79]. Peak deconvolution was performed using a nonlinear Shirley baseline and a combination of Gaussian and Lorentzian type curves.

3.3 Oxygen Chemisorption

Chemisorption is an analytical adsorption technique (widely used in heterogenous catalysis) that is based on chemical interactions occurring between the the adsorbate gas and the exposed surface of a catalytic material. Chemisorption is used to reveal information about a variety of surface properties. These include but are not limited to: the active metal surface area, dispersion of the active metal, surface energy, reducibility and oxidizability of the catalytic material, and crystallite size. In this work, information from selective oxygen chemisorption was used specifically to determine the silver crystallite size of the Ag/TiO_2 adsorbent. Oxygen gas was used in preference to other gases such as CO and H_2 as it most readily adsorbed to form a well-defined monolayer coverage (with the least challenges) [28, 80–82].

Selective oxygen chemisorption was used to obtain the active metal surface area at conditions which supported the formation of a monolayer on the surface of the exposed metal atoms. The number of surface metal atoms is obtained from measuring the amount of chemisorbed gas. The amount of oxygen chemisorbed based on the formation of a monolayer was used with the known adsorption stoichiometry between the adsorbate gas and the metal [28, 35, 36, 67, 83]. The metal surface area is given by:

$$ASA = N_m SA_m N_A \tag{3.6}$$

where ASA is the active surface area of the metal atoms (m^2/g), N_m is the oxygen monolayer uptake (moles/g), S is the adsorption stoichiometry, A_m is the cross-sectional area of the active metal surface atom (Å/ Ag atom), and N_A is Avogadro's number (atom/moles).

Metal crystallite size was determined by estimating the volume from the mass and the density of the supported metal, using the ASA, and by assuming a geometry of the crystallite. The geometries assumed were (i) spherical, (ii) hemispherical, and (iii) cubic. The average crystallite size is given by:

$$d = \frac{Lf}{ASA \cdot \rho_m} \tag{3.7}$$

where d is the particle diameter, L is the percent metal loading, ρ_m is the density of the supported metal, and f is the particle shape correction factor ($f = 6$ for spherical and hemispherical particles and $f = 5$ for cubic particles see Section C.3).

3.3.1 Experimental

The Quantachrome Autosorb-1 was used to perform oxygen chemisorption using that static chemisorption technique [82]. Three pretreatment steps were carried out for oxygen chemisorption: firstly, ~ 5 mg of the adsorbent pellets were heated to 150°C followed by an evacuation at 2.99×10^{-9} Torr for 30 minutes to remove the moisture and contaminants from the surface. Secondly, hydrogen reduction at 300°C and 760 Torr for 60 minutes to provide reducible oxygen uptake. Thirdly, evacuation at 300°C and 2.99×10^{-9} Torr for 60 minutes for the removal of physisorbed hydrogen. Oxygen uptake was recorded at 170°C after saturation of the surface was reached. The effluent gases were continuously monitored with a mass spectrometer. The Brunaur-Emmett-Teller (BET) surface areas were measured from nitrogen gas adsorption-desortpion at 77 K. The average sizes of the dispersed crystallites were derived from the active surface area.

3.4 Electron Paramagnetic Resonance

Electron Paramagnetic Resonance (EPR) is a spectroscopic technique that is used to detect chemical species that have unpaired electrons. It is the measurement and interpretation of the energy differences between the atomic or molecular states and is used to increase knowledge about the structure of molecules and probe the adsorbate-surface interactions by analyzing a molecular absorption spectra which arise when the frequency and the amount of the electromagnetic radiation is changed as it passes through a sample.

EPR is based on the interaction of electromagnetic radiation with magnetic moments arising from electrons. In EPR the intensity, the number of absorption lines and the line position is used to identify different nuclei. Intensity is purely a property of the electron,but can be correlated to a metal when the metal content is known.

Line positions in EPR are stated in g values which is a function of the ratio of the frequency to the resonant field. The relationship describing the absorption of microwave energy between two spin states is

$$\Delta E = h\nu = gbB$$

where:

ΔE is the energy difference between the two spin states

h is Planck's constant

ν is the microwave frequency

g is the Zeeman splitting factor

b is the Bohr magneton

B is the applied magnetic field.

EPR is used as a complementary technique to characterize the adsorbate surface system, information can only be obtained if the system is paramagnetic. Thus, in the $AgTiO_2$ system we can only gain direct information on the Ag^{2+} paramagnetic species.

3.4.1 Experimental

The EPR system consists of a Bruker EMX-6/1 X-band EPR spectrometer composed of: an EMX 1/3 console, an ER 041 X61 bridge microwave bridge with built-in microwave frequency counter, an ER070 magnet, and an ER-410410st standard universal rectangular angular cavity. Data acquisition was performed with the software supplied by Bruker (WINEPR acquisition program), data manipulation (determination of g-values, subtraction, base lining, integration and conversion to ASCII files for use with Origin or Microsoft Excel) was done with the WINEPR program version 2.11.

Experimental

Ag/TiO_2 samples were prepared by the method described previously. Prepared samples were cooled with liquid nitrogen to 77 K in a finger dewar. Spectra of the as-prepared sorbent were recorded with a field modulation frequency of 100 kHz, a modulation amplitude of 10 mT, a frequency of 9.37 GHz, and a power supply of 2 mW.

Chapter 4

Experimental Results

This chapter details the results of the different techniques used to characterize the physiochemical properties of the Ag/TiO_2 adsorbent system. XPS and oxygen chemisorption were the principal techniques employed in this study. XRD data was not presented in the study due to problems determining particle size at low weight percent loadings.

4.1 XPS Analysis

The XPS survey spectra revealed significant compositions of the following elements: Ag, Ti, O, C. The measurement sequence and procedure for all samples were the same. A 20 eV and a 50 eV spectra were recorded for all samples in the following sequence: C(1s), Survey, Ag(3d), Ti(2p), O(1s), C(1s). The spectra were referenced to the adventitious C 1s peak at 284.6 eV. Variation in spectrometer intensity was accounted for by taking the intensity of the C(1s) peak at the beginning and end of each sequence.

The XPS spectra in Figure 4.1 show the experimental data of the Ag 3d doublets of Ag/TiO_2 adsorbents ranging in silver loading from 1 wt% - 20 wt%. As expected, the studies indicated that the Ag content on the support increased with Ag loading; also, as is reported in the literature, the Ag 3d doublet maintained its characteristic features: a peak separation of 6.0 eV and an area ratio of 2:3 [76, 77, 85]

The Ag signal intensity was below the detection limit of the XPS at the 1 wt% loading; a weak signal was detected at the 2 wt% loading and from there the Ag peak intensity increased in prominence up to 20 wt% loading. The spectra showed a slight shift toward a lower binding energy (BE) of the Ag 3d doublet peaks at the 12 wt% loading and 20 wt% loading. A shift in the binding energy is a result of a change in the chemical bonding

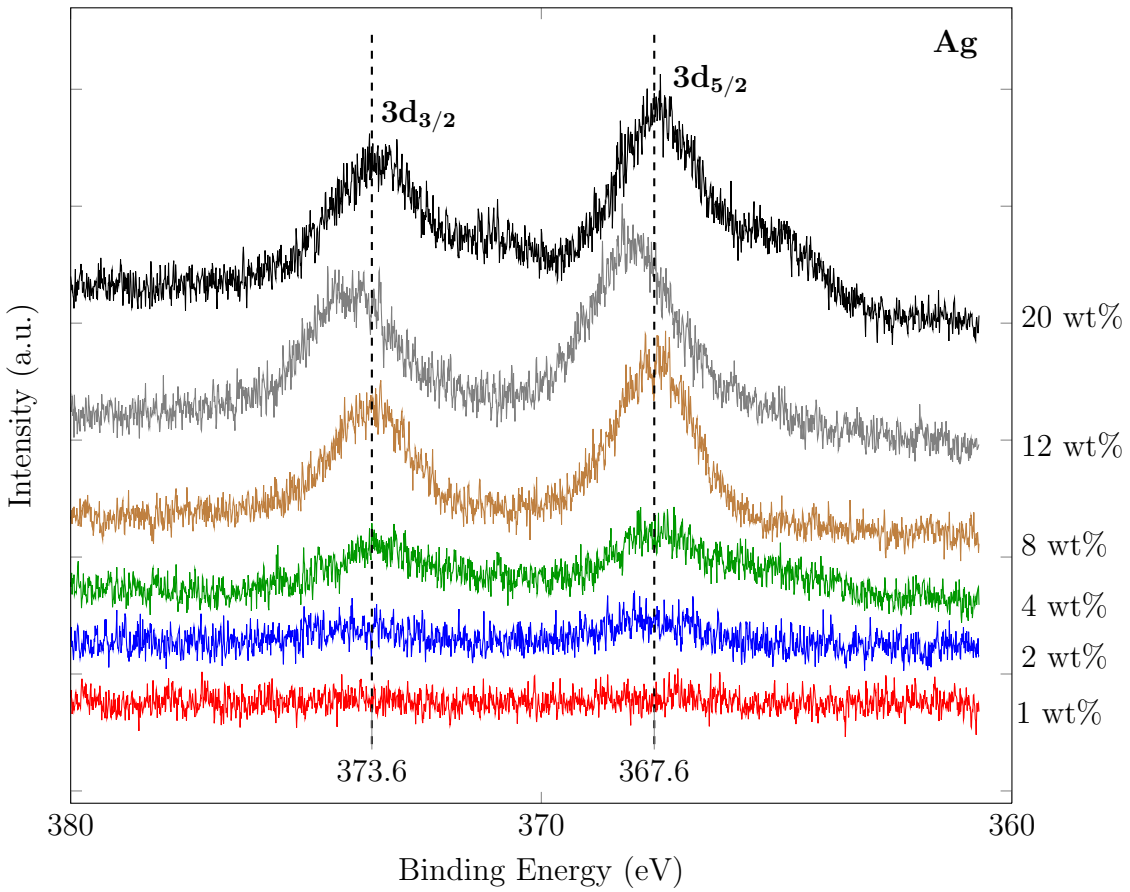

Figure 4.1: XPS spectra of the Ag/TiO_2 $Ag(3d_{3/2}, 3d_{5/2})$ peaks

of the atoms in a solid. Several factors such as valence electron density, lattice potential, work function, and atomic relaxation energy are reported to influence a shift in BE [85, 86]. If ionic charge or oxidation state were the only factors to be considered, then it could be concluded that Ag was reduced. However, the anomalous nature of the BE of Ag oxides compared to that of Ag metal is such that there is a negative shift in BE from Ag^0 to $Ag^{1+,\,2+}$ [87, 88]. Normally in the literature, most metal to metal oxides systems exhibit positive binding energy shifts. Changes in oxidation state of Ag could not be determined due to the slight differences in BE values using the $(3d_{5/2})$ peak binding energies Ag^0 (368.2 eV), Ag^{1+} (367.7 eV), and Ag^{2+} (367.4 eV) [76, 85, 87]. Additionally, this determination was beyond the sensitivity of the non-monochromatic LHS-10 XPS system which had an

uncertainty of ± 0.2 eV. Table 4.1 shows the values of the BE of Ag($3d_{5/2}$) peak in Ag, Ag_2O, and AgO found in literature.

Table 4.1: BE of Ag($3d_{5/2}$) Peak in Ag, Ag_2O, and AgO

Compound	Binding Energy (eV)	Reference
Ag	368.1 ± 0.1	Schön [87]
Ag	368.0	Gaarenstrom [85]
Ag	367.9	Wagner [76]
Ag	367.9 ± 0.2	This work
Ag_2O	367.7 ± 0.2	Schön [87]
Ag_2O	367.6	Gaarenstrom [85]
AgO	367.8	Wagner [76]
AgO	367.4 ± 0.2	Schön [87]
AgO	367.2	Gaarenstrom [85]

The decomposition of the Ag 3d photoemission spectra is shown in Figure 4.2. Peak deconvolution was accomplished using the XPSPeak41 software. Photoelectron lines have a Lorentzian shape corresponding to the lifetime of the core hole that is created; if all the features were ideal a strictly Lorentzian curve would be used. However, a combination of Gaussian-Lorentzian curve was used to account for non-idealities in the system; instrumental factors such as the width of the x-ray line and the analyzer resolution. This mixed curve ratio was employed for the entire analysis. Symetrical line shapes were used for all elements. Several parameter constraints were employed in consideration of known physical constants of Ag in order to obey the chemistry. These parameters were: the peak symmetry - defined by the p-subshell, a doublet separation of 6.0 ± 0.2 eV, and the relative intensities for p electrons, 1:2. A proper background was also necessary to obey the chemistry and physics involved in the system. A blend of the Shirley and linear backgrounds was used to satisfy the 1:2 ratio of the p doublet. The Gaussian-Lorentzian curve ratio, the relative intensity 2p doublet area ratio, and the peak separation were all fixed. The FWHM of the peaks were constrained within a range. The use of the physical constants and constraints should reduce ambiguity, elucidate underlying peaks, and eliminate the introduction of biases that would

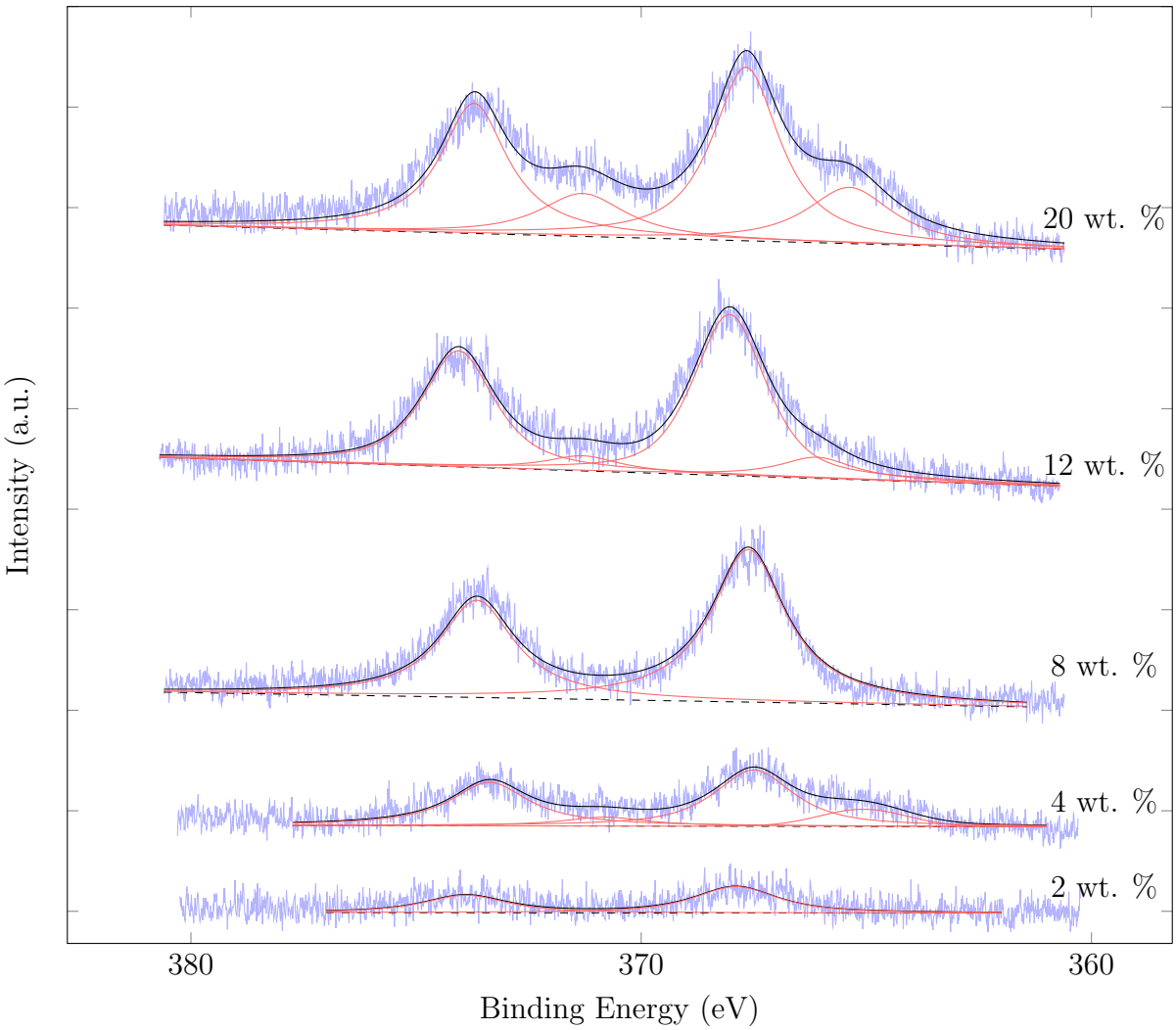

Figure 4.2: Deconvolution of XPS spectra of the Ag/TiO_2 $Ag(3d_{3/2}, 3d_{5/2})$ peaks

result in a loss of the contribution of other peaks. The peaks were fitted with a fair degree of certainty because of these physical constants and constraints .

The prominent shoulders displayed in the 20 wt% loading were attributed to the occurrence of a second doublet component. The Ag silver at the 12 wt% loading showed an anomaly in that the BE of the Ag 3d peak displayed the highest BE of all the sample analyzed. This occurrence was independently verified [89]. The 4, 12 and 20 wt% loading were decomposed into two doublets. The multiple occurrence and growth of the second doublet suggest that this is not an artifact resulting from system contamination. The second doublet suggests the occurrence of multiple species of Ag_xO_x. Table 4.2 shows the BE and the

FWHM values for the components of the XPS Ag 3d spectra. The BE of the silver oxides decrease in the order Ag_m – Ag_2O – AgO while the FWHM increases and the peaks get broader. The first Ag component is assigned to Ag_2O with Ag $3d_{5/2}$ located at 365.6 ± 0.2 eV as is reported in literature (see Table 4.1). The FWHM of this component decreases with increasing weight loading. The second component Ag peak is assigned to AgO. AgO is reported to have two chemically inequivalent silver atoms with chemical formula $Ag^{I}Ag^{III}O_2$. Ag^{I} has two oxygen atoms and Ag^{III} with four oxygen atoms [87].

Oxygen displays distinctive features which are characteristic to metallic silver and Ag_xO_x compounds; Ag^0 has a peak at 532.2 eV, Ag^{1+} has two peaks at 529.0 eV and 530.4 eV, and Ag^{2+} has two peak at 528.4 eV and 530.3 eV [87]. The analyses of the Ag 3d and O 1s peaks Figures 4.3 and 4.2 lead to the conclusion that the peak occurring at approximately 529.5 eV can be assigned to TiO_2. There is most likely a small contribution from Ag_2O and AgO, but that contribution could not be extracted from this data with great fidelity. However, it can be concluded that the oxygen peaks show the presence of multiple species. The change from one component to two component in the oxygen peak could be due to continuously changing oxygen absorbed on Ag_2O to metallic Ag noted in metal-oxygen systems reported in Schön [87]. Previous TPR investigations revealed that Ag is present in its oxide state as Ag^{1+} with minor concentrations present as Ag^{2+} [21].

Table 4.2: FWHM and BE of Ag-3d Peaks

Ag/TiO_2	Binding Energy (eV)							
	Component 1				Component 2			
Loading	$Ag(3d_{3/2})$	FWHM	$Ag(3d_{5/2})$	FWHM	$Ag(3d_{3/2})$	FWHM	$Ag(3d_{5/2})$	FWHM
1 wt%	UD	UD	UD	UD	UD	UD	UD	UD
2 wt%	373.9	2.3	367.9	2.3	UD	UD	UD	UD
4 wt%	373.5	2.1	367.5	2.1	370.8	2.1	365.1	2.1
8 wt%	373.7	2.1	367.6	2.1	UD	UD	UD	UD
12 wt%	374.0	2.0	368.0	2.0	371.3	2.0	365.3	2.0
20 wt%	373.7	1.9	367.7	1.9	371.3	2.3	365.3	2.3

UD - undetectable
† uncertainty ± 0.2 eV

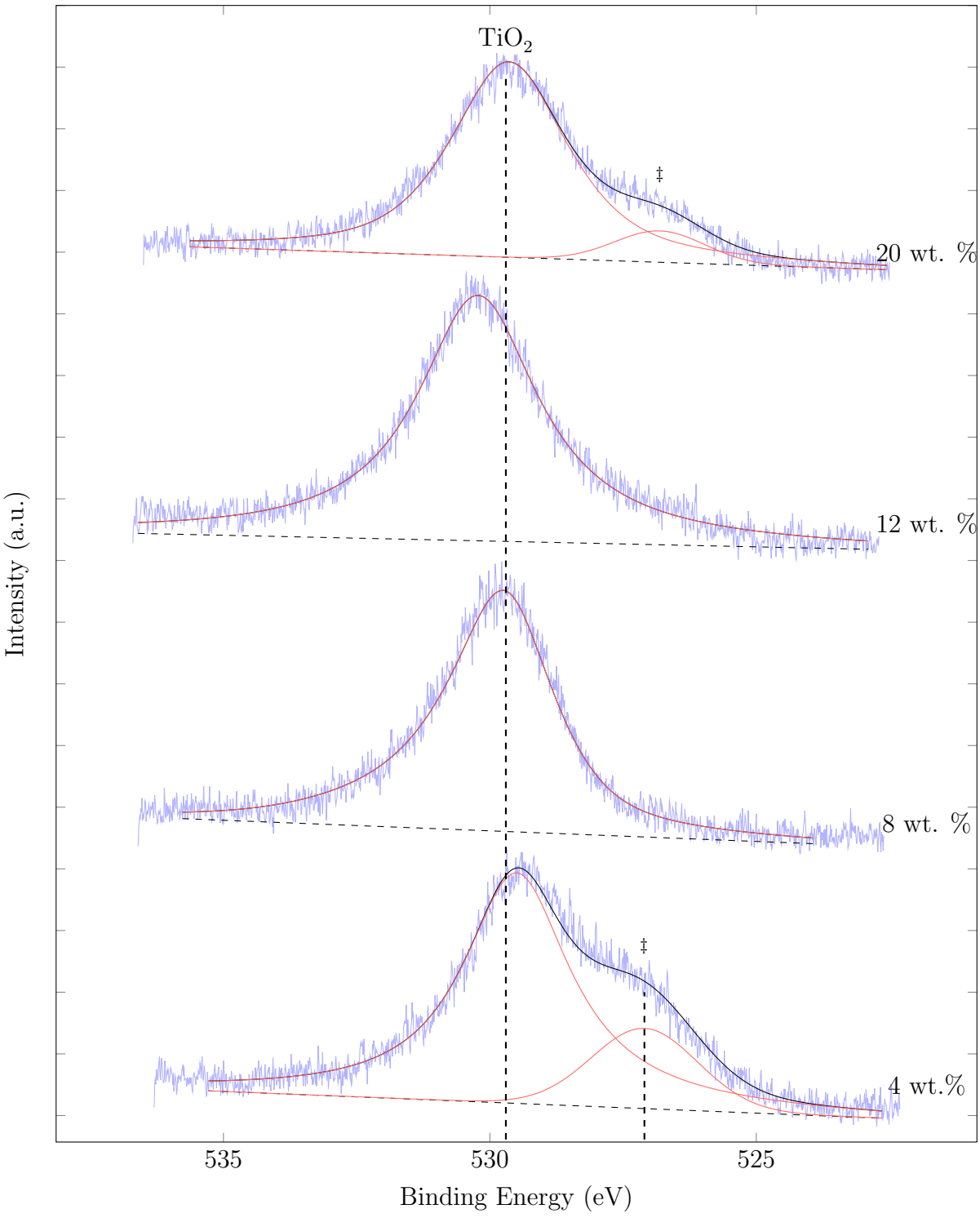

‡ - indicates multiple oxygen species.

Figure 4.3: Oxygen 1s spectra of various loading of Ag/TiO_2 adsorbents

4.1.1 Atomic Ratios

Atomic ratios derived from the XPS data are listed in Table 4.3. These ratio were calculated using a simplified version of the FPM model - Equation 3.3. Quantitative measurements had ± 10% uncertainty. On analysis of the data, it was found that Ti($2p_{3/2}$) was a more suitable reference due to its stability. The BE of the carbon 1s peak shifted because of the existence of major secondary carbon species/component. For comparison, atomic ratios referenced to carbon are listed in Table B.2.

Table 4.3: Atomic Ratio of Surface Species on Ag/TiO_2 Adsorbent Pellets

	Ag/TiO_2 Loading					
Element	1wt%	2wt%	4wt%	8wt%	12wt%	20wt%
C-1s	0.25	0.31	0.21	0.19	0.19	0.22
O-1s	0.52	0.51	0.53	0.52	0.51	0.46
TiO_2-2p	0.23	0.17	0.23	0.23	0.23	0.22
Ag-3d	UD	0.01	0.03	0.06	0.08	0.10
Theoretical Ag†	0.008	0.015	0.03	0.06	0.09	0.15
Total	1.00	1.00	1.00	1.00	1.00	1.00
	Stoichiometric Ratios					
O/Ti	2.25	2.90	2.26	2.20	2.26	2.14
Ag/O	—	0.02	0.06	0.14	0.16	0.22
Ag/Ti	—	0.06	0.14	0.28	0.35	0.48

‡ - uncertainty ± 10%

UD - undetectable

† - calculated based on the Ag deposited on specimen.

The atomic ratios of TiO_2 are fairly constant for all the weight loadings, except for the 2 wt% loading. This shows that the titania support was not appreciably obscured by the silver deposited. Supporting quantitative evidence is shown in Appendix C.1 The deviation in the 2 wt% sample can be explained by the increased levels of carbon which suggested carbon contamination. Similarly, the atomic ratios of oxygen are fairly constant across the various loadings, except for the 20 wt% sample where it is hypothesized that reduction took place. The O/Ti ratios did vary at the 2 and 20 wt% loadings. It is believed that deviated

occurred at the 2 wt% due to carbon contamination and at 20 wt% as a result of some chemical structural change.

4.1.2 Dispersion

Information regarding the dispersion and particle size of silver particles on titanium oxide support was extracted using the XPS. XPS has been well established as a technique for studying dispersion of metal on supported systems [33, 39–44, 50, 66, 90–93]. Figure 4.19 shows the intensities of the active particles relative to the support versus the mole fraction as detected by the XPS for various loadings of silver particles. The XPS intensity ratio for Ag/TiO_2 increases with additional loadings of silver. There is a linear relationship observed at lower loadings of less than 0.03 mole fraction (<4 wt%) which suggests that silver is highly dispersed on the titanium oxide support up to a certain critical value. At this critical value, theorized to be between 4 and 5 wt% , increased silver loading deviates from the linear trend and levels off smoothly. This points to the growth of silver particles. Initially, particles are likely to be of uniform distribution and are well dispersed on the surface of the support until they reach a critical loading where the particles begin to grow in size. Similar trends have been observed in the literature [40, 93, 95]. Briggs [40] observed the peak areas of metal catalysts supported on silica versus the wt% metal loading in M/SiO_2 catalyst[1] and Park [93] observed the XPS Cr 2p/Al 2p intensity ratios. This theory is also supported by the fact that sulfur capacity for the Ag/TiO_2 adsorbent increases with weight loading up to a critical value, between 4 and 5 wt% after which increased loading does not increase sulfur capacity [1].

The dashed line in Figure 4.4 exemplifies the trend that would result if the silver-to-titania intensity ratios exhibited a strong linear dependence with loading; however, the experimental values, as indicated by the solid line, did not show this dependence. This dependence was calculated assuming all the silver was atomically dispersed and every atom

[1]the identity of M was not disclosed

was accessible (best case scenario). The 2, 4, and 8 wt% Ag/TiO_2 loadings conformed to uniform dispersion as revealed by the values in Table 4.4. At the 12 wt% the experimental value falls slightly below the calculated values and at 20 wt%, the adsorbent with the highest loading, the value falls significantly below linear dispersion line. It is important to note that high and uniform dispersion is important to gain the greatest access to the active atoms of the adsorbent.

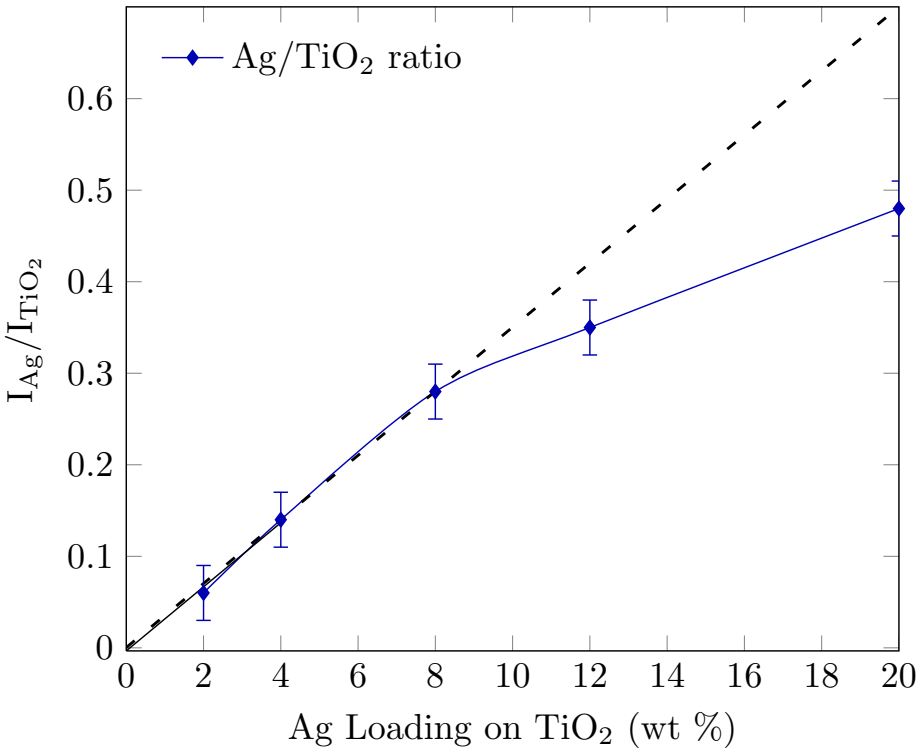

Figure 4.4: Ag/Ti ratio as a function of weight loading of Ag

Table 4.4: Silver-Titania Intensity Ratios - Experimental vs Calculated

Element Ratio	Ag/TiO_2 Loading						
I_{Ag}/I_{Ti}	0wt%	1wt%	2wt%	4wt%	8wt%	12wt%	20wt%
Experimental	0	UD	0.06	0.14	0.28	0.35	0.48
Calculated	0	0.04	0.07	0.14	0.28	0.42	0.70

‡ - uncertainty ± 10%

UD - undetectable

† - Assuming no nucleation and uniform dispersion

∓- Calculated values are based on a linear line through 2 & 4 wt % loading

Several calculations were performed to investigate the silver surface area i.e. the accessible silver atoms, covering the titania support. In these calculations, the following assumptions were made:

- The Ag crystals are an ordered packing of particles that are uniformly and equally dispersed on the TiO_2 support.
- The shape of the Ag particle was (i) spherical and (ii) hemispherical (ii) cubic, see Figure 4.5.
- The Ag particles occupy the intersection of points of a square matrix on the support.
- All Ag particles occupy a position on the surface.
- The surface shielded by the base of a single hemisphere is the same as that shielded by a sphere.

Figure 4.5 gives a pictorial description of some of the assumptions (not drawn to scale). Detailed calculations can be seen in Appendix C.1. These calculations employed the results of oxygen chemisorption particle size determination to derive surface coverage. It show that maximum surface coverage of spherical and hemispherical shaped particles were 2.76 % and 5.52 % respectively,[2] of the total surface area of the support. Thus, supporting the XPS results[3] that showed there was minimal shadowing of the TiO_2 surface area by the silver particles. Table C.1 summarizes the calculated surface coverage results for 4, 8, 12 and 20 % wt Ag loading. XPS was used to gain a more accurate estimation of particle size.

4.1.3 Particle Size

In addition to dispersion, the properties of a catalyst are to a large extent dependent on particle size. However, the atomic size difficult to predict. Difficulties arise in compounds

[2]Ag deposited at the 20 wt% loading produced the largest particles.
[3]See atomic ratios - section 4.1.1

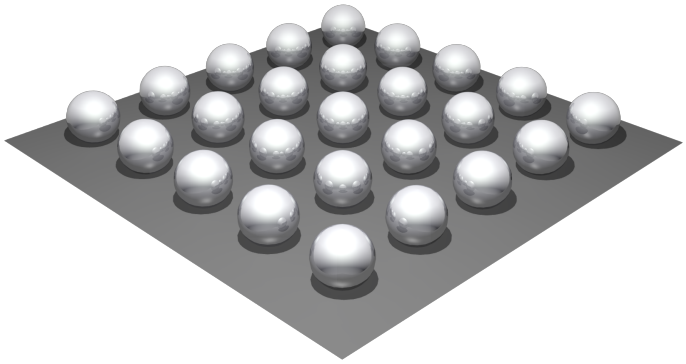

(a) Spheres

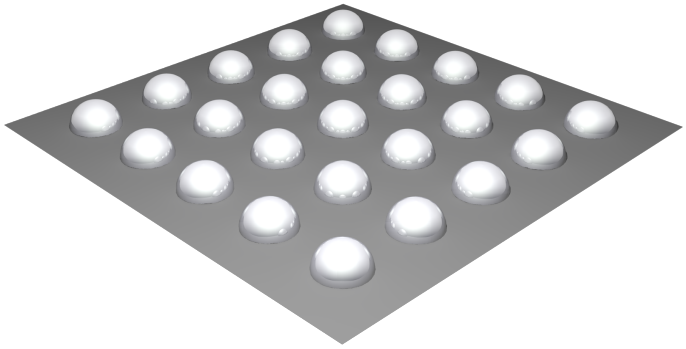

(b) Hemispheres

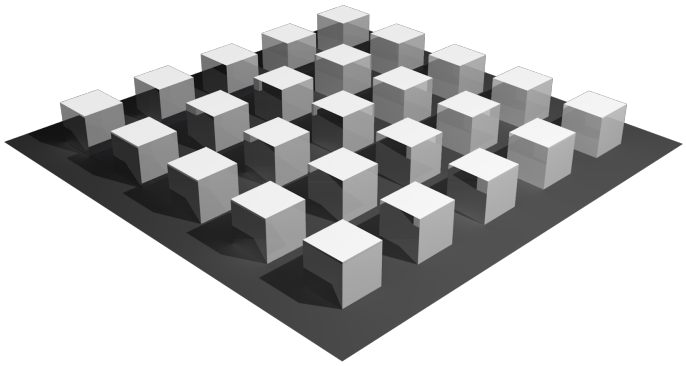

(c) Cubes

Figure 4.5: Isometric View - Particles of different geometries - Not dawn to scale

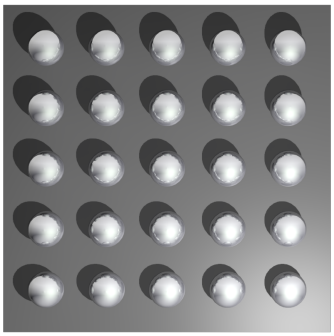

(a) Spheres

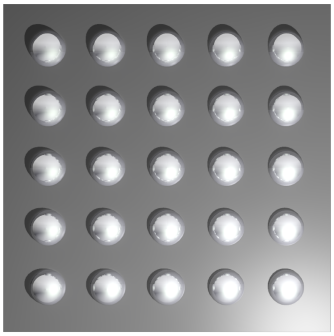

(b) Hemispheres

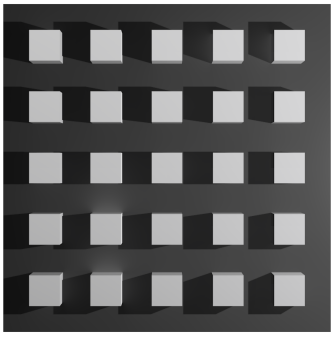

(c) Cubes

Figure 4.6: Top View - Particles of different geometries - Not dawn to scale

because of nearest neighbors interactions and the resulting perturbation on the electron charge cloud. Despite these difficulties, a best estimation is a useful starting point. Particle size was derived using the techniques, chemisorption and XPS. The underlying assumptions associated with each technique was outlined in Chapter 2.

In the literature, there are several instances where Ag has been shown to have various geometries when deposited on various support including titania [29, 67, 96]. Thus, three different geometries were explored. Table 4.6 lists the average crystallite size determined using oxygen chemisorption with the corresponding weight percent loading of Ag for spherical, hemispherical, and cubic geometries. These results are also shown graphically in Figure 4.5. The graph in Figure 4.7 indicates that average crystallite size increased linearly with Ag loading. Note that on this graph the crystal size approximations of the spherical and hemispherical particles geometries were equal. The crystallite size dimensions were derived using the active surface area (ASA) values reported in Table 5 in Nair et al [1] using Egn 3.7. A discrepancy was found in the values reported at the 20 wt% loading. The ASA value corresponded to a value of 8.0 nm (using Egn 3.7) instead of the reported 6.9 nm value. Both values were considered in the analysis.

In Figures 4.7 and 4.8, a line of best fit was drawn on the graphs which could be predictive of the trend on which these results are based. It was noteworthy that the line of best fit fell within the the error bars using the reported crystallite size and the crystallite size calculated due to the reported ASA value at the 20 wt% loading. Thus, the accurate value could not be determined using regression analysis. This analysis showed that assuming chemisorption is correct there is not much difference in assuming a spherical, hemispherical, or cubic geometry.

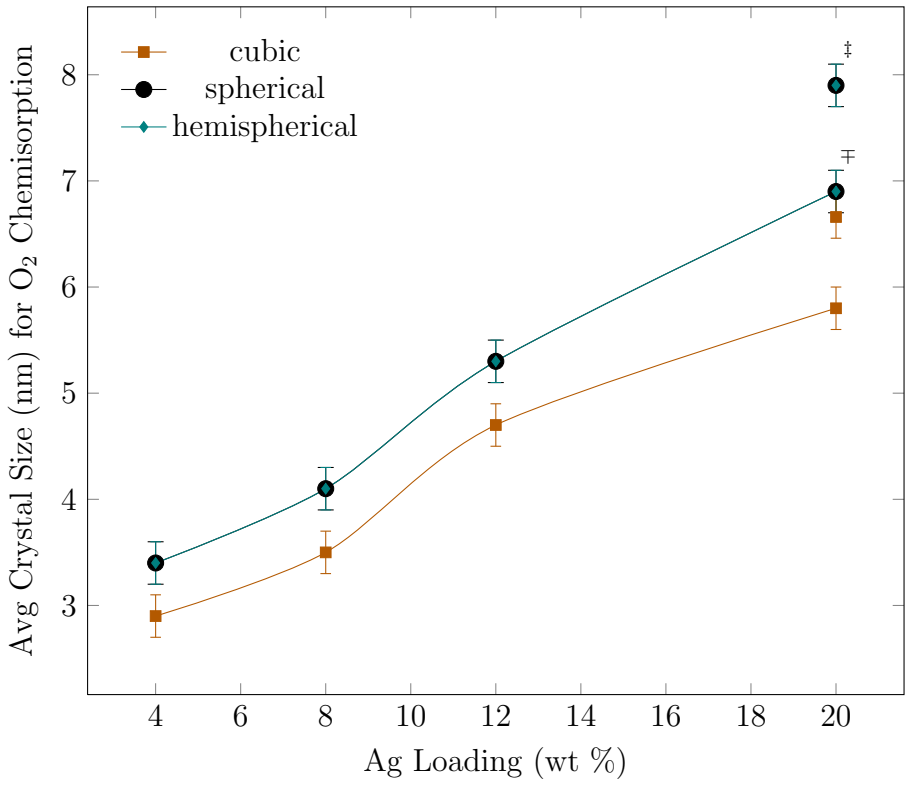

Table 4.5: Trend in average crystal size for Ag particles on TiO_2 determined by O_2 chemisorption -(i) spherical, (ii) hemispherical and, (iii) cubic models

Table 4.6: Crystal Size due to Geometry

Metal Loading (wt%)	Active Surface Area (m^2/g)	Average Crystal Size (nm)		
		Sphere	Hemisphere	Cube
4	6.69	3.4	3.4	2.9
8	10.70	4.1	4.1	3.6
12	12.05	5.3	5.3	4.7
20‡	14.31	8.0	8.0	6.7
20∓	16.50	6.9	6.9	5.8

‡ - dimension calculated based on reported ASA value.

∓- dimension reported in Nair [1].

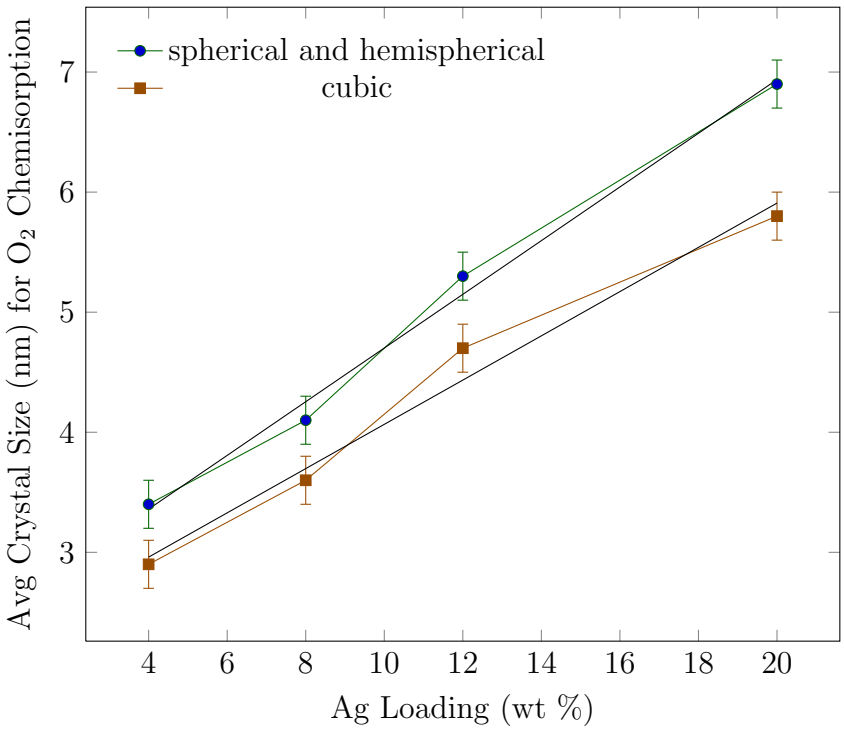

Figure 4.7: Trend in Ag average crystallite size in reported in Nair [1]

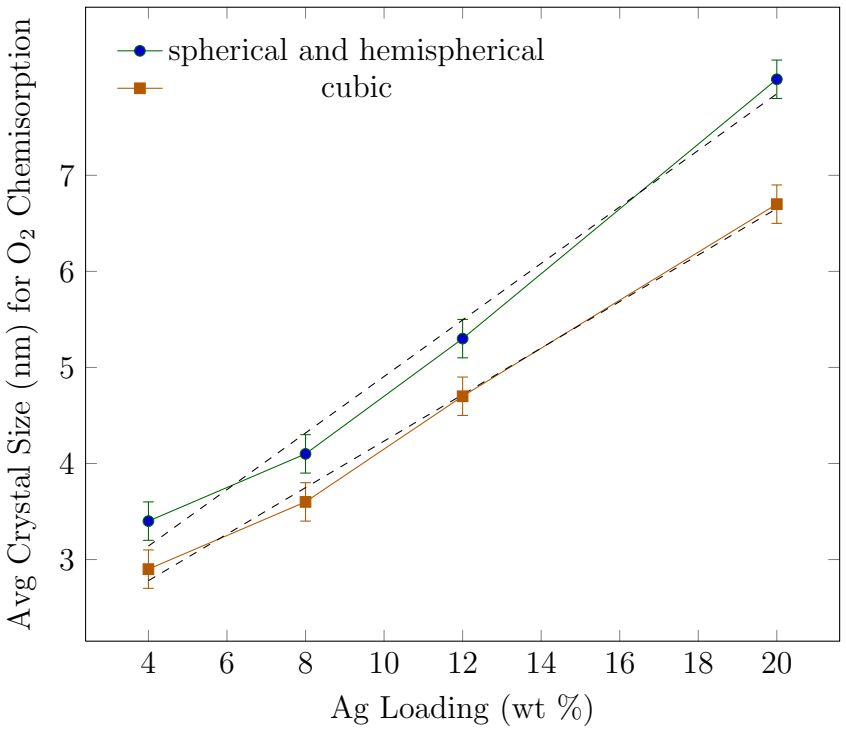

Figure 4.8: Trend in Ag average crystallite size (dimensions calculated based on reported ASA value Nair[1])

In this section, particle size was determined using the method outlined in Kuipers et al. [91]. In this method a general model is derived that allowed the quantification of particle dimension using XPS signal received from the surface/volume ratios of supported phase. XPS intensity ratios determined by surface-to-volume ratios are independent of particle shape [29, 91].

Using the relationship from Kiupers et al. - Equation 1, the signal ratio $I_{\mathrm{Ag}}/I_{\mathrm{TiO_2}}$:

$$\frac{I_{\mathrm{Ag}}}{I_{\mathrm{TiO_2}}} = \frac{I^{\infty}_{\mathrm{Ag}}}{I^{\infty}_{\mathrm{TiO_2}}} \cdot \frac{\theta_{\mathrm{Ag}}\left[1-\exp(-t_{\mathrm{Ag}}/\lambda_{\mathrm{Ag}})\right]}{1-\theta_{\mathrm{Ag}}\left[1-\exp(-t_{\mathrm{Ag}}/\lambda_{\mathrm{TiO_2}})\right]} \tag{4.1}$$

where I is the intensity, ∞ superscript indicates the signal ratio of the pure compound, and λ is the inelastic mean free path (IMFP), θ is geometric surface coverage, parallel to the normals of the underlying support, t is the layer thickness. I^{∞}_{Ag} is estimated for Ag(111) surface plane, see Section C.3. $I^{\infty}_{TiO_2}$ is estimated for TiO_2(001) surface plane, see Section C.4. Several surface common planes of TiO_2 vary within $\pm$ 0.2 of the reported atomic spacing, and spherical particles of diameter $2R_{Ag} = 3t_{Ag}$, where R is the radius, with half the coverage of the layers[97, 98]. XPS cannot distinguish between supported layers of thickness and surface coverage [91]. This fact was used to find the unknown value θ_{Ag} from the relationship:

$$\theta_{\mathrm{Ag}} \cdot t_{\mathrm{Ag}} = \frac{c_{\mathrm{Ag}}}{\rho_{\mathrm{Ag}}\sigma_{\mathrm{TiO_2}}\left(1-c_{\mathrm{Ag}}\right)} \tag{4.2}$$

where ρ is the density , c is the concentration, σ is the specific surface area of the support. The following estimation were employed in various models.

Case 1: Estimate $\mathrm{I_{Ag}/I_{TiO_2}}$ using known particle size values from chemisorption.

1. Use Equation 4.2 then apply Equation 4.1-Using the surface coverage estimation from Table C.1- (this table used the chemisortpion data to estimate surface coverage using (i) spherical (ii) hemispherical and (iii) cubic model), the thickness t_{Ag}, was found. Next, this value was used in Equation 4.1 to find $\mathrm{I_{Ag}/I_{TiO_2}}$. For sample data see Appendix C.5.

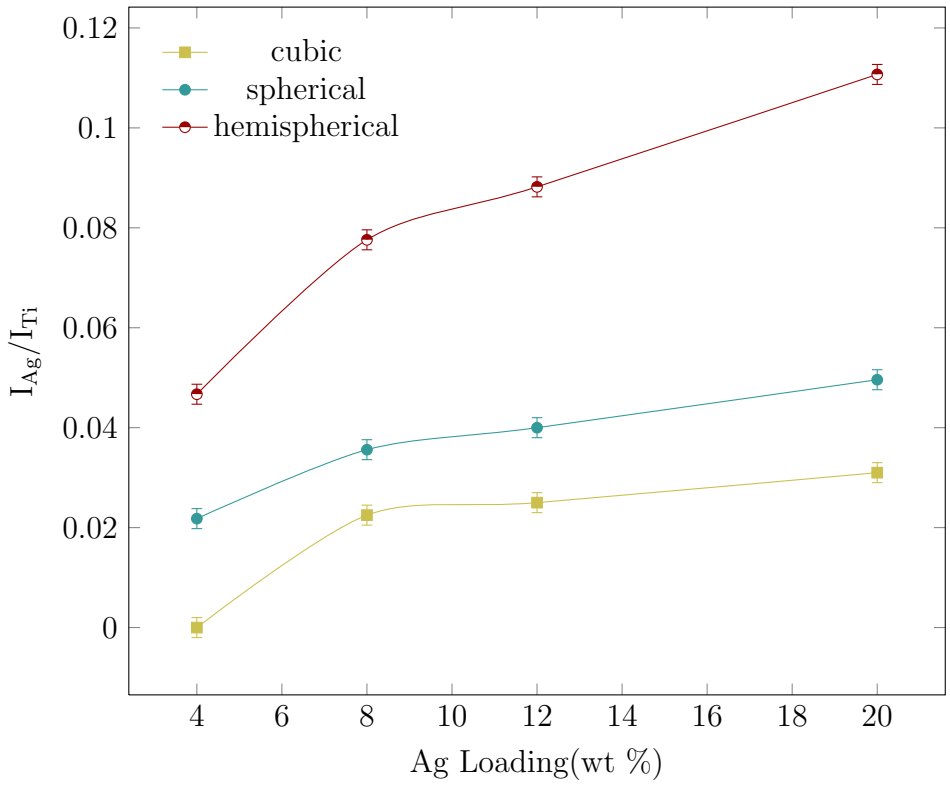

Figure 4.9: Case 1 - Estimation of I_{Ag}/I_{TiO_2} using known particle size values from chemisorption using (i) spherical, (ii) hemispherical, and (iii) cubic models.

Table 4.7: I_{Ag}/I_{TiO_2} Experimental versus Theoretical -Kuipers - Case 1

Ag Loading wt %	I_{Ag}/I_{TiO_2}			
	Experimental	Theoretical		
		Spherical	Hemispherical	Cubic
4	0.14	0.022	0.047	0.000
8	0.28	0.036	0.078	0.022
12	0.35	0.040	0.088	0.025
20	0.48	0.050	0.111	0.031

Three models for particles were assumed (spheres, hemispheres and cubes), the theoretical I_{Ag}/I_{TiO_2} ratio was calculated for the various surface areas. The result showed that the I_{Ag}/I_{TiO_2} ratio increased with increased surface area. The hemispheres had the greatest surface coverage area hence the greatest predicted I_{Ag}/I_{TiO_2} ratio. The three geometric models produced the same basic shape in the graph in Figure 4.9, the corresponding values can be seen in Table 4.7.

2. Use relationship $2R_{Ag} = 3t_{Ag}$ to get θ_{Ag}, then apply Equation 4.1.

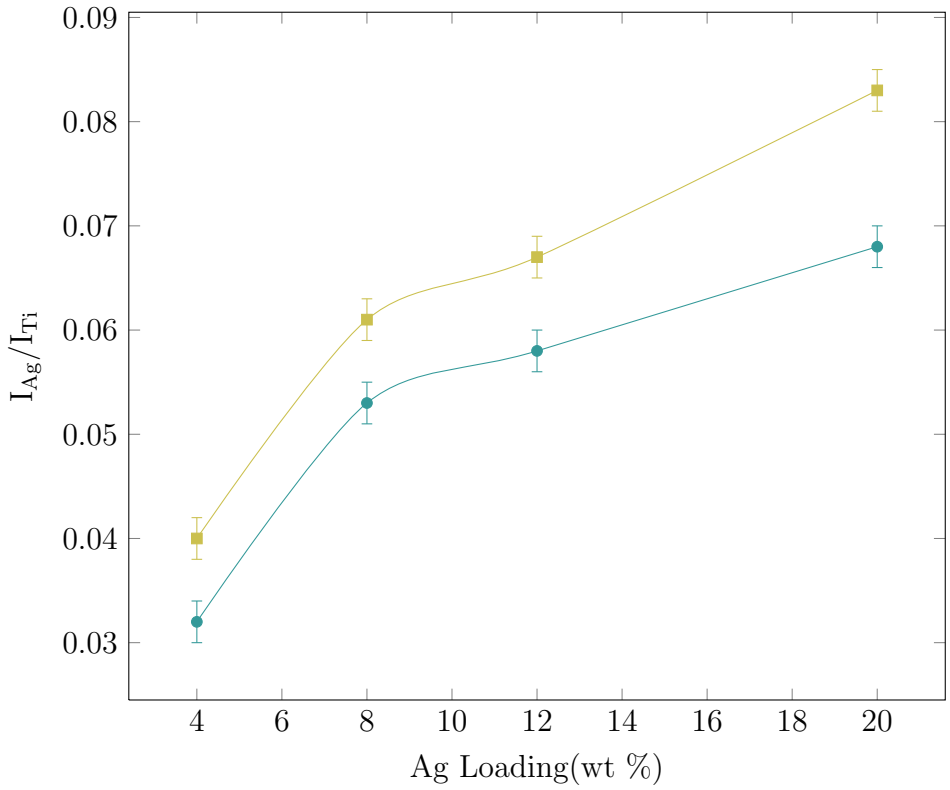

Figure 4.10: Case 2 - Estimation of I_{Ag}/I_{TiO_2} using thickness calculated from chemisorption dimensions.

The I_{Ag}/I_{TiO_2} theoretical values derived using case 2 was lower than the experimental values by a factor of 4 -7, increasing from 4 - 20 wt% loading. The surface coverage from case 1 was calculated based on the chemisorption diameters to calculate the thickness and in case 2, the chemisorption diameters were used directly in using the relationship $2R_{Ag} = 3t_{Ag}$ to calculate the thickness.

Table 4.8: I_{Ag}/I_{TiO_2} Experimental versus Theoretical - Case 2

Ag Loading	I_{Ag}/I_{TiO_2}		
	Experimental	Theoretical	
wt%		Spherical	Cubic
4	0.14	0.032	0.040
8	0.28	0.053	0.061
12	0.35	0.058	0.067
20	0.48	0.068	0.083

This method of determining theoretical values for I_{Ag}/I_{TiO_2} does not produce a correlation with experimental values. Since the surface coverage values were estimated using chemisorption values, an improvement in this method would be to find an independent source of surface coverage estimation.

Case 3: Estimate particle size values from XPS data. Use the values from XPS data for I_{Ag}/I_{TiO_2} in Equation 4.1, 4.2, and the relationship $2R_{Ag} = 3t_{Ag}$, to derive the particle size.

The plot of the average particle size predicted from the experimental XPS intensity ratios Figure 4.11 displayed a linear relationship. This linear relationship was expected in these predictions as a curve would be indicative of particle growth. Particle growth is not accounted for by the model because XPS see mono distribution, thus when are large particles the accuracy of particle size determination by XPS decreases. This estimation is unrealistic as 0.7 Å is in the subatomic region. The atomic radius of silver is 1.75 Å thus estimating a particle diameter to be less than the atomic radius is incorrect.

The method outlined in Kuipers et al. describes a homogenous mixture of silver particles with the titania support, not the silver dispersed on the surface of the titania. This accounts for the low calculated crystallite size predictions. These results showed that Ag is not homogeneously dispersed throughout the support.

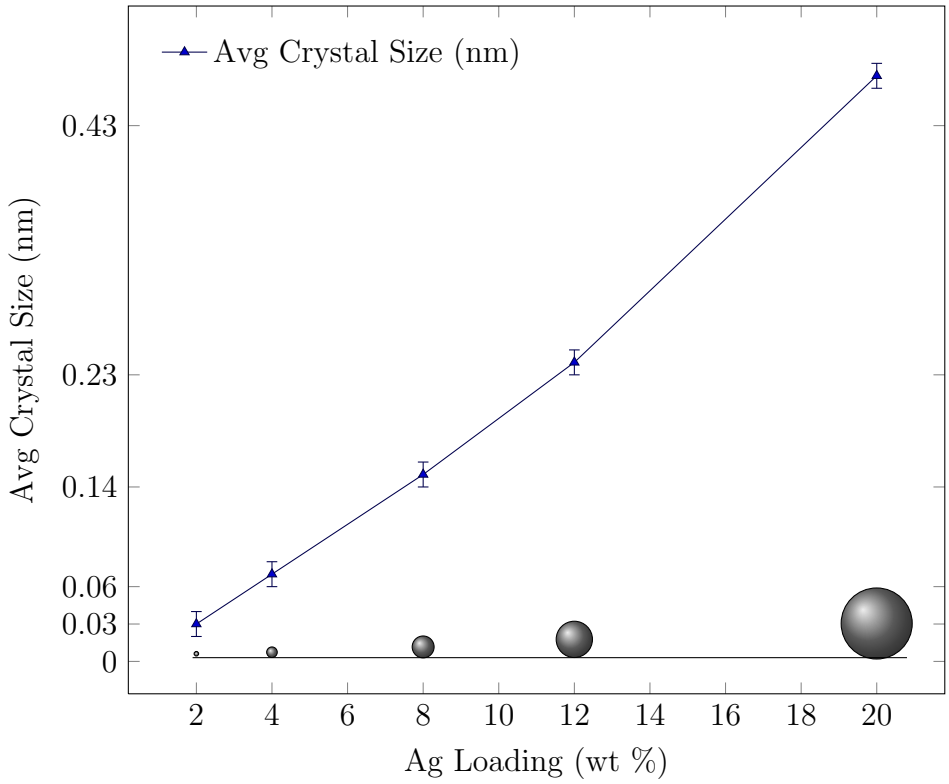

Figure 4.11: Case 3- Particle size estimation using XPS experimental data

Table 4.9: Particle Size Dimensions - Oxygen Chemisorption versus XPS

Ag Loading	Particle Size (nm)	
wt %	Oxygen Chemisorption	XPS
4	3.4	0.07
8	4.1	0.15
12	5.3	0.24
20	6.9	0.47

4.2 Evaluation of Particle Size using XPS Experimental Data

The intensity of the Ag photoelectron peak from first principles is described by:

$$I_{Ag} = I_0 n \sigma_{Ag} \lambda_{Ag}(\epsilon) D(\epsilon) \int_0^t e^{-t/\lambda} \, \mathrm{d}t \tag{4.3}$$

where I_0 is the X-ray flux, n is the density of Ag atoms, σ is the photoelectron cross-section of Ag, $f(\epsilon)$ is a function of energy, $\lambda(\epsilon)$ is the mean free path of energy of Ag (ϵ), $D(\epsilon)$ the fraction of electrons detected by the analyzer. The Equation 4.3 will be further simplified to:

$$I_{Ag} = B_0 \sigma_{Ag} \lambda_{Ag}(\epsilon) N_{Ag} \underbrace{\int_0^t e^{-t/\lambda} \, \mathrm{d}t}_{growth\ term} \tag{4.4}$$

where B_0 is a constant which includes the X-ray flux, transmission efficiency, accepted angles, analyzer efficiency, all morphological and instrumental parameters which can be reasonably assumed constant given uniform instrumental collection parameters, such as pass energy and detection range during the sample analysis. N_{Ag} is the number of atoms/g, $\int_0^t e^{-t/\lambda}$ describes the cumulative probability with which elctrons are ejected form the sample at depth t. It also describes the growth of the particles above atomic dispersion which was assumed equal to 1, when particle growth is absent.

Similarly, $I_{\mathrm{TiO_2}}$ photoelectron peak will be described by:

$$I_{\mathrm{TiO_2}} = B_0 \sigma_{\mathrm{TiO_2}} \lambda_{\mathrm{TiO_2}} N_{\mathrm{TiO_2}} \int_0^\infty e^{-t/\lambda} \, \mathrm{d}t \tag{4.5}$$

So,

$$\frac{I_{Ag}}{I_{\mathrm{TiO_2}}} = \frac{B_0 \sigma_{Ag} \lambda_{Ag} N_{Ag} \int_0^t e^{-t/\lambda} \, \mathrm{d}t}{B_0 \sigma_{\mathrm{TiO_2}} \lambda_{\mathrm{TiO_2}} N_{\mathrm{TiO_2}} \int_0^{t=\infty} e^{-t/\lambda} \, \mathrm{d}t} \tag{4.6}$$

Apply Equation 4.6 to the Ag/TiO_2 system,

$$\frac{I_{Ag}}{I_{\mathrm{TiO}_2}} = \frac{B_0\sigma_{Ag}\lambda_{Ag}N_{Ag}\int_0^t e^{-t/\lambda}\,\mathrm{d}t}{B_0\sigma_{\mathrm{TiO}_2}\lambda_{\mathrm{TiO}_2}N_{\mathrm{TiO}_2}\int_0^\infty e^{-t/\lambda}\,\mathrm{d}t} \tag{4.7}$$

It is theorized that at low loading all atoms are accessible on the surface of the TiO_2. Thus at the linear section of the graph I_{Ag}/I_{Ti} vs Ag Loading (Figure 4.13) atoms were assumed to be on the surface of the support. Also, the XPS signal arising from the support will be constant as there was no diminution in the XPS signal of TiO_2 from the increased loading, between 0–20 wt% Ag on the surface of the TiO_2.

$$\begin{aligned}\frac{I_{Ag}}{I_{\mathrm{TiO}_2}} &= \frac{\cancel{B_0}\sigma_{Ag}\lambda_{Ag}N_{Ag}\int_0^{t=0} \cancel{e^{-t/\lambda}}^{\,1}\,\mathrm{d}t}{\underbrace{\cancel{B_0}\sigma_{\mathrm{TiO}_2}\lambda_{\mathrm{TiO}_2}N_{\mathrm{TiO}_2}\int_0^\infty e^{-t/\lambda}\,\mathrm{d}t}_{constant}} \\ &= \frac{\sigma_{Ag}\lambda_{Ag}N_{Ag}}{\sigma_{\mathrm{TiO}_2}\lambda_{\mathrm{TiO}_2}N_{\mathrm{TiO}_2}}\end{aligned} \tag{4.8}$$

$$N_{\mathrm{TiO}_2} = N_0\mathrm{TiO}_2\int_0^{t=10} e^{-t/\lambda}\,\mathrm{d}t \tag{4.9}$$

N_{TiO_2} was calculated at $t = \infty$. In XPS infinite depth $t = \infty$ was assumed to be $\approx t = 1000$, at this value no photoelectron should be detected according to the governing equations. An atomic layer was modeled to comprise of the total number of TiO_2 atoms on a square matrix of area 150 m^2, see schematic representation and photoelectron intensity probability function in Figure 4.12. Figure 4.12 (a) shows a simplified representation of the layers of atoms of TiO_2 and the graph in Figure 4.12 (b) shows the probability that an electron will escape as a function of depth corresponding to λ.

$N_0\mathrm{TiO}_2 = 1 \times 10^{21}$

λ= 18.5 Å

Number of Layers = 1000

TiO_2 (100) Interatomic spacing = 3.79 Å

$N_{TiO_2} = 5.40 \times 10^{21}$

The resulting theoretical I_{Ag}/I_{TiO_2} is listed in Table 4.10.

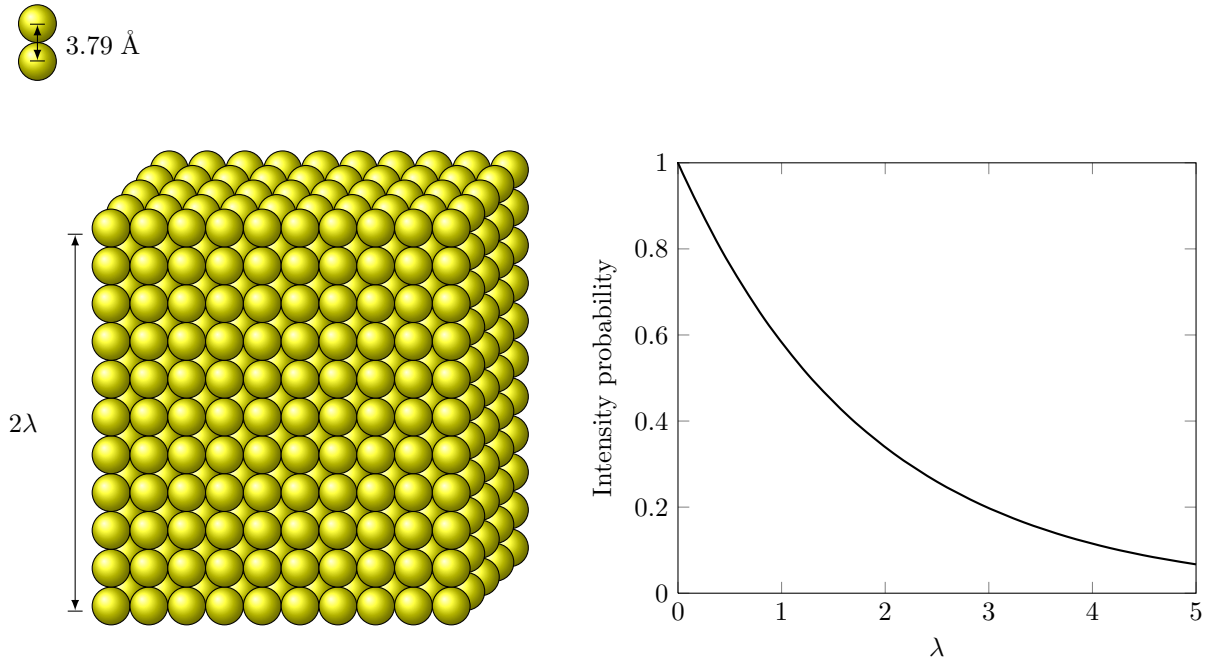

(a) Layers of representative atoms **(b)** Photoelectron intensity probability function

Figure 4.12: Schematic of the TiO_2 support

In Figure 4.13 the theoretical and experimental I_{Ag}/I_{TiO_2} are plotted with respect to wt% loading of Ag on TiO_2. The solid lines with the diamond and oplus markers represent the Ag/TiO_2 ratio observed and the theoretical calculated values of the Ag/TiO_2 ratio respectively. In general all the theoretical calculated values are lower than the experimental value; this suggests there is an error arising from one of the physical parameters. The theoretical calculated values are the best case scenario and such the experimental line should fall below the theoretical line. The two most likely sources of error lie in the calculation of the mean free path and the estimation of N_0 in Equation 4.9. The mean free path was calculated from the semi-empirical formula developed by Penn [73]. The Penn formula assumes that the atoms and molecules are homogeneously distribute throughout the material and that

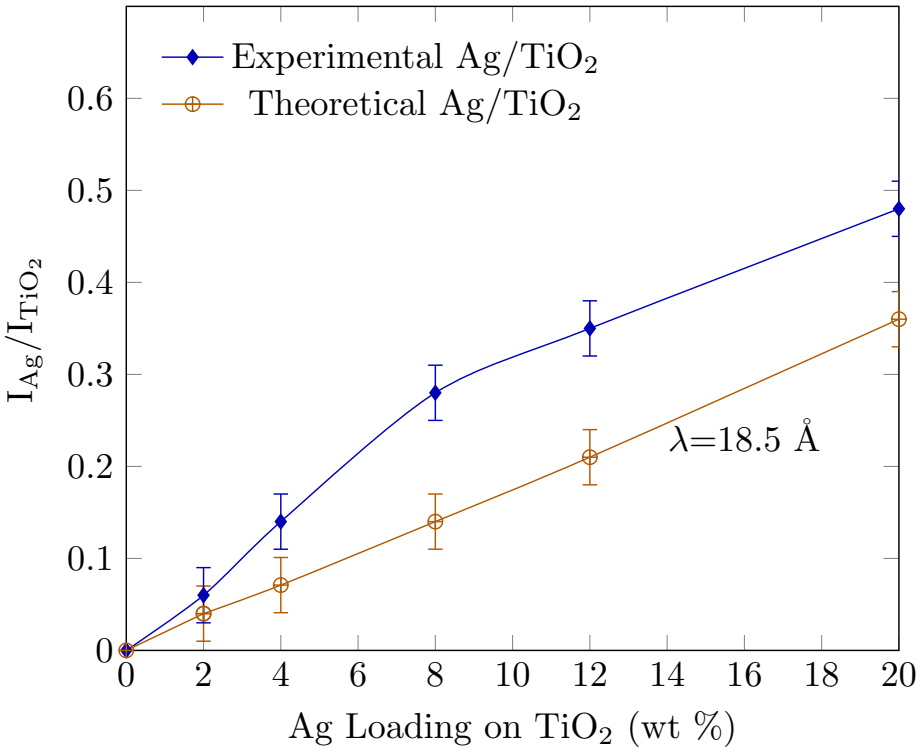

Figure 4.13: Ag/Ti ratio as a function of weight loading of Ag

Table 4.10: I_{Ag}/I_{TiO_2} -Experimental versus Theoretical

Ag	I_{Ag}/I_{TiO2}	
Loading (wt %)	Experimental	Theoretical
2	0.06	0.04
4	0.14	0.07
8	0.28	0.14
12	0.35	0.21
20	0.48	0.36

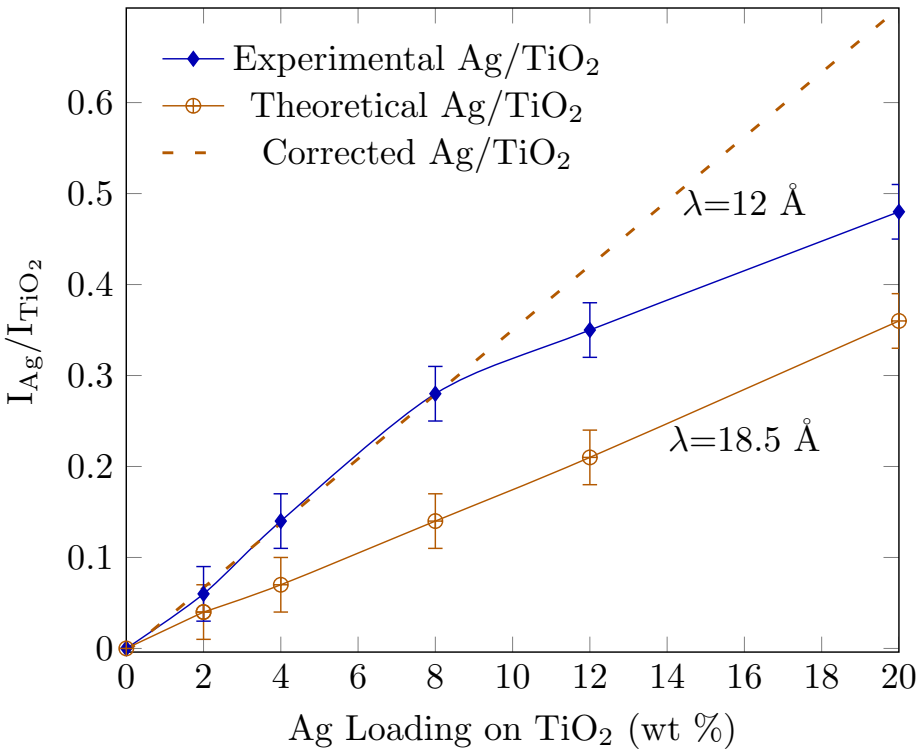

Figure 4.14: Ag/Ti ratio as a function of weight loading of Ag

the material is 100% dense. While this is not the case, the value will be used as a starting approximation. The value of N_0 based on the interatomic spacing of the TiO_2 of the (100) plane.

A correction was made by assuming that at Ag loading less or equal to 4 wt% every a signal from TiO_2 molecule is sampled. Thus, the ultimate signal will be acquired and experimental values scan only be less than or equal to this value. The dotted line in Figure 4.14 shows the corrected theoretical gradient. Using this gradient, a value of 12.0 Å was derived for the mean free path. The mean free path is highly surface dependent, thus considering the amorphous nature, surface roughness, and the porosity of the adsorbent, the derived mean free path can be used as a working basis approximation.

4.3 Particle Growth Estimation

Predicted XPS Intensity Ratio due to Particle Growth

If an assumption is made that the Ag atoms are all uniformly dispersed on the support, then an estimation can be made to locate the point beyond which the Ag particles begin to increase in size based on a comparison of the experimental I_{Ag}/I_{TiO_2} and the calculated I_{Ag}/I_{TiO_2} assuming 100% accessibility of Ag atoms.

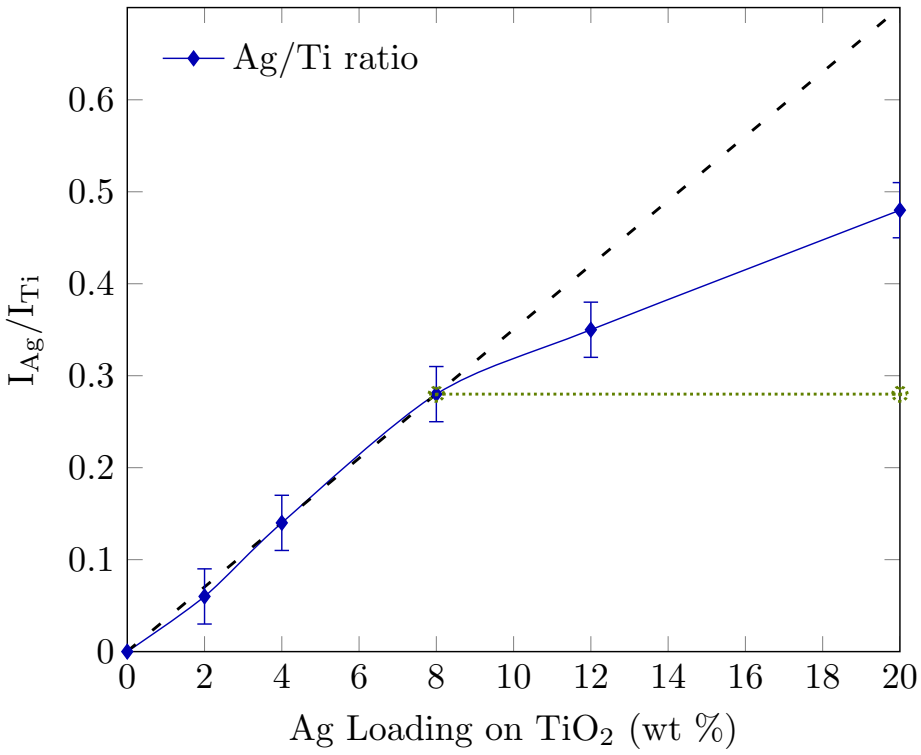

Figure 4.15: Ag/Ti ratio as a function of weight loading of Ag

Table 4.11: Particle Growth - after 8 wt% Loading

Ag Loading (wt%)	I_{Ag}/I_{TiO_2} Experimental	Predicted I_{Ag}/I_{TiO_2} due to Particle Growth
8	0.28	—
12	0.35	0.39 ± 0.04
20	0.48	0.56 ± 0.07

The data displayed in Figure 4.15 suggests that all the Ag atoms are accessible up to 8 wt% loading after which the crystallites growth occurs. This is signified by the departure from the linear behavior demonstrated from 0 wt% up to 8 wt%. Another linear trend is displayed from 8 wt% to 20 wt% which indicates that the particles form crystallites that are uniform in size and increase in occurrence with increased loading up to 20 wt%. The I_{Ag}/I_{TiO_2} experimental values form 0 – 8 wt% loadings lie on the on a line which typically indicates uniform dispersion. Since non-linear behavior starts after 8 wt% loading, it was assumed that nucleation occurred beyond this point. Table 4.11 lists the predicted I_{Ag}/I_{TiO_2} values due to particle growth. The predicted values at 12 wt% fell at the lower end of the uncertainty range while at the 20 wt% loading the predicted value was just outside the uncertainty range.

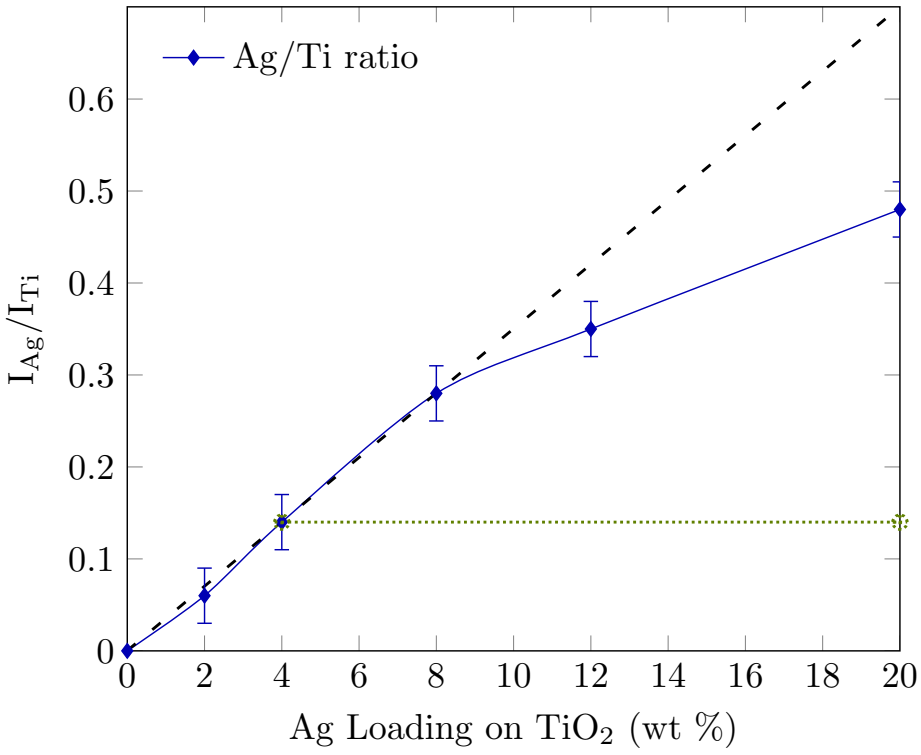

Figure 4.16: Ag/Ti ratio as a function of weight loading of Ag

Table 4.12 lists the predicted I_{Ag}/I_{TiO_2} values when particle growth is assumed to after 4 wt% loading. These values are well within the uncertainty range. The results listed in

Tables 4.11 and 4.12 indicates that arguably the Ag particle growth could be somewhere between 4 wt% than 8 wt%. Also, since the sulfur heterocyclic adsorption selectively has the greatest capacity at about the 4 wt% loading a more confident assertion is that particle growth begins at this point.

Table 4.12: Particle Growth- after 4 wt% Loading

Ag Loading (wt%)	I_{Ag}/I_{TiO_2} Experimental	Predicted I_{Ag}/I_{TiO_2} due to Particle Growth
4	0.14	—
8	0.28	0.24 ± 0.03
12	0.35	0.33 ± 0.04
20	0.48	0.46 ± 0.05

Predicted Particle Size

The dimension change of the crystallites were found by equating the particle growth term as seen in Equation 4.4 to the I_{Ag}/I_{TiO_2} experimental values. Particle growth was assumed to begin after 4 wt% loading.

Table 4.13: XPS Ag Crystallite Growth Estimation

Ag Loading (wt%)	Crystallite Size (nm)	No. of atoms on Edge	Total No. of Atoms
8	0.71	2	8
12	0.84	3	27
20	1.11	4	64

The final dimensions can be calculated by accounting for the initial atomic size plus the growth dimension. One Ag atomic radius is equivalent to approximately 0.35 nm. If a crystallite at the 8 wt% loading contains 2 atoms on an edge of a cube then the total number of atoms contained would be 8 atoms. The subsequent size at 8 – 20 wt% loadings are listed in Table 4.13.

The diagrams in Figure 4.17 are a representation of the model surface of the adsorbent at the various weight loading that have the characteristics that are consistent with the

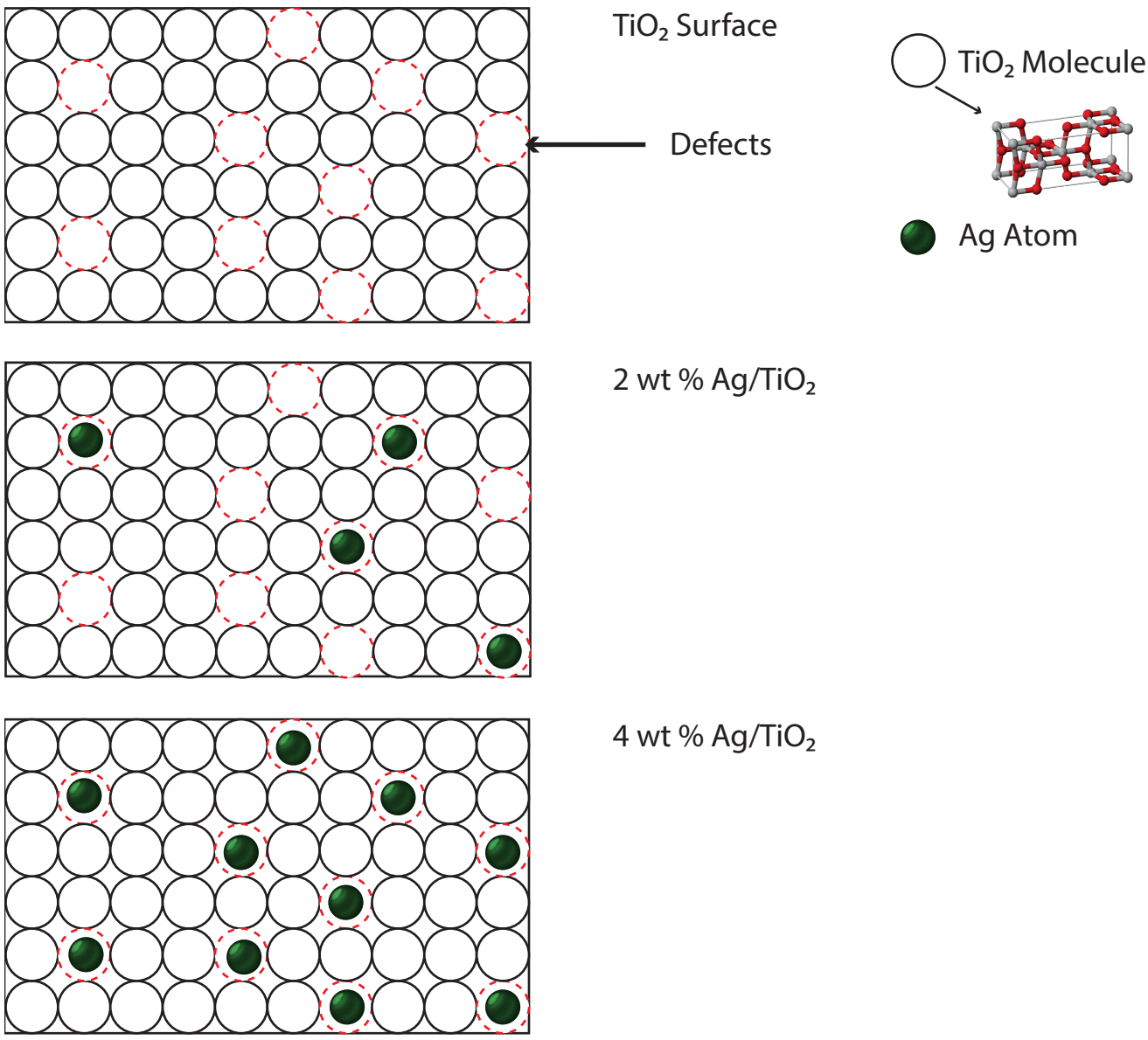

Figure 4.17: Schematic representation of the most probable morphological configuration of Ag/TiO_2. 0 – 4 wt% Ag loading.

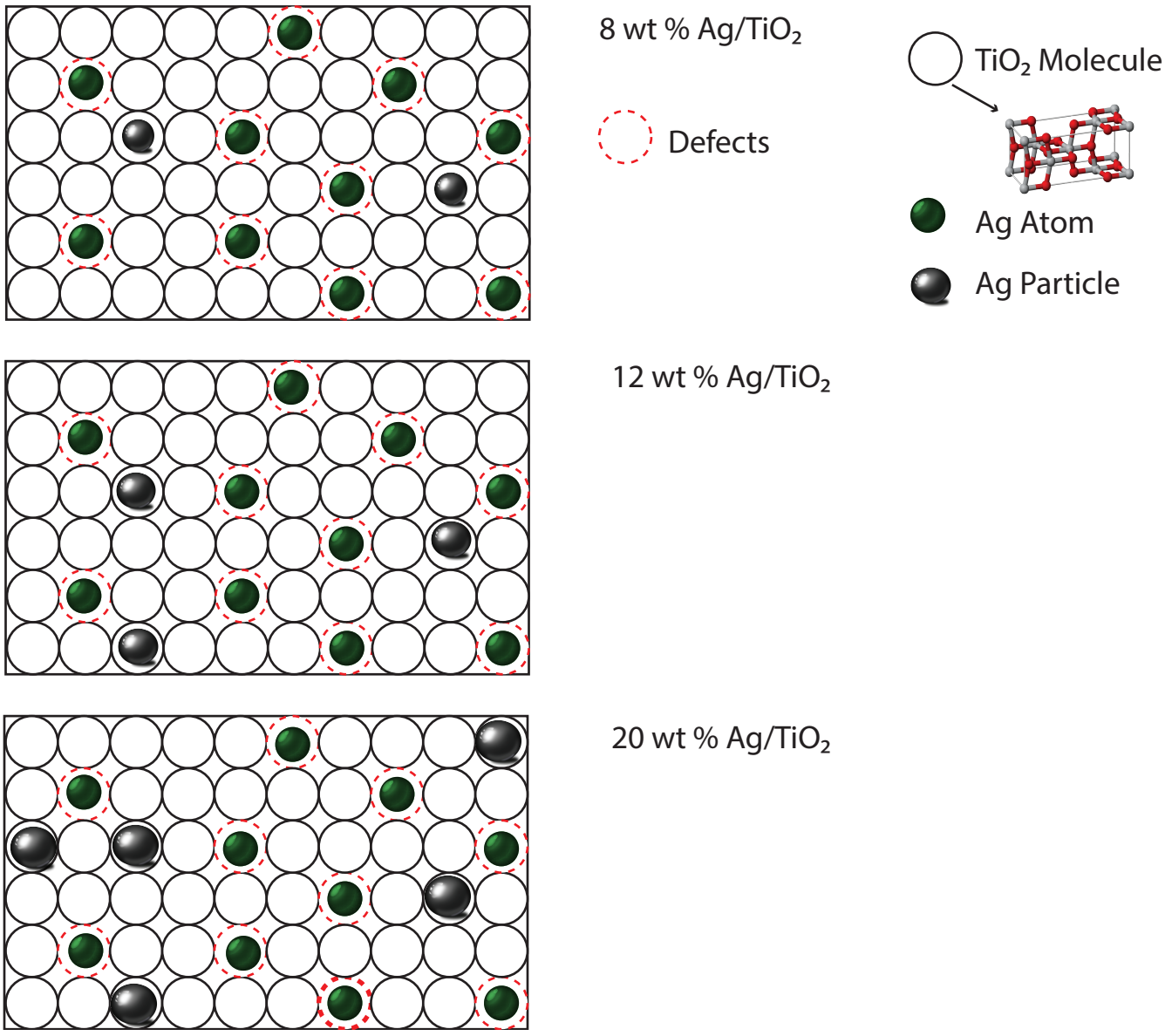

Figure 4.18: Schematic representation of the most probable morphological configuration of $Ag/TiO_2$8– 20 wt% Ag loading.

experimental results of the XPS. At the 2 and 4 wt% loading it is believed that the atoms are of the same size but increase in occurrence as the weight loading of silver increase. This theory is due to the fact that 0, 2, and 4 wt% loadings line on the same line segment. At $\leq$ 4 wt% loading the Ag crystallites occupy surface defects on the titanium surface and all the atoms are settled on the surface. When the crystallites settle into the high energy sites they will have a lower free energy and thus be more stable. It is theorized that all the surface defected high energy sites are populated at about the 4 wt% loading and thus further increase in loading results in particle growth.

At the 8 wt% loading the silver coverage is about 0.28 ML (refer to Figure 4.19), hence it can be assumed that silver atoms can still occupy the available surface on the titanium dioxide. However, there are no more defects available on the titanium sites that can hold the individual silver atoms strongly. At the 8, 12, and 20 wt% loadings the crystal grow progressively bigger as revealed by the particle size estimations.

Assuming Ag was 100 % dispersed, the monolayer thickness was calculated. Figure 4.19 shows the mole fraction of Ag detected and the mole fraction of Ag deposited with respect to monolayer thickness and percent weight loading. The figure indicated the effectiveness of the XPS at detected the actual number of moles of Ag deposited.

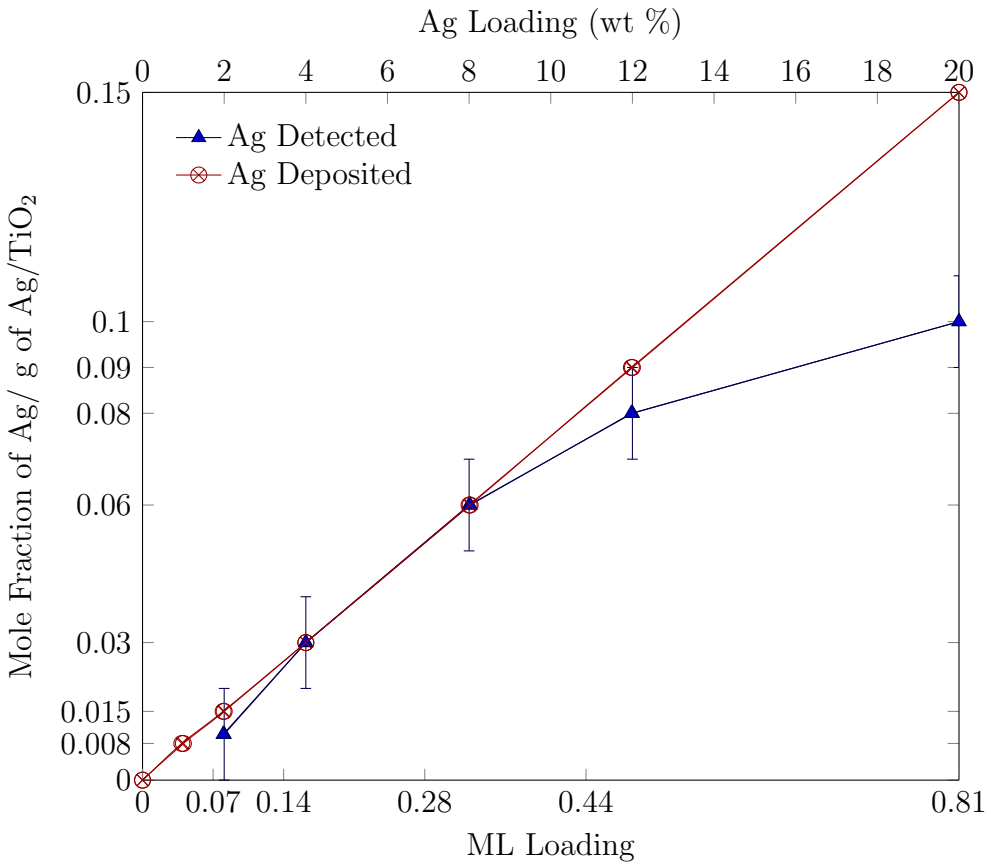

Figure 4.19: Monolayer detected versus moles deposited of Ag

4.4 EPR Analysis

Previous work using EPR, revealed that only $\sim$ 0.1 % of the total Ag was present as Ag^{2+} on the 4 wt% Ag/TiO_2 sorbent [21]. The shift towards lower B.E in the XPS spectra of the Ag 3d peaks from the 4 wt% to the 20 wt% loading of Ag/TiO_2 (see figure 4.2) prompted complementary investigation by EPR. Specifically, the EPR signal for nanoparticles of metallic Ag that may be evident at about 3250G and 3350 G [99].

The 2, 4, 8, 20 wt% loadings of Ag/TiO_2 was analyzed in an attempt to resolve the EPR line for Ag^0 and Ag^{2+} species. The results were inconclusive with regards to the presence of Ag^0 line. EPR spectral lines at about 3000G and 3600 G were except due to Ag^0 [100–102]. The Ag signal could not be resolved from the samples with sites found in literature [100–102]. The EPR signal for the Ag^{2+} species is most easily identified in the 4 wt% loading. This result correlates with other findings [1] which leads to the conclusion that 4 wt% Ag/TiO_2 has special properties that enhances its capacity for sulfur removal. In the 8 and 20 wt% loadings the Ag line maybe present in the 3250 - 3400 G region but it is unobservable due to overlapping with the Ti EPR line- the EPR line has been broaden line in this region. This broadening is influenced by the presence of NO bound to the bulk titania [103, 104]. Resolution of the Ag signal in the Ag/titania sorbent is difficult because the EPR signal due to trapped nitrate and Ag/titania sorbent are identical. Previous work demonstrated that there is a small concentration of NO bound to bulk TiO_2 in the Ag/TiO_2 sorbent [104]. The EPR measurement temperature was varied in an effort to distinguish the spectral contributions. Spectra was taken at 77 K and 298 K.

Preliminary XAFS measurement [89] indicated the presence of a metallic contribution. Why does XAFS indicate the presence of metallic silver when EPR does not? The answer lies the intrinsic manner in which the techniques evaluates the presence of metallic Ag. Maybe XAFS is more sensitive to the presence of metallic Ag than EPR.

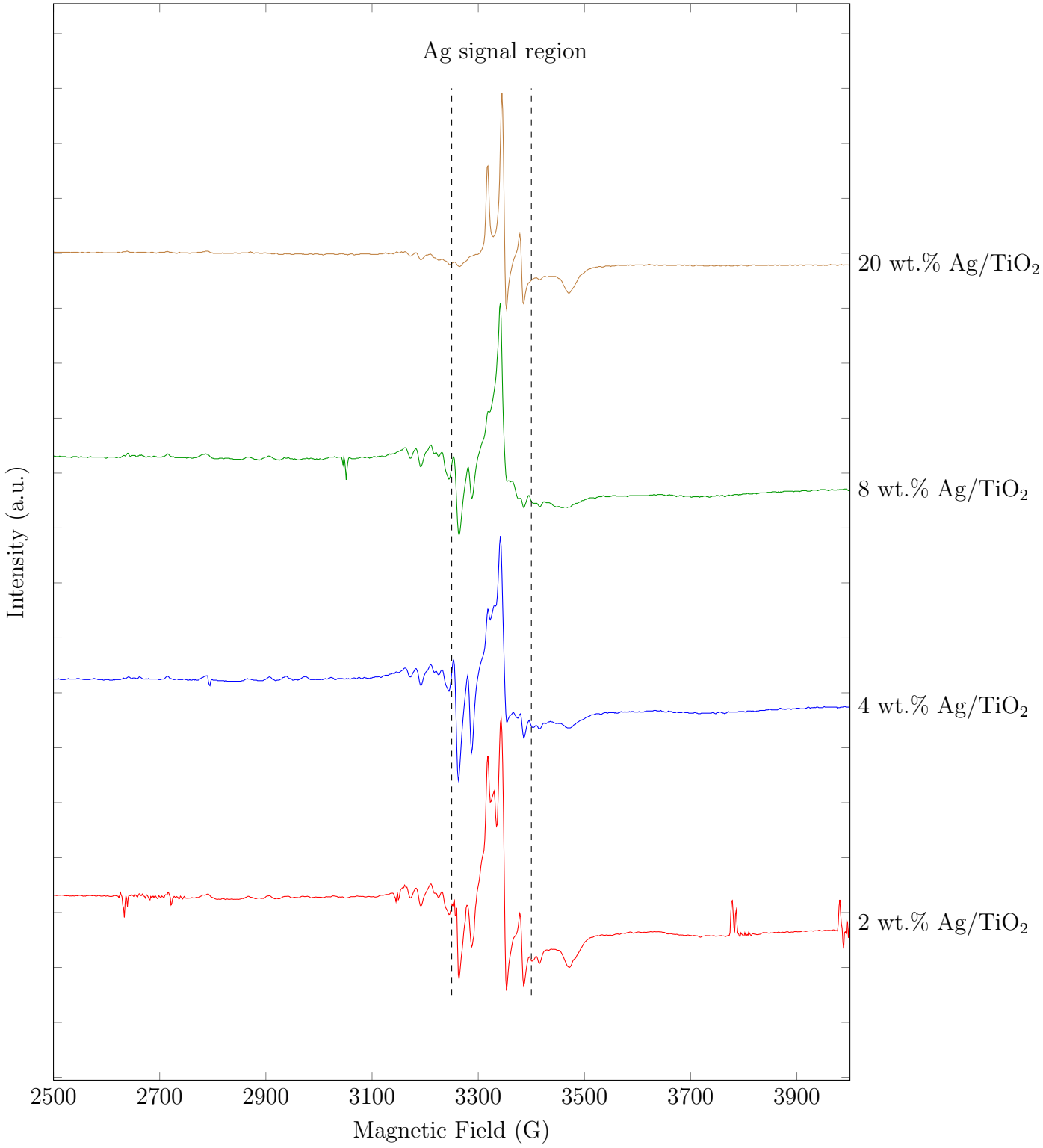

Figure 4.20: EPR spectra of the Ag/TiO_2 at 77 K

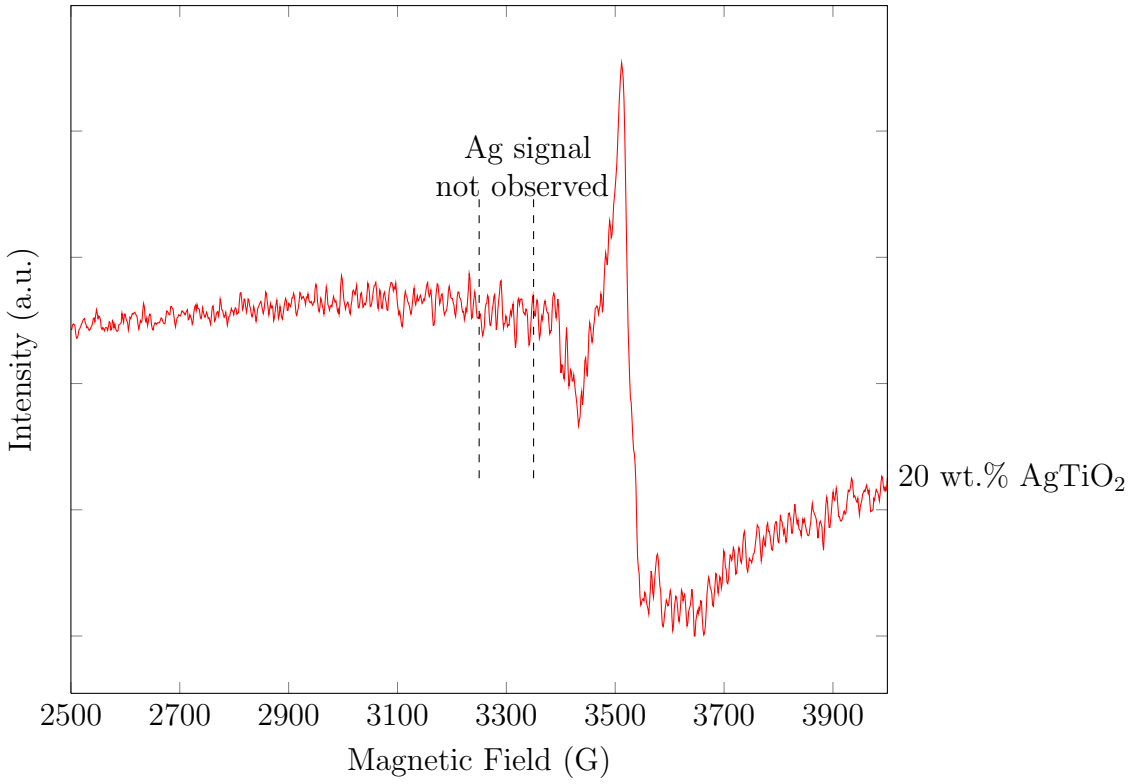

Figure 4.21: EPR spectra of the Ag/TiO_2 at 298 K

Chapter 5

Conclusion

Fundamental studies aimed at acquiring a greater understanding of desulfurization materials were performed. The salient findings of this study are stated below.

The surface of the titania support from an XPS perspective is not appreciably shadowed by the Ag particles up to 20 wt% loading. The maximum area occupied by silver particle is less than approximately 6% of the total surface area of the titania assuming that the crystallites are evenly spaced of spherical, hemispherical or cubic geometries. Homogenous and mono dispersal of Ag on the support would result in coverage up to 0.81 ML at 20 wt%.

A functional relationship exists between the dispersed phase, the size of the silver particle and the observed XPS intensity. Ag/TiO_2 adsorbents display mono dispersion up to the 4 wt% loading. This corresponds to hypothesis that the silver atoms populate defects on the titanium support up to this specific weight loading. This 4 wt% loading is the critical loading baseline after which the atoms begin to grow into bigger crystallites.

The characteristic property of sulfur selectivity is a combination of the interaction of the silver oxide, the population of titania defects and the size of the silver crystallites. XPS result indicated the presence of Ag in its oxide form. The XPS oxygen peak due assigned to Ag^{1+} was the most dominant suggesting that Ag_2O was in the majority.XPS results also indicated that the activity of Ag/TiO_2 is most likely optimal not only for a specific size but also when the defects on the titania support are populated.

Oxygen chemisorption should not be used as the sole means of determining the particle size of Ag particles; the inherent assumptions may lead to inaccuracies in estimation. The combination of XPS and chemisorption measurements are a more accurate indication of the actual crystallite size. Oxygen chemisorption over-estimated the particle size for Ag particles

in the Ag/TiO_2 system studied. XPS provided a more accurate representation of particle size. The 2-10 Å particle size range estimated from XPS is supported by the fact that the Ag particle size could not be determined from XRD measurements, thus suggesting than the particle sizes are less than 5 nm.

Chapter 6

Future Work

The ultimate goal of this project is to gain crucial information about the surface properties responsible for the Ag/TiO_2 adsorbent's capacity to desulfurize liquid phase high sulfur logistic fuels. This knowledge is necessary to enhance performance and develop new sorbents. The following are suggestions of future studies that can be done to contribute to a complete understanding of the sorbent.

Isolation of Ag^0 species by EPR. Implement a stepwise approach by trying a different support to isolate and identify the Ag species. The support used should not be paramagnetically active. Investigate the existence of Ag^0 at 473 K signal that was reported in Wang and Weh [102], which should be absent at room temperature due to sample exposure to air.

Evaluation of TiO_2 native oxygen uptake. Account for oxygen uptake using oxygen chemisorption on the native or nitrated TiO_2 surface and re-evaluate crystallite size approximations.

Temperature programmed analysis. Exploration of the desorption kinetics, surface reaction mechanisms, nature of the surface intermediates and surface acidity. Investigate the acidity of Ag/TiO_2 adsorbents by TPD/TPRS using probe molecules such as ammonia and pyridine that provide selective interaction with the surface sites. Ammonia can be used to indicate strong and weak Brønsted and Lewis sites while pyridine can be to show strong and weak Brønsted and strong and weak Lewis sites, thereby enabling the discernment of the weak Brønsted site [105–108].

Temperature programmed XPS of the chemisorption assumptions and conditions. This would provide a better understanding of oxygen chemisorption when used with silver particles.

Investigation of the adsorption process and assessment of the removal pathway. The introduction of selective refractory heterocyclic species, such as thiophene and benzothiophene and in TPD/TPRS will enable the assessment of specificity of various heterocyclic compounds. Since it is known that the surface of the Ag strongly influences the sorbent's affinity for the refractory heterocyclic compounds. It is reported that Ag forms step edges at which the sulfur binds on Ag surfaces [109, 110] thus, it is likely that it is the structure of the edges that facilitate the 'lock' for these big refractory compounds.

Additional XPS characterization. Perform XPS investigation on the adsorbent system Ag/TiO_2 using a more sensitive system than the non-monochromated LHS-10. XPS has become even more powerful with new technological advancements: higher counting rates, more sensitive detection limits, narrower FWHM, greater signal-to noise ratios. These new advances have enabled acquisition of more fundamental surface chemical information. Thus, more information can be extracted by the technique since limitations encountered were due to the current XPS system and the technique.

Examination of the Ag Auger energy levels to distinguish the factors such as static relaxation term influencing chemical shifts in the Ag/TiO_2 adsorbent. Comparison of the Auger energy shifts and binding energy shift can lead to the identification of the Ag chemical environment.

Also, XPS can be used as a complementary technique to TPD/TPRS study surface acidity of Ag/TiO_2. This technique has been used to study the adsorption of probe molecules such as: benzene, pyridine, and pyrrole in literature [95, 111, 112]. Specifically, perform alkali treatment to modify acid-base properties to investigate surface acidity.

Complementary crystallite size determination. Use scanning probe microscopy (SPM) to get an independent determination of crystallite size. SPM uses a fine probe to image surfaces at the nanometer scale. This technique is not restricted by the wavelength of light or electrons and can resolve atoms and true 3-D maps of surfaces.

Sintering study. Perform a sintering study to show the nucleation growth of the mobile silver particles. Anneal the Ag/TiO_2 samples at various temperatures for example 400, 450, 500°C, etc. Analyse the samples using XPS and plot the I_{Ag}/I_{TiO_2} as a function of the annealing temperature.

Bibliography

[1] S. Nair and B. J. Tatarchuk, "Supported Silver Adsorbents for Selective Removal of Sulfur Species from Hydrocarbon Fuels," *Fuel*, vol. 89, no. 11, pp. 3218–3225, 2010.

[2] U. E. P. A. (EPA), "Fuel Sulfur Standards," 01 2009. Code of Federal Regulations (CFR) citations: 40 CFR Part 80 Subpart H.

[3] C. A. I. for Asian Cities (CAI-Asia), "Current and Proposed Sulfur levels in Diesel in Asia, EU and USA.," 2009.

[4] U.S. Energy Information Administration, "Light-Duty Diesel Vehicles: Efficiency and Emissions Attributes and Market Issues," tech. rep., U.S. Energy Information Administration, 2009. SR/OIAF(2009)02.

[5] "Part 80 - Regulation of Fuels and Fuel Additives," *Federal Register*, vol. 65, pp. 6822–6870, February 2000.

[6] X. Ma, M. Sprague, and C. Song, "Deep Desulfurization of Gasoline by Selective Adsorption over Nickel-Based Adsorbent for Fuel Cell Applications," *Industrial & Engineering Chemistry Research*, vol. 44, no. 15, pp. 5768–5775, 2005.

[7] C. Song, "An Overview of New Approaches to Deep Desulfurization for Ultra-Clean Gasoline, Diesel Fuel and Jet Fuel," *Catalysis Today*, vol. 86, no. 1-4, pp. 211 – 263, 2003. Effects of Support in Hydrotreating Catalysis for Ultra-clean Fuels.

[8] S. Velu, X. Ma, and C. Song, "Selective Adsorption for Removing Sulfur from Jet Fuel over Zeolite-Based Adsorbents," *Industrial & Engineering Chemistry Research*, vol. 42, no. 21, pp. 5293–5304, 2003.

[9] X. Ma, S. Velu, J. H. Kim, and C. Song, "Deep Desulfurization of Gasoline by Selective Adsorption over Solid Adsorbents and Impact of Analytical Methods on ppm-level Sulfur Quantification for Fuel Cell Applications," *Applied Catalysis B: Environmental*, vol. 56, no. 1-2, pp. 137 – 147, 2005.

[10] A. J. Hernandez-Maldonaldo and R. Yang, "Desulfurization of Transportation Fuels by Adsorption," *Catalysis Reviews*, vol. 46, no. 2, pp. 111–150, 2004.

[11] E. Ito and J. R. van Veen, "On novel Processes for Removing Sulphur from Refinery Streams," *Catalysis Today*, vol. 116, no. 4, pp. 446 – 460, 2006.

[12] P. T. Vasudevana and J. L. G. Fierro, "A Review of Deep Hydrodesulfurization Catalysis," *Catalysis Reviews: Science and Engineering*, vol. 38, pp. 161–188, May 1996.

[13] X. Ma, K. Sakanishi, and I. Mochida, "Hydrodesulfurization Reactivities of Various Sulfur Compounds in Vacuum Gas Oil," *Industrial & Engineering Chemistry Research*, vol. 35, no. 8, pp. 2487–2494, 1996.

[14] S. Haji and C. Erkey, "Removal of Dibenzothiophene from Model Diesel by Adsorption on Carbon Aerogels for Fuel Cell Applications," *Industrial & Engineering Chemistry Research*, vol. 42, no. 26, pp. 6933–6937, 2003.

[15] A. J. Hernndez-Maldonado and R. T. Yang, "Desulfurization of Liquid Fuels by Adsorption via Complexation with Cu(I)Y and AgY Zeolites," *Industrial & Engineering Chemistry Research*, vol. 42, no. 1, pp. 123–129, 2003.

[16] R. V. Siriwardane and J. A. Poston, "Characterization of Copper Oxides, Iron Oxides, and Zinc Copper Ferrite Desulfurization Sorbents by X-ray Photoelectron Spectroscopy and Scanning Electron Microscopy," *Applied Surface Science*, vol. 68, no. 1, pp. 65 – 80, 1993.

[17] J. H. Kim, X. Ma, A. Zhou, and C. Song, "Ultra-deep Desulfurization and Denitrogenation of Diesel Fuel by Selective Adsorption over Three Different Adsorbents: A Study on Adsorptive Selectivity and Mechanism," *Catalysis Today*, vol. 111, no. 1-2, pp. 74 – 83, 2006.

[18] S. Velu, X. Ma, C. Song, M. Namazian, S. Sethuraman, and G. Venkataraman, "Desulfurization of JP-8 Jet Fuel by Selective Adsorption over a Ni-based Adsorbent for Micro Solid Oxide Fuel Cells," *Energy & Fuels*, vol. 19, pp. 1116–1125, 2005.

[19] D. L. King and L. Li, "Removal of Sulfur Components from Low Sulfur Gasoline using Copper Exchanged Zeolite Y at Ambient Temperature," *Catalysis Today*, vol. 116, no. 4, pp. 526 – 529, 2006.

[20] B.Tatarchuk, H. Yang, and S. Nair, "Silver-Based Sorbents," April 2008. US 2008/0283446 A1.

[21] A. Samokhvalov, S. Nair, E. C. Duin, and B. J. Tatarchuk, "Surface Characterization of Ag/Titania Adsorbents," *Applied Surface Science*, vol. 256, no. 11, pp. 3647–3652, 2010.

[22] J. R. Anderson, *Structure of Metallic Catalysts*. Academic Press Inc, 1975.

[23] M. A. Wahab, *Solid State Physics: Structure and Properties of Materials*. Alpha Science International Ltd, 2nd ed., 2005.

[24] C. Brooks and G. Christopher, "Measurement of the State of Metal Dispersion on Supported Nickel Catalysts by Gas Chemisorption," *Journal of Catalysis*, vol. 10, no. 3, pp. 211–223, 1968.

[25] B. G. Linsen, ed., *Physical and Chemical Aspects of Adsorbents and Catalysts : Dedicated to J. H. de Boer on the Occasion of His Retirement from the Technological University, Delft, the Netherlands*. Academic Press, 1970.

[26] T. E. Whyte, "Metal Particle Size Determination of Supported Metal Catalysts," *Catalysis Reviews*, vol. 8, no. 1, pp. 117–134, 1974.

[27] D. G. Mustard and C. H. Bartholomew, "Determination of Metal Crystallite Size and Morphology in Supported Nickel Catalysts," *Journal of Catalysis*, vol. 67, no. 1, pp. 186–206, 1981.

[28] D. E. Strohmayer, G. L. Geoffroy, and M. A. Vannice, "Measurement of Silver Surface area by the H_2 Titration of Chemisorbed Oxygen," *Applied Catalysisreporte*, vol. 7, no. 2, pp. 189–198, 1983.

[29] S. Seyedmonir, D. E. Strohmayer, G. L. Geoffroy, M. Vannice, H. W. Young, and J. W. Linowski, "Characterization of Supported Silver Catalysts: I. Adsorption of O_2, H_2, N_2O, and the H_2-Titration of Adsorbed Oxygen on Well-Dispersed Ag on TiO_2," *Journal of Catalysis*, vol. 87, no. 2, pp. 424–436, 1984.

[30] B. Kip, F. Duivenvoorden, D. Koningsberger, and R. Prins, "Determination of Metal Particle Size of Highly Dispersed Rh, Ir, and Pt Catalysts by Hydrogen Chemisorption and EXAFS," *Journal of Catalysis*, vol. 105, no. 1, pp. 26–38, 1987.

[31] J. Regalbuto, T. Fleisch, and E. Wolf, "An Integrated Study of $Pt/WO_3/SiO_2$ Catalysts for the NO-CO Reaction: I. Catalyst Characterization by XRD, Chemisorption, and XPS," *Journal of Catalysis*, vol. 107, no. 1, pp. 114–128, 1987.

[32] D. Farin and D. Avnir, "Crystallite Size Effects in Chemisorption on Dispersed Metals," *Journal of Catalysis*, vol. 120, no. 1, pp. 55 – 67, 1989.

[33] R. Wojcieszak, M. J. Genet, P. Eloy, P. Ruiz, and E. M. Gaigneaux, "Determination of the Size of Supported Pd Nanoparticles by X-ray Photoelectron Spectroscopy. Comparison with X-ray Diffraction, Transmission Electron Microscopy, and H_2 Chemisorption Methods," *The Journal of Physical Chemistry C*, vol. 114, no. 39, pp. 16677–16684, 2010.

[34] J. Scholten, J. Konvalinka, and F. Beekman, "Reaction of Nitrous Oxide and Oxygen with Silver Surfaces, and Application to the Determination of Free-Silver Surface Areas of Catalysts," *Journal of Catalysis*, vol. 28, no. 2, pp. 209–220, 1973.

[35] K. M. Kholyavenko, M. Y. Rubanik, and N. Chernukhina, "Determination of the Surface Area of Silver Deposited on a Carrier by Chemisorption," *Kinetika i Kataliza (Kinectics and Catalysis)*, vol. 5, no. 3, pp. 505–512, 1964.

[36] A. W. Czanderna, "The Adsorption of Oxygen on Silver," *The Journal of Physical Chemistry*, vol. 68, no. 10, pp. 2765–2771, 1964.

[37] M. Barteau and R. Madix, *The Surface Reactivity of Silver: Oxidation Reactions in: The Chemical Physics of Solid Surfaces and Heterogeneous Catalysis*, ch. 4, pp. 95–142. Elsevier, 1982.

[38] J. S. Brinen, "Applications of ESCA to Industrial Chemistry," *Journal of Electron Spectroscopy and Related Phenomena*, vol. 5, no. 1, pp. 377–400, 1974.

[39] L. Scharpen, "The Dispersion of Platinum on Silica-Correlation of ESCA and Gas Adsorption Data," *Journal of Electron Spectroscopy and Related Phenomena*, vol. 5, no. 1, pp. 369–376, 1974.

[40] D. Briggs, "ESCA and Metal Crystallite Size/Dispersion in Catalysts," *Journal of Electron Spectroscopy and Related Phenomena*, vol. 9, no. 5, pp. 487–491, 1976.

[41] R. Shalvoy and P. Reucroft, "Quantitative Analysis of ESCA Signal Intensifies from Coprecipitated Nickel on Alumina Catalysts," *Journal of Electron Spectroscopy and Related Phenomena*, vol. 12, no. 3, pp. 351–356, 1977.

[42] M. Houalla and B. Delmon, "Use of XPS to Detect Variations in Dispersion of Impregnated and Ion-exchanged NiO/SiO_2 Systems," *Surface and Interface Analysis*, vol. 3, no. 3, pp. 103–105, 1981.

[43] C. Defosse, M. Houalla, A. Lycourghiotis, and F. Delannay, "Joint Use of X-Ray Photoelectron Spectroscopy and Analytical Electron Microscopy in the Investigation of Cobalt and Nickel Oxide Supported on Na-Doped Alumina," in *New Horizons in Catalysis Proceedings of the 7th International Congress on Catalysis* (T. Seivama and K. Tanabe, eds.), vol. 7, Part A of *Studies in Surface Science and Catalysis*, pp. 108–121, Elsevier, 1981.

[44] Z. Liu, Z. Lin, H. Fan, F. Li, Q. Bao, and S. Zhang, "Dispersion of V_2O_5 Supported on a TiO_2 Surface by X-Ray Photoelectron Spectroscopy," *Applied Physics A: Materials Science & Processing*, vol. 45, pp. 159–164, 1988.

[45] V. D. Castro, C. Furlani, M. Gargano, N. Ravasio, and M. Rossi, "XPS Study of Copper Dispersion in CuO/Al_2O_3 Catalysts," *Journal of Electron Spectroscopy and Related Phenomena*, vol. 52, no. 0, pp. 415–422, 1990.

[46] S. Kaliaguine, "Application of Surface Science Techniques in the Field of Zeolitic Materials," in *Recent Advances and New Horizons in Zeolite Science and Technology* (S. W. H. Chon and S.-E. Park, eds.), vol. 102 of *Studies in Surface Science and Catalysis*, pp. 191–230, Elsevier, 1996.

[47] B. M. Reddy, B. Chowdhury, E. P. Reddy, and A. Fernndez, "An XPS Study of Dispersion and Chemical State of MoO_3 on Al_2O_3-TiO_2 Binary Oxide Support," *Applied Catalysis A: General*, vol. 213, no. 2, pp. 279–288, 2001.

[48] J. Brinen, J. Schmitt, W. Doughman, P. Achorn, L. Siegel, and W. Delgass, "X-ray Photoelectron Spectroscopy Studies of the Rhodium on Charcoal Catalyst: II. Dispersion as a Function of Reduction," *Journal of Catalysis*, vol. 40, no. 3, pp. 295–300, 1975.

[49] S. C. Fung, "Application of XPS to the Determination of the Size of Supported Particles in a Catalyst–Model Development and its Application to Describe the Sintering

Behavior of a Silica-Supported Pt Film," *Journal of Catalysis*, vol. 58, no. 3, pp. 454–469, 1979.

[50] S. Kaliaguine, A. Adnot, and G. Lemay, "A Model for the Quantitative Analysis of ESCA Intensity Ratios for Supported Catalysts with Partial Surface Segregation," *The Journal of Physical Chemistry*, vol. 91, no. 11, pp. 2886–2890, 1986.

[51] S. Davis, "Particle Size Information from Dispersed Phase Photoemission Intensity Ratios," *Journal of Catalysis*, vol. 117, no. 2, pp. 432–446, 1989.

[52] S. Kaliaguine, A. Adnot, G. Lemay, and L. Rodrigo, "On the Quantitative Analysis of XPS Intensity Data for Supported Catalysts with Partial Surface Segregation," *Journal of Catalysis*, vol. 118, no. 1, pp. 275–279, 1989.

[53] E. Voogt, A. Mens, O. Gijzeman, and J. Geus, "XPS Analysis of Palladium Oxide Layers and Particles," *Surface Science*, vol. 350, no. 13, pp. 21–31, 1996.

[54] J. Watts, "Surface Analysis — X-Ray Photoelectron Spectroscopy," in *Encyclopedia of Analytical Science* (P. Worsfold, A. Townshend, and C. Poole, eds.), vol. 8, pp. 5047–5058, Oxford: Elsevier, 1st ed., 1995.

[55] J. E. Fulghum, "Recent Developments in High Energy and Spatial Resolution Analysis of Polymers by XPS," *Journal of Electron Spectroscopy and Related Phenomena*, vol. 100, no. 13, pp. 331–355, 1999.

[56] S. Tougaard, "Surface Analysis — X-Ray Photoelectron Spectroscopy," in *Encyclopedia of Analytical Science* (P. Worsfold, A. Townshend, , and C. Poole, eds.), pp. 446–456, Oxford: Academic Press, 2nd ed., 2005.

[57] J. Walton and N. Fairley, "Characterisation of the Kratos Axis Ultra with Spherical Mirror Analyser for XPS Imaging," *Surface and Interface Analysis*, vol. 38, no. 8, pp. 1230–1235, 2006.

[58] J. I. Langford and A. J. C. Wilson, "Scherrer after Sixty Years: A Survey and Some New Results in the Determination of Crystallite Size," *Journal of Applied Crystallography*, vol. 11, pp. 102–113, Apr 1978.

[59] C. Suryanarayana and M. G. Norton, *X-ray Diffraction: A Practical Approach*. Springer, 1st ed., 1998.

[60] B. Cullity and S. Stock, *Elements of X-Ray Diffraction*. Prentice Hall, 3rd ed., 2001.

[61] J. Angevine, W. N.Delgass, and J. C.Vartuli, "Dispersion and Uniformity of Supported Catalyst by X-ray Photoelectron Spectroscopy," *Proceedings of the 6th International Congress on Catalysis*, vol. 2, pp. 611–620, 1976.

[62] P. Georgopoulos and J. B. Cohen, "Study of Supported Platinum Catalysts by Anomalous Scattering," *Journal of Catalysis*, vol. 92, no. 2, pp. 211–215, 1985.

[63] M. Treacy and A. Howie, "Contrast Effects in the Transmission Electron Microscopy of Supported Crystalline Catalyst Particles," *Journal of Catalysis*, vol. 63, no. 1, pp. 265–269, 1980.

[64] J. Sanders and K. Pratt, "The Relationship of Structure and Activity of NiMo Sulfides to Composition of the Precursor Oxides," *Journal of Catalysis*, vol. 67, no. 2, pp. 331–347, 1981.

[65] S. Nair, "Personal Communication.".

[66] F. P. J. M. Kerkhof and J. A. Moulijn, "Quantitative Analysis of XPS Intensities for Supported Catalysts," *The Journal of Physical Chemistry*, vol. 83, no. 12, pp. 1612–1619, 1979.

[67] X. E. Verykios, F. P. Stein, and R. W. Coughlin, "Influence of Metal Crystallite Size and Morphology on Selectivity and Activity of Ethylene Oxidation Catalyzed by Supported Silver," *Journal of Catalysis*, vol. 66, no. 2, pp. 368–382, 1980.

[68] Y. Okamoto, K. Oh-Hiraki, T. Imanaka, and S. Teranishi, "X-ray Photoelectron Spectroscopic Study of Mixed Oxide Catalysts Containing Molybdenum: I. $SnO_2 - MoO_3$Catalysts," *Journal of Catalysis*, vol. 71, no. 1, pp. 99–110, 1981.

[69] R. Baker, E. Prestridge, and L. Murrell, "Electron Microscopy of Supported Metal Particles: III. The Role of the Metal in an SMSI Interaction," *Journal of Catalysis*, vol. 79, no. 2, pp. 348–358, 1983.

[70] J. Cohen, "X-ray Diffraction Studies of Catalysts," *Ultramicroscopy*, vol. 34, no. 12, pp. 41–46, 1990.

[71] X. Shen, L.-J. Garces, Y. Ding, K. Laubernds, R. P. Zerger, M. Aindow, E. J. Neth, and S. L. Suib, "Behavior of H_2 Chemisorption on Ru/TiO_2 Surface and its Application in Evaluation of Ru Particle Sizes Compared with TEM and XRD Analyses," *Applied Catalysis A: General*, vol. 335, no. 2, pp. 187–195, 2008.

[72] X. Zhu, R. Birringer, U. Herr, and H. Gleiter, "X-ray Diffraction Studies of the Structure of Nanometer-sized Crystalline Materials," *Phys. Rev. B*, vol. 35, pp. 9085–9090, Jun 1987.

[73] D. R. Penn, "Quantitative Chemical Analysis by ESCA," *Journal of Electron Spectroscopy and Related Phenomena*, vol. 9, no. 1, pp. 29–40, 1976.

[74] D. Briggs and M. P. Seah, eds., *Practical Surface Analysis: by Auger and X-ray Photoelectron Spectroscopy.* Chichester: Wiley, 1983.

[75] G. Wertheim, "New Method for Bulk Quantitative Analysis by ESCA," *Journal of Electron Spectroscopy and Related Phenomena*, vol. 50, no. 1, pp. 31–38, 1990.

[76] C. D. Wagner, W. M. Riggs, L. E. Davis, J. F. Moulder, and G. E.Muilenberg, *Handbook of X-ray Photoelectron Spectroscopy.* Physical Electronics Division. Perkin-Elmer Corp., 1978.

[77] C. D. Wagner, L. E. Davis, M. V. Zeller, J. A. Taylor, R. H. Raymond, and L. H. Gale, "Empirical Atomic Sensitivity Factors for Quantitative Analysis by Electron Spectroscopy for Chemical Analysis," *Surface and Interface Analysis*, vol. 3, no. 5, pp. 211–225, 1981.

[78] C. Battistoni, G. Mattogno, and E. Paparazzo, "Quantitative Surface Analysis by XPS: A Comparison among Different Quantitative Approaches," *Surface and Interface Analysis*, vol. 7, no. 3, pp. 117–121, 1985.

[79] S. Kumar, J. V. Ramana, V. S. Raju, J. Arunachalam, and S. Gangadharan, "Determination of Stoichiometry of Cadmium Telluride by XPS," *Fresenius' Journal of Analytical Chemistry*, vol. 343, pp. 879–880, 1992.

[80] D. Hayward and B. Trapnell, *Chemisorption*. Butterworth and Co. Ltd, 2nd ed., 1964.

[81] G. Wedler, *Chemisorption: An Experimental Approach*. Butterworth and Co. Ltd, 1970.

[82] I. E. Wachs, ed., *Characterization of Catalytic Materials*. Butterworth-Heinemann, 1992.

[83] W. W. Smeltzer, E. L. Tollefson, and A. Cambron, "Adsorption of Oxygen by a Silver Catalyst," *Canadian Journal of Chemistry*, vol. 34, no. 8, pp. 1046–1060, 1956.

[84] J. A. Weil, J. R. Bolton, and J. E. Wertz, *Electron Paramagnetic Resonance : Elementary Theory and Practical Applications*. John Wiley & Sons, Inc, 1994.

[85] S. W. Gaarenstroom and N. Winograd, "Initial and Final State Effects in the ESCA Spectra of Cadmium and Silver Oxides," *Journal of Chemical Physics*, vol. 67, no. 10, pp. 3500–3506, 1977.

[86] K. Kim and N. Winograd, "X-ray Photoelectron Spectroscopic Binding Energy Shifts due to Matrix in Alloys and Small Supported Metal Particles," *Chemical Physics Letters*, vol. 30, no. 1, pp. 91–95, 1975.

[87] G. Schön, "ESCA Studies of Ag,Ag_2O and AgO," *Acta Chemica Scandinavica*, vol. 27, pp. 2623–2633, 1973.

[88] J. S. Hammond, S. W. Gaarenstroom, and N. Winograd, "X-ray Photoelectron Spectroscopic Studies of Cadmium- and Silver-Oxygen Surfaces," *Analytical Chemistry*, vol. 47, no. 13, pp. 2193–2199, 1975.

[89] J. Heinzel, "EXAFS Analysis of Supported Ag for Liquid-Phase Logistics Fuel Desulfurization.".

[90] F. Delannay, C. Defosse, B. Delmon, P. G. Menon, and G. F. Froment, "Chloriding of $Pt - Al_2O_3$ Catalysts. Studies by Transmission Electron Microscopy and X-ray Photoelectron Spectroscopy," *Industrial & Engineering Chemistry Product Research and Development*, vol. 19, no. 4, pp. 537–541, 1980.

[91] H. P. C. E. Kuipers, H. C. E. Van Leuven, and W. M. Visser, "The Characterization of Heterogeneous Catalysts by XPS based on Geometrical Probability. 1: Monometallic Catalysts," *Surface and Interface Analysis*, vol. 8, no. 6, pp. 235–242, 1986.

[92] A. Meijers, A. de Jong, L. van Gruijthuijsen, and J. Niemantsverdriet, "Preparation of Zirconium Oxide on Silica and Characterization by X-ray Photoelectron Spectroscopy, Secondary Ion Mass Spectrometry, Temperature Programmed Oxidation and Infra-red Spectroscopy," *Applied Catalysis*, vol. 70, no. 1, pp. 53–71, 1991.

[93] P. W. Park and J. S. Ledford, "Characterization and CH_4 Oxidation Activity of Cr/Al_2O_3 Catalysts," *Langmuir*, vol. 13, no. 10, pp. 2726–2730, 1997.

[94] G. C. Smith, *Surface Analysis by Electron Spectroscopy: Measurement and Interpretation (Updates in Applied Physics and Electrical Technology)*. Springer, 1994.

[95] P. O. Scokart, A. Amin, C. Defosse, and P. G. Rouxhet, "Direct Probing of the Surface Properties of Alkali-Treated Aluminas by Infrared and X-ray Photoelectron Spectroscopy," *The Journal of Physical Chemistry*, vol. 85, no. 10, pp. 1406–1412, 1981.

[96] J. Hamilton and P. Logel, "Nucleation and Growth of Ag and Pd on Amorphous Carbon by Vapor Deposition," *Thin Solid Films*, vol. 16, no. 1, pp. 49–63, 1973.

[97] K. D. Sattler, ed., *Handbook of Nanophysics: Functional Nanomaterials*. CRC Press, 2010.

[98] D. Zhang, X. Yang, J. Zhu, Y. Zhang, P. Zhang, and G. Li, "Graphite-like Carbon Deposited Anatase TiO_2 Single Crystals as Efficient Visible-light Photocatalysts," *Journal of Sol-Gel Science and Technology*, vol. 58, pp. 594–601, 2011.

[99] M. Danilczuk, A. Lund, J. Sadlo, H. Yamada, and J. Michalik, "Conduction Electron Spin Resonance of Small Silver Particles," *Spectrochimica Acta Part A: Molecular and Biomolecular Spectroscopy*, vol. 63, no. 1, pp. 189–191, 2006.

[100] B. Bales and L. Kevan, "EPR of Ag^0 Site Conversion in Gamma-irradiated Frozen $AgNO_3$ Ices," *Chemical Physics Letters*, vol. 3, no. 7, pp. 484–487, 1969.

[101] G. E. Holmberg, W. P. Unruh, and R. J. Friauf, "An ESR and ENDOR Study of the Ag^0 Center in KCl and NaCl," *Phys. Rev. B*, vol. 13, pp. 983–992, 1976.

[102] Y.-P. Wang and C.-T. Yeh, "Electron Paramagnetic Resonance Study of the Interactions of Oxygen with Silver/Titania," *Journal of the Chemical Society, Faraday Transactions*, vol. 87, pp. 345–348, 1991.

[103] S. Livraghi, M. Paganini, M. Chiesa, and E. Giamello, "Trapped Molecular Species in N-doped TiO_2," *Research on Chemical Intermediates*, vol. 33, pp. 739–747, 2007.

[104] A. Samokhvalov, E. C. Duin, S. Nair, M. Bowman, Z. Davis, and B. J. Tatarchuk, "Study of the Surface Chemical Reactions of Thiophene with Ag/Titania by the Complementary Temperature-Programmed Electron Spin Resonance, Temperature-Programmed Desorption, and X-ray Photoelectron Spectroscopy: Adsorption, Desorption, and Sorbent Regeneration Mechanisms," *The Journal of Physical Chemistry C*, vol. 114, no. 9, pp. 4075–4085, 2010.

[105] H. G. Karge and V. Dondur, "Investigation of the Distribution of Acidity in Zeolites by Temperature-Programmed Desorption of Probe Molecules. I. Dealuminated Mordenites," *The Journal of Physical Chemistry*, vol. 94, no. 2, pp. 765–772, 1990.

[106] C. U. I. Odenbrand, J. G. M. Brandin, and G. Busca, "Surface Acidity of Silica-Titania Mixed Oxides.," *ChemInform*, vol. 23, no. 36, pp. no–no, 1992.

[107] A. Auroux, R. Monaci, E. Rombi, V. Solinas, A. Sorrentino, and E. Santacesaria, "Acid Sites Investigation of Simple and Mixed Cxides by TPD and Microcalorimetric techniques," *Thermochimica Acta*, vol. 379, no. 1-2, pp. 227 – 231, 2001.

[108] F. Arena, R. Dario, and A. Parmaliana, "A Characterization Study of the Surface Acidity of Solid Catalysts by Temperature Programmed Methods," *Applied Catalysis A: General*, vol. 170, no. 1, pp. 127 – 137, 1998.

[109] P. A. Thiel, M. Shen, D.-J. Liu, and J. W. Evans, "Adsorbate-Enhanced Transport of Metals on Metal Surfaces: Oxygen and Sulfur on Coinage Metals," *Journal of Vacuum Science & Technology A: Vacuum, Surfaces, and Films*, vol. 28, no. 6, pp. 1285–1298, 2010.

[110] M. Shen, C. Jenks, J. Evans, and P. Thiel, "How Sulfur Controls Nucleation of Ag Islands on Ag(111)," *Topics in Catalysis*, vol. 54, pp. 83–89, 2011.

[111] R. Borade, A. Sayari, A. Adnot, and S. Kaliaguine, "Characterization of Acidity in ZSM-5 Zeolites: An X-ray Photoelectron and IR Spectroscopy Study," *The Journal of Physical Chemistry*, vol. 94, no. 15, pp. 5989–5994, 1990.

[112] C. Defossé, P. Canesson, P. Rouxhet, and B. Delmon, "Surface Characterization of Silica-Aluminas by Photoelectron Spectroscopy," *Journal of Catalysis*, vol. 51, no. 2, pp. 269–277, 1977.

[113] JabRef Development Team, *JabRef*. JabRef Development Team, 2010.

[114] G. Somorjai and Y. Li, *Introduction to Surface Chemistry and Catalysis*. John Wiley & Sons Limited, 2nd ed., 2010.

[115] R. J. Culbertson, L. C. Feldman, P. J. Silverman, and H. Boehm, "Epitaxy of Au on Ag(111) Studied by High-Energy Ion Scattering," *Phys. Rev. Lett.*, vol. 47, pp. 657–660, 1981.

[116] D. R. Lide, ed., *CRC Handbook of Chemistry and Physics*. CRC Press, 86 ed., 2005.

[117] J. H. Scofield, "Hartree-Slater Subshell Photoionization Cross-sections at 1254 and 1487 eV," *Journal of Electron Spectroscopy and Related Phenomena*, vol. 8, no. 2, pp. 129–137, 1976.

[118] C. Powell, "Attenuation Lengths of Low-Energy Electrons in Solids," *Surface Science*, vol. 44, no. 1, pp. 29–46, 1974.

[119] G. G. Fuentes, E. Elizalde, F. Yubero, and J. M. Sanz, "Electron Inelastic Mean Free Path for Ti, TiC, TiN and TiO_2 as Determined by Quantitative Reflection Electron Energy-Loss Spectroscopy," *Surface and Interface Analysis*, vol. 33, no. 3, pp. 230–237, 2002.

Appendices

Appendix A

Physical Properties

Useful Silver Properties

Ag metallic radius	1.45	Å
Ag^{1+} ionic radius	1.26	Å
Ag^{2+} ionic radius	1.01	Å
Ag atomic weight	107.867	g/mol
Ag density	1.05×10^{7}	g/m^3
Ag NN interatomic distance	2.889	Å
Ag(111) fcc surface spacing [114, 115]	2.35 ± 0.1	Å
Ag(110) fcc surface spacing [114]	1.33 ± 0.04	Å
Ag fcc lattice parameter [116]	4.08	Å
Ag active surface atom cross-sectional area [1]	8.6960	$Å^2$/Ag atom
Ag photoemission cross-section Ag $3d_{5/2}$ Al-Kα [117]	1.45×10^{-23}	m^2
	10.66	13600 barns
Ag photoemission cross-section Ag $3d_{3/2}$ Al-Kα [117]	1.00×10^{-23}	m^2
	7.38	13600 barns
Ag photoemission cross-section Ag $3d_{5/2}$ Mg-Kα [117]	2.37×10^{-23}	m^2
Mean free path (1118 eV) Ag $3d_{5/2}$ Al-Kα, λ [73]	1.38×10^{-9}	m

Useful Titanium Properties

TiO_2 molecular weight	79.9	g/mol
Ti density	4.23×10^{6}	g/cm^3
Ti photoemission cross-section Ti $2p_{1/2}$ Al-Kα [117]	3.66×10^{-24}	m^2
	2.69	13600 barns
Ti photoemission cross-section Ti $2p_{3/2}$ Al-Kα [117]	7.10×10^{-24}	m^2
	5.22	13600 barns
Mean free path (1118 eV) Ti $2p_{1/2}$ Al-Kα, λ [73]	1.62×10^{-9}	m

Other Useful Properties		
Al-Kα line width [74]	0.85	eV
Al-Kα line x-ray energy	1486.6	eV
Mg-Kα x-ray energy	1253.6	eV
Mg-Kα line width[74]	0.70	eV
Bohr radius,a_0,	0.529	Å

Appendix B

Sample Calculations

B.1 Calculating the Ag Mole Fraction in Silver-Titania Adsorbent

Physical Data - TiO_2

Molecular Weight, MM TiO_2: 79.9 g/mol

Density ρ, TiO_2: 4.23 g/cm^3

S_A TiO_2: 150 m^2/g

Total pore volume TiO_2: 0.38 cm^2/g

MM $AgNO_3$: 169.87 g/mol

Sorbent Preparation for 4 wt % Ag/TiO_2: 5.8 mL of 1M $AgNO_3$ solution is deposited on 15 g TiO_2

There are 0.0058 moles of $AgNO_3$ in a 5.8 mL 1M $AgNO_3$ solution

$$\#\text{ of moles of } TiO_2 = 15 \text{ g} \times \frac{1 \text{ mol}}{79.9 \text{ g/mol}} = 0.1877 \text{ moles}$$

$$X_{AgNO_3} = \frac{0.0058 \text{ moles } AgNO_3}{0.0058 \text{ moles } AgNO_3 + 0.1877 \text{ moles } TiO_2} = 0.03$$

$$X_{TiO_2} = \frac{0.1877 \text{ moles } TiO_2}{0.0058 \text{ moles } AgNO_3 + 0.1877 \text{ moles } TiO_2} = 0.97$$

Table B.1: Atomic Ratio Ag/TiO_2 Sorbent

Loading (wt %)	1	2	4	8	12	20
TiO_2	0.992	0.985	0.97	0.94	0.91	0.85
Ag	0.008	0.015	0.03	0.06	0.09	0.15

Table B.2: Atomic Ratio of Surface Species on Ag/TiO_2 Adsorbent Pellets

	Ag/TiO_2 Loading					
Element	1wt%	2wt%	4wt%	8wt%	12wt%	20wt%
C-1s	0.24	0.32	0.20	0.21	0.21	0.25
O-1s	0.56	0.50	0.55	0.52	0.50	0.43
TiO_2-2p	0.21	0.16	0.23	0.20	0.22	0.22
Ag-3d	UD	0.01	0.03	0.07	0.07	0.11
Theoretical Ag[†]	0.008	0.015	0.03	0.06	0.09	0.15
Total	1.00	1.00	1.00	1.00	1.00	1.00
	Stoichiometric Ratios					
O/Ti	2.67	3.21	2.41	2.55	2.32	1.95
Ag/O	—	0.02	0.05	0.13	0.14	0.25
Ag/Ti	—	0.07	0.13	0.34	0.32	0.49

[‡] - uncertainty ± 10%

UD - undetectable

[†] - calculated based on the Ag deposited on specimen.

B.2 Calculating Mean Free Path of Titanium Dioxide - Penn Method

The mean free path was calculated for the compound TiO_2 using the method described in Penn [73],

$$\lambda_T = \epsilon/[a(\ln \epsilon + b)] \tag{B.1}$$

where λ_T is the total mean free path due to the valence and core electrons, ϵ is excitation energy in eV, and a and b are electronic concentration functions of η_e. Al Kα (1486.6 eV) x-ray excitation source was used.

$$\eta_e = 6.02 \times 10^{23}\ Z\rho/A \tag{B.2}$$

where η_e is density of valence electrons, cm^{-3}, Z is # of valence electrons, ρ is concentration of solid, $\mathrm{g \cdot cm^{-3}}$, and A is molecular weight, $\mathrm{g \cdot mol^{-1}}$.

For TiO_2, $Z = 4 + 2 \times 6 = 16$, $\rho = 4.23\ \mathrm{g \cdot cm^{-3}}$, $A = 79.9\ \mathrm{g \cdot mol^{-1}}$.

$$\eta_e = \frac{6.02 \times 10^{23}\ \times 16 \times 3.9}{79.9} = 5.10 \times 10^{23}\ \mathrm{cm^{-3}}$$

$$r_s = \left(\frac{3}{4\pi}\frac{1}{n_e}\right)^{\frac{1}{3}} \frac{1}{a_0} \tag{B.3}$$

$$r_s = \left(\frac{3}{4\pi}\frac{1}{5.10 \times 10^{23}}\right)^{\frac{1}{3}} \frac{1}{0.529 \times 10^{-8}} = 1.47$$

For $r_s = 1.47$, using Figure 1 in Penn[73] $a_v = 15.75$ and $b_v = -2.75$.
From Penn [73], Table 1, for a Ti atom N is the number of core electrons in the highest core level, N= 6, and the excitation energy ΔE, of the highest core level, $\Delta E = 66.7$ eV, for an O atom, N= 0 has no core level of importance. Thus,

$$a_c = 3.92 \times 10^2(\rho N/A\Delta E) \tag{B.4}$$

$$a_c = 3.92 \times 10^2 \left(\frac{4.23 \times 6}{79.9 \times 66.7} \right) = 1.87$$

$$b_c = \ln(\Delta E/4) \tag{B.5}$$

$$b_c = -\ln(66.7/4) = -2.81$$

$$a = a_v + a_c = 17.62$$

$$b = (a_v b_v + a_c b_c)/(a_v + a_c) \tag{B.6}$$

$$b = \frac{(15.75 \times -2.75 + 1.87 \times -2.81)}{(15.75 + 1.87)} = -2.76$$

$$\lambda_v = \epsilon/[a_v(\ln \epsilon + b_v)]$$

$$\lambda_v = 1486.6/[15.75(\ln 1486.6 - 2.75)] = 2.07 \text{ Å}$$

$$\lambda_c = \epsilon/[a_c(\ln \epsilon + b_c)]$$

$$\lambda_c = 1486.6/[1.87(\ln 1486.6 - 2.81)] = 176.88 \text{ Å}$$

$$\lambda_T = \lambda_v^{-1} + \lambda_c^{-1} \tag{B.7}$$

$$\lambda_T = 18.5 \ \pm 1 \text{ Å}$$

This value for λ_{TiO2} at 1486.6 eV was found to be in good agreement with other values found in the literature [119]. Also, as expected, $\lambda_{\mathrm{TiO2}} < \lambda_{\mathrm{Ti}}$ due electrons not being as tightly bound in TiO_2 as it is in Ti metal λ_{Ti}= 21.4 Å [73].

Appendix C

Crystal Size Approximation

C.1 Quantitative Estimation of Surface Atoms

How far apart are the Ag atoms in the TiO_2 surface?

Surface area of TiO_2: 150 m^2/g

Assumption: Ag atoms are well-dispersed and equally spaced.

For a TiO_2 surface area loaded with 20 wt% Ag, the SA due to TiO_2 is:

$$= 150 \text{ m}^2/\text{g} \times 0.80 \text{ g} = 120 \text{ m}^2$$

Assuming area is a square, side length of square = $\sqrt{120 \text{ m}^2} \approx 11.0$ m

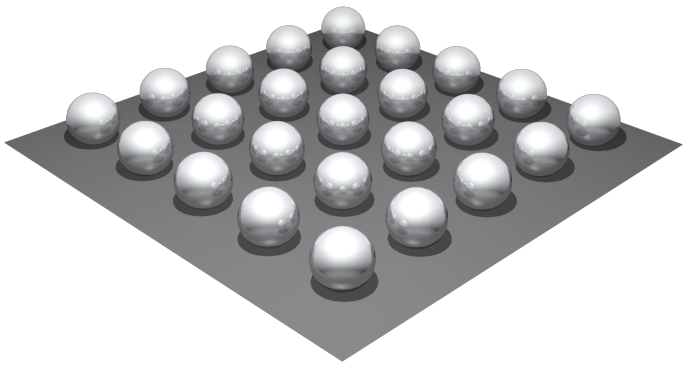

Figure C.1: Square matrix with evenly spaced spherical particles

Number of silver atoms in 0.20 g of Ag:

$$= \frac{0.20 \text{ g Ag}}{107.87 \text{ g/mol}} \times 6.022 \times 10^{23} \text{ atoms/mol} = 1.12 \times 10^{21} \text{ atoms}$$

Number of atoms on a square matrix:

$$= \sqrt{1.12 \times 10^{21}} = 3.34 \times 10^{10} \text{ atoms}$$

Separation distance of Ag atoms:

$$= \frac{11.0 \text{ m}}{3.34 \times 10^{10} \text{ atoms}} = 3.27 \text{ Å} = 0.327 \text{ nm}$$

Using Oxygen Chemisorption data and assumptions:

ρ of Ag : 10.5 g/cm^3 =1.05×10^7g/m^3

At 20 wt%, the avg crystallite size = 6.9 nm

Assuming spherical shape, Volume of sphere, d = 6.9 nm

$$V = \frac{4}{3}\pi \mathrm{r}^3 = \frac{1}{6}\pi \mathrm{d}^3$$

$$V = \frac{1}{6}\pi \ (69\text{Å})^3 = 1.72 \times 10^{-25} \text{ m}^3$$

Mass of atoms in a 69 Å crystal :

$$= \text{density of Ag} \times \text{Volume of sphere}$$

$$= 1.05 \times 10^7 \text{g/m}^3 \times 1.72 \times 10^{-25} \text{ m}^3$$

$$= 1.81 \times 10^{-18} \text{ g}$$

Number of atoms of Ag in a 69 Å crystal :

$$= \frac{1.81 \times 10^{-18} \text{ g Ag}}{\text{Atomic Weight of Ag g/mol}} \times \text{N}_\text{A} \text{ atoms/mol}$$

$$= \frac{1.81 \times 10^{-18} \text{ g Ag}}{107.87 \text{ Ag g/mol}} \times 6.022 \times 10^{23} \text{ atoms/mol} = 1.01 \times 10^4 \text{ atoms}$$

Number of Ag crystallites:

$$= \frac{1.12 \times 10^{21} \text{ atoms}}{1.01 \times 10^{4} \text{ atoms}} = 1.11 \times 10^{17} \text{ crystallites}$$

Assuming one crystallite is equivalent to 6.9 nm

Number of crystallites on a square matrix:

$$= \sqrt{1.11 \times 10^{17}} = 3.33 \times 10^{8} \text{ crystallites}$$

Considering the shadowing effect

Cross-sectional area of a sphere, $d = 6.9$ nm:

$$A_c = \pi \mathrm{r}^2 = \frac{\pi \mathrm{d}^2}{4}$$

$$= \frac{\pi \ (6.9 \text{ nm})^2}{4} = 3.74 \times 10^{-17} \mathrm{m}^2$$

Total surface area of Ag crystallites for 20 wt % loading:

$$= A_c \text{ of a crystallite} \times \text{Total \# of crystallites}$$

$$= 3.74 \times 10^{-17} \mathrm{m}^2 \times 1.11 \times 10^{17} \text{ crystallites}$$

$$= 4.15 \text{ m}^2$$

Percentage of surface area Ag occupies

$$= \frac{4.15 \text{ m}^2}{150 \text{ m}^2} \times 100 = 2.8 \ \%$$

Separation distance of crystallites on a side of the square l= 11 m, assuming center to center separation:

$$= \frac{11 \text{ m}}{3.33 \times 10^8 \text{ crystallites}}$$

$$= 3.29 \times 10^{-8} \text{ m/crystallite} = 329 \text{ Å between each crystallite}$$

Assuming hemispherical shape

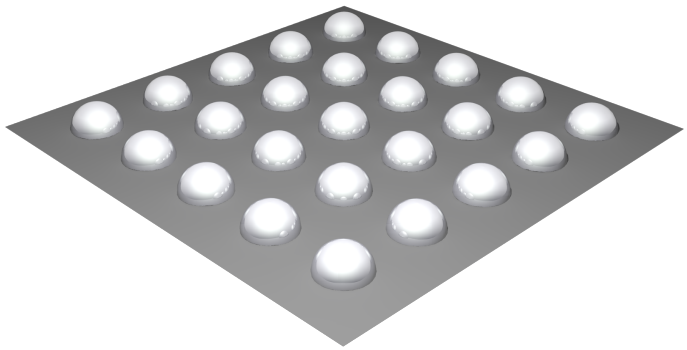

Figure C.2: Square matrix with evenly spaced hemispherical particles

Volume of hemisphere, d = 6.9 nm

$$V = \frac{2}{3}\pi \text{r}^3 = \frac{1}{12}\pi \text{d}^3$$

$$V = \frac{1}{12}\pi \ (69\text{Å})^3 = 8.60 \times 10^{-26} \text{ m}^3$$

Mass of atoms in a 69 Å crystal :

$$= 1.05 \times 10^7 \text{g/m}^3 \times 8.60 \times 10^{-26} \text{ m}^3$$

$$= 9.03 \times 10^{-19} \text{ g}$$

Number of atoms of Ag in a 69 Å crystal :

$$= \frac{9.03 \times 10^{-18} \text{ g Ag}}{107.87 \text{ g/mol}} \times 6.022 \times 10^{23} \text{ atoms/mol} = 5.04 \times 10^{3} \text{ atoms}$$

Number of Ag crystallites:

$$= \frac{1.12 \times 10^{21} \text{ atoms}}{5.04 \times 10^{3} \text{ atoms}} = 2.22 \times 10^{17} \text{ crystallites}$$

Number of crystallites on a square matrix:

$$= \sqrt{2.22 \times 10^{17}} = 4.71 \times 10^{8} \text{ crystallites}$$

Cross-sectional area of a hemisphere, $d = 6.9$ nm:

$$A_c = \pi \mathrm{r}^2 = \frac{\pi \mathrm{d}^2}{4}$$

$$= \frac{\pi \ (6.9 \text{ nm})^2}{4} = 3.74 \times 10^{-17} \mathrm{m}^2$$

Total surface area of Ag crystallites for 20 wt% loading:

$$= A_c \text{ of one crystallites} \times \text{Total \# of crystallites}$$

$$= 3.74 \times 10^{-17} \mathrm{m}^2 \times 2.21 \times 10^{17} \text{ crystallites}$$

$$= 8.28 \text{ m}^2$$

Percentage of surface area Ag occupies

$$= \frac{8.28 \text{ m}^2}{150 \text{ m}^2} \times 100 = 5.5 \text{ \%}$$

Separation distance of crystallites on a side of the square l= 11 m, assuming center to center separation:

$$= \frac{11 \text{ m}}{4.71 \times 10^8 \text{ crystallites}}$$

$$= 2.33 \times 10^{-8} \text{ m/crystallite} = 233 \text{ Å between each crystallite}$$

Assuming cubic shape

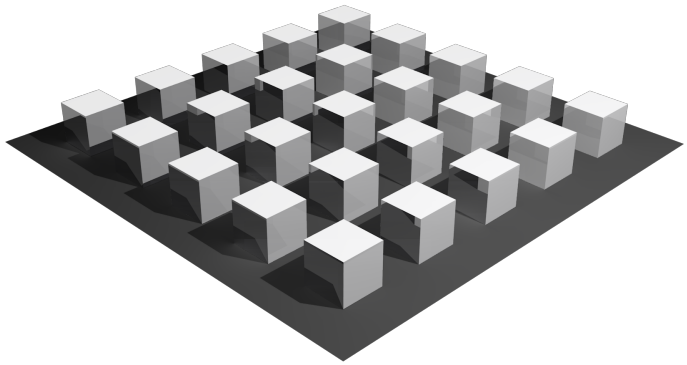

Figure C.3: Square matrix with evenly spaced cubic particles

Side edge of cube s, $s = 6.9$ nm ()

$$V = s^3$$

$$V = (69\text{Å})^3 = 3.29 \times 10^{-25} \text{ m}^3$$

Mass of atoms in a 69 Å crystal :

$$= 1.05 \times 10^7 \text{g/m}^3 \times 3.29 \times 10^{-25} \text{ m}^3$$

$$= 3.45 \times 10^{-18} \text{ g}$$

Number of atoms of Ag in a 69 Å crystal :

$$= \frac{3.45 \times 10^{-18} \text{ g Ag}}{107.87 \text{ g/mol}} \times 6.022 \times 10^{23} \text{ atoms/mol} = 1.93 \times 10^{4} \text{ atoms}$$

Number of Ag crystallites:

$$= \frac{1.12 \times 10^{21} \text{ atoms}}{1.926 \times 10^{4} \text{ atoms}} = 5.80 \times 10^{16} \text{ crystallites}$$

Number of crystallites on a square matrix:

$$= \sqrt{5.80 \times 10^{16}} = 2.41 \times 10^{8} \text{ crystallites}$$

Cross-sectional area of a cube, $s = 6.9$ nm:

$$A_c = s^2$$

$$= (6.9 \text{ nm})^2 = 4.76 \times 10^{-17} \text{m}^2$$

Total surface area of Ag crystallites for 20 wt % loading:

$$= A_c \text{ of one crystallites} \times \text{Total \# of crystallites}$$

$$= 4.76 \times 10^{-17} \text{m}^2 \times 5.80 \times 10^{16} \text{ crystallites}$$

$$= 2.76 \text{ m}^2$$

Percentage of surface area Ag occupies

$$= \frac{2.76 \text{ m}^2}{150 \text{ m}^2} \times 100 = 1.8 \text{ \%}$$

Separation distance of crystallites on a side of the square l= 11 m, assuming center to center separation:

$$= \frac{11 \text{ m}}{2.41 \times 10^8 \text{ crystallites}}$$

$$= 4.56 \times 10^{-8} \text{ m/crystallite} = 456 \text{ Å between each crystallite}$$

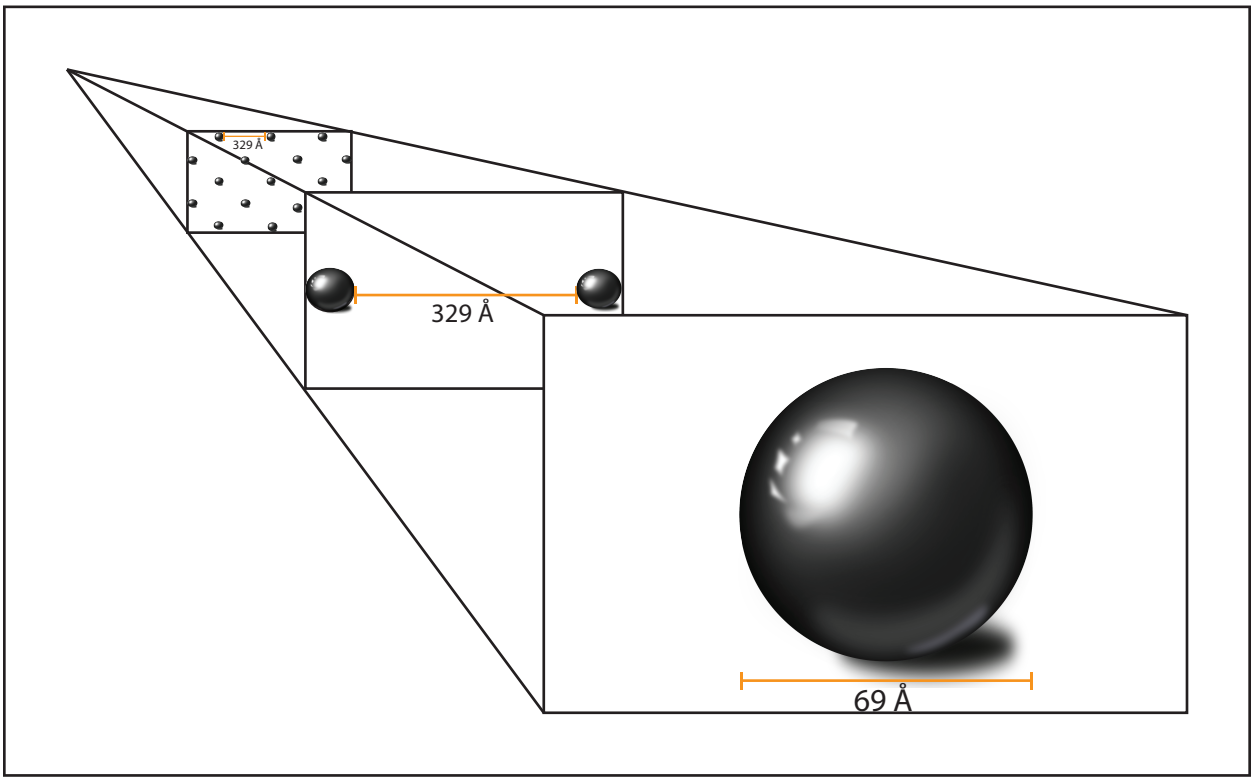

Figure C.4: Schematic representation of 20 wt% Ag particles (particles size derived from chemisorption) on TiO_2 surface .

C.2 Monolayer Estimation

1 ML Ag(111)= 1.14×10^{15} atoms/cm^2 (see Section 2.2)

Number of silver atoms in 0.04 g of Ag:

$$= \frac{0.04 \text{ g Ag}}{107.87 \text{ g/mol}} \times \text{N}_\text{A}$$

$$= \frac{0.04 \text{ g Ag}}{107.87 \text{ g/mol}} \times 6.022 \times 10^{23} \text{ atoms/mol}$$

$$= 2.23 \times 10^{20} \text{ atoms}$$

Thus, there are 2.23×10^{20} atoms in 1 g of 4 wt% Ag/TiO_2.

Number of atoms needed to form 1ML of Ag on 144 m^2 on TiO_2:

$$= 1.14 \times 10^{19} \text{ atoms/m}^2 \times 144 \text{ m}^2$$

$$= 1.64 \times 10^{21} \text{ atoms}$$

Thus, ML formed on 4 wt% Ag/TiO_2 assuming homogenous distribution is:

$$= \frac{2.23 \times 10^{20}}{1.64 \times 10^{21}}$$

$$= 0.131\text{ML}$$

[§]A working basis approximation for polycrystalline surface is to assume that the surface is formed from equal proportions of the main low index planes. The (100), (110), and (111) surfaces are the so-called low index surfaces of a cubic crystal system. The number of surface atoms per unit area of Ag polycrystalline surface is 1.14×10^{19} atoms/m^2.

Table C.1: Surface Coverage Estimation

Data	Ag/TiO_2 Loading				Units
	4 wt%	8 wt%	12 wt%	20 wt%	
Chemisorption Avg Crystal Size (diameter)	3.4	4.1	5.3	6.9	nm
S.A due to TiO_2	144	138	132	120	m^2
Side length of square	12.0	11.7	11.5	11.0	m
No. of silver atoms in Ag Loading	2.23×10^{20}	4.47×10^{20}	6.70×10^{20}	1.12×10^{21}	atoms
No. of atoms on a square matrix	1.49×10^{10}	2.11×10^{10}	2.59×10^{10}	3.34×10^{10}	atoms
Separation distance of Ag atoms[1]	8.030×10^{-10}	5.559×10^{-10}	4.439×10^{-10}	3.278×10^{-10}	m/atom
Spherical Shape					
Volume of sphere ($V = 1/6\pi \cdot R^3$)	2.06×10^{-26}	3.61×10^{-26}	7.80×10^{-26}	1.72E-25	m^3
Mass of atoms in crystallite	2.16×10^{-19}	3.79×10^{-19}	8.18×10^{-19}	1.81×10^{-18}	g
No. of atoms in crystallite	1.21×10^{3}	2.12×10^{3}	4.57×10^{3}	1.01×10^{4}	atoms
No. of crystallite	1.85×10^{17}	2.11×10^{17}	1.47×10^{17}	1.11×10^{17}	crystallites
No. of crystallites on square matrix	4.30×10^{8}	4.59×10^{8}	3.83×10^{8}	3.33×10^{8}	crystallites
Cross sectional area of sphere	9.08×10^{-18}	1.32×10^{-17}	2.21×10^{-17}	3.74×10^{-17}	m^2
Total SA of Ag crystallites	1.68	2.79	3.23	4.14	m^2

Table C.1: Surface Coverage Estimation

	Ag/TiO_2 Loading				
Data	4 wt%	8 wt%	12 wt%	20 wt%	Units
% SA of Ag atoms	1.12	1.86	2.16	2.76	%
Separation distance of crystallite	2.79×10^{-8}	2.56×10^{-8}	3.00×10^{-8}	3.29×10^{-8}	m/crystallite
Hemispherical Shape					
Volume of hemisphere ($V = 1/12\pi \cdot d^3$)	1.03×10^{-26}	1.80×10^{-26}	3.90×10^{-26}	8.60×10^{-26}	m^3
Mass of atoms in crystallite	1.08×10^{-19}	1.89×10^{-19}	4.09×10^{-19}	9.03×10^{-19}	g
No. of atoms in crystallite	6.03×10^{2}	1.06×10^{3}	2.28×10^{3}	5.04×10^{3}	atoms
No. of crystallite	3.70×10^{17}	4.22×10^{17}	2.93×10^{17}	2.21×10^{17}	crystallites
No. of crystallites on square matrix	6.08×10^{8}	6.50×10^{8}	5.41×10^{8}	4.71×10^{8}	crystallites
Cross sectional area of hemisphere	9.08×10^{-18}	1.32×10^{-17}	2.21×10^{-17}	3.74×10^{-17}	m^2
Total SA of Ag crystallites	3.36	5.57	6.47	8.28	m^2
% SA of Ag atoms	2.24	3.72	4.31	5.52	%
Separation distance of crystallite	1.97×10^{-8}	1.81×10^{-8}	2.12×10^{-8}	2.33×10^{-8}	m/crystallite
Cubic Shape					
Volume of cube^2 $V = d^3$	3.93×10^{-26}	6.89×10^{-26}	1.49×10^{-25}	3.29×10^{-25}	m^3
Mass of atoms in crystallite	4.13×10^{-19}	7.24×10^{-19}	1.56×10^{-18}	3.45×10^{-18}	g

Table C.1: Surface Coverage Estimation

	Ag/TiO_2 Loading				
Data	4 wt%	8 wt%	12 wt%	20 wt%	Units
No. of atoms in crystallite	2.304×10^{3}	4.040×10^{3}	8.727×10^{3}	1.926×10^{4}	atoms
No. of crystallite	9.69×10^{16}	1.11×10^{17}	7.68×10^{16}	5.80×10^{16}	crystallites
No. of crystallites on square matrix	3.11×10^{8}	3.32×10^{8}	2.77×10^{8}	2.41×10^{8}	crystallites
Cross sectional area of cube	1.156×10^{-17}	1.681×10^{-17}	2.809×10^{-17}	$4.761\text{E}\times10^{-17}$	m^2
Total SA of Ag crystallites	1.12	1.86	2.16	2.76	m^2
% SA of Ag Atoms	0.747	1.24	1.44	1.84	%
Separation distance of crystallite	3.85×10^{-8}	3.53×10^{-8}	4.15×10^{-8}	4.55×10^{-8}	m/crystallite
Equivalent ML Coverage	0.131	0.261	0.392	0.653	ML

[1]Separation estimation due to weight loading and size of sample area
[2]dimension of one side of cubic particle

C.3 Chemisorption Particle Geometry Analysis

Cubic crystallites with five sides exposed, the surface-to-volume (S/V) ratio of crystallite is:

$$\begin{aligned} \frac{S_T}{V_T} &= \frac{N5d^2}{Nd^3} \\ &= \frac{5}{d} \end{aligned} \tag{C.1}$$

where S_T is the total metal surface area, V_T is the total volume of metal crystallites, N is the number of crystallites, and d is particle dimension. Rearranging Eqn C.1

$$d = \frac{5V}{S}$$

Substituing $\rho = W_m/V_T$

$$d = \frac{5W_m}{S\rho} \tag{C.2}$$

where ρ is the density of the metal, and W_m is the percent weight loading of the metal. Since the average crystallite size is based arbitrarily on a chosen geometry the deviation from the mean of the crystallite size from the geometries was noted in Table C.2

Table C.2: Crystallite Geometry Comparison

Geometry	S/V ratio	Shape factor
Cube	$5/d$	5
Sphere	$6/d$	6
Hemisphere	$6/d$	6

C.4 Theoretical XPS Intensity Calculation

Table C.3: Ag(111) Intensity Estimation

Interatomic Spacing[1]	Atomic Spacing Å	Intensity	Cum. Intensity	Mean Free Path[2] λ
Surface	0.00	1.00	1.00	
1	2.35	0.84	1.84	
2	4.70	0.71	2.55	
3	7.05	0.60	3.15	
4	9.40	0.51	3.66	
5	11.75	0.43	4.09	
6	14.10	0.36	4.45	1
7	16.45	0.30	4.75	
8	18.80	0.26	5.01	
9	21.15	0.22	5.22	
10	23.50	0.18	5.41	
11	25.85	0.15	5.56	
12	28.20	0.13	5.69	2
13	30.55	0.11	5.80	
14	32.90	0.09	5.89	
15	35.25	0.08	5.97	
16	37.60	0.07	6.03	
17	39.95	0.06	6.09	
18	42.30	0.05	6.14	3
19	44.65	0.04	6.17	
20	47.00	0.03	6.21	
21	49.35	0.03	6.24	

Table C.3: Ag(111) Intensity Estimation

Interatomic Spacing[1]	Atomic Spacing Å	Intensity	Cum. Intensity	Mean Free Path[2] λ
22	51.70	0.02	6.26	
23	54.05	0.02	6.28	
24	56.40	0.02	6.30	4
25	58.75	0.014	6.31	
26	61.10	0.012	6.32	
27	63.45	0.010	6.33	
28	65.80	0.008	6.34	
29	68.15	0.007	6.35	
30	70.50	0.006	6.35	5
40	94.00	0.001	6.38	
50	118.0	2.00×10^{-4}	6.39	
100	1175	4.02×10^{-8}	6.39	
500	1175	4.11×10^{-37}	6.39	
1000	2350	1.11×10^{-74}	6.39	

[1] Ag (111) interatomic surface spacing 2.35 Å[114]
[2] Ag mean free path 13.8Å. [73]

Table C.4: Ti(001) Intensity Estimation

Interatomic Spacing[1]	Atomic Spacing Å	Intensity	Cum. Intensity	Mean Free Path[2] λ
Surface	0.00	1.00	1.00	
1	3.79	0.74	1.74	
2	7.58	0.55	2.30	
3	11.37	0.41	2.71	
4	15.16	0.31	3.01	
5	18.95	0.23	3.24	1
6	22.74	0.17	3.41	
7	26.53	0.13	3.54	
8	30.32	0.09	3.63	
9	34.11	0.07	3.70	
10	37.90	0.05	3.75	2
11	41.69	0.04	3.79	
12	45.48	0.03	3.82	
13	49.27	0.02	3.84	
14	53.06	0.02	3.86	
15	56.85	0.01	3.87	3
16	60.64	0.01	3.88	
17	64.43	0.01	3.88	
18	68.22	4.85×10^{-3}	3.89	
19	72.01	3.60×10^{-3}	3.89	
20	75.80	2.68×10^{-3}	3.89	4
21	79.59	1.99×10^{-3}	3.90	
22	83.38	1.48×10^{-3}	3.90	

Table C.4: Ti(001) Intensity Estimation

Interatomic Spacing[1]	Atomic Spacing Å	Intensity	Cum. Intensity	Mean Free Path[2] λ
23	87.17	1.10×10^{-3}	3.90	
24	90.96	8.20×10^{-4}	3.90	
25	94.75	6.10×10^{-4}	3.90	5
30	113.70	1.39×10^{-4}	3.90	
50	189.0	3.72×10^{-7}	3.90	
100	379.37	1.38×10^{-13}	3.90	
500	1175	5.06×10^{-65}	3.90	
1000	2350	2.56×10^{-129}	3.90	

[1] TiO_2(001) interatomic surface spacing 3.79 Å[97, 98]
[2] TiO_2 mean free path 18.5 Å. see Section B.2

Table C.5: I_{Ag}/I_{TiO_2} Theoretical Estimation-Kuipers Case-1

Ag Loading	Concentration	Surface Area Coverage	t_k	I_{Ag}/I_{TiO2}
wt%	moles Ag	m^2	m	
Spherical Model				
4	0.03	0.0112	1.75×10^{-9}	0.022
8	0.06	0.0186	2.18×10^{-9}	0.036
12	0.09	0.0216	2.91×10^{-9}	0.040
20	0.15	0.0276	4.06×10^{-9}	0.050
Hemispherical Model				
4	0.03	0.0224	8.77×10^{-10}	0.047
8	0.06	0.0372	1.09×10^{-9}	0.078
12	0.09	0.0431	1.46×10^{-9}	0.088
20	0.15	0.0552	2.03×10^{-9}	0.111
Cubic Model				
4	0.03	0.00747	2.63×10^{-9}	0.000
8	0.06	0.0124	3.27×10^{-9}	0.022
12	0.09	0.0144	4.36×10^{-9}	0.025
20	0.15	0.0184	6.09×10^{-9}	0.031

Table C.6: I_{Ag}/I_{TiO_2} Theoretical Estimation-Kuipers Case 2

Ag Loading	Concentration	Diameter	Surface Area Coverage	t_k	I_{Ag}/I_{TiO2}
wt%	moles Ag	m	m^2	m	
4	0.03	3.40×10^{-9}	1.13×10^{-9}	0.0163	0.0332
8	0.06	4.10×10^{-9}	1.37×10^{-9}	0.0262	0.0053
12	0.09	5.30×10^{-9}	1.77×10^{-9}	0.0294	0.0583
20	0.15	6.90×10^{-9}	2.30×10^{-9}	0.0352	0.0681

Table C.7: I_{Ag}/I_{TiO_2} Theoretical Estimation-Kuipers Case 3

Ag Loading	Concentration	I_{Ag}/I_{TiO2}	Surface Area Coverage	t_k	Diameter	Diameter
wt%	moles Ag		m^2	m	m	nm
1	0.008					
2	0.015	0.06	0.96	1.02×10^{-11}	3.05×10^{-11}	0.03
4	0.03	0.14	0.92	2.18×10^{-11}	6.55×10^{-11}	0.07
8	0.06	0.31	0.85	5.13×10^{-11}	1.53×10^{-10}	0.15
12	0.09	0.35	0.83	8.16×10^{-11}	2.45×10^{-10}	0.24
20	0.15	0.48	0.78	1.56×10^{-10}	4.66×10^{-10}	0.47